SCUOLA DI DOTTORATO
UNIVERSITÀ DEGLI STUDI DI MILANO-BICOCCA

Department of Medicine and Surgery

PhD program: Translational and Molecular Medicine
Cycle: XXXVIII

Mass Spectrometry in the realm of Renal Pathology: from disease investigation to clinical translation

Surname: **Bindi** Name: **Greta**

Registration number: 872843

Tutor: Prof. Fulvio **Magni**

Co-tutor: Prof. Andrew **Smith**

Coordinator: Prof. Francesco **Mantegazza**

ACADEMIC YEAR 2024/2025

Table of contents

Summary

Among all possible fields of application, renal pathology stands out as particularly suited for the implementation of high-throughput and spatially resolved molecular approaches. Indeed, renal diseases of diverse aetiologies often share similar histopathological manifestations, underscoring the need for techniques capable of exploring, in an *omic* manner, the molecular complexity of the heterogeneous renal compartments. In this thesis, mass spectrometry-based approaches, and in particular mass spectrometry imaging, are applied within the realm of renal pathology with the aim of advancing their use for disease investigation and clinical translation.

In the first chapter, two original approaches for investigating the tumour-immune environment of clear cell Renal Cell Carcinoma (ccRCC) are presented. ccRCC remains a particularly challenging disease due to the high heterogeneity of its microenvironment and the strong influence of immune infiltration on therapeutic response. To address these challenges, patient-derived tumour resections were employed to implement a workflow in which targeted and untargeted spatial proteomics were sequentially applied, enabling the typing and molecular profiling of distinct immune populations within a single tissue section. In parallel, to investigate the influence of immune cells on the ccRCC tumour microenvironment in a controlled and tunable experimental setting, three-dimensional co-culture models of tumour and immune cells were established and characterised using metabolomic and proteomic approaches. Together, these complementary strategies expand the methodological toolkit available for ccRCC research and lay the groundwork for more targeted therapeutic interventions.

In the second chapter, mass spectrometry imaging (MSI) is applied to a challenging-to-diagnose renal disease to explore its potential for clinical translation. Specifically, this work presents a novel approach for the one-slide detection and typing of renal amyloidosis. The robustness of the workflow was also assessed in the instance of different sample preparation methods, including the use of Bouin's fixative as an alternative to formalin, broadening its applicability for large multicentre studies. Finally, this strategy was complemented by integrating digital pathology on the same tissue slide, enabling the concurrent use of a molecular and digital approach for the detection of renal amyloidosis. Altogether, this study bridges the gap between bench and bedside, advancing the use of mass spectrometry imaging in the clinical setting and demonstrating how this high-throughput spatial technique can aid in the elucidation of complex, hard-to-diagnose diseases such as renal amyloidosis.

This thesis constitutes a significant advance in the application of mass spectrometry-based methodologies, and particularly spatially resolved approaches, within renal pathology, linking fundamental disease investigation with clinical translation through innovative *omic* strategies.

Introduction

Renal pathology: from the histological to the molecular era

The Modern Era of renal pathology dates back to 1951, when the renal biopsy started to be used as a primary source of information for the diagnosis of kidney disease. This introduction paved the way for renal pathology to become its own subspecialty of pathology, complemented by the rise of novel tissue staining techniques to delineate the basement membrane thickness and interstitial fibrosis[1,2]. In the late 1950s, the application of transmission electron microscopy to renal biopsies unveiled the fine ultrastructural characteristics of the diseased kidney, enabling the distinction of podocyte foot processes or electron-dense immune complex deposits[3,4]. Since then, and up to this day, renal pathology has been governed by the equivalence of tubule, interstitial and glomerular morphological patterns and kidney function. Whilst it is well founded that the histological characteristics of renal tissue are often sufficient to reveal an underlying pathological condition, morphological alterations are often common to several renal disorders, and therefore the field of renal pathology had to evolve hand in hand with molecular biology in order to link each disease with its pathogenesis.

Molecular biology made its way into the renal field starting from the 1970s and continued its expansion throughout the rest of the century, concurrently with the rise of nucleic acid analysis and genomics[5]. This enabled the characterisation of renal diseases of genetic aetiology, such as Autosomal Dominant Polycystic Kidney Disease (ADPKD)[6], but was still not sufficient to define those pathologies which did not present an underlying genetic cause. After the early 2000s, molecular biology evolved according to the central dogma and shifted its focus on RNA and, finally, proteins and metabolites.

Whilst nephrology research and the clinical setting already employed low-plexed methods for the investigation of these biomolecules, including immunostaining, Enzyme-Linked Immunosorbent Assay (ELISA) and Western blot, the "post-genomic" era gave way to other *omic* techniques, including proteomics and metabolomics enabled by Mass Spectrometry (MS). In human pathology, these high-throughput approaches evaluate the comprehensive proteomic and metabolomic profiles of biofluids (*e.g.*, blood, plasma, or urine) and tissues, aiding the elucidation of both the systemic and tissue-specific alterations linked to the pathophysiology of diseases[7]. This unique capability is especially relevant in the nephropathological context, considering that glomerular sclerosis and renal fibrosis are the final manifestations of a wide variety of renal diseases, and therefore these histomorphological characteristics are not sufficient to pinpoint those molecular mechanisms driving renal damage, and that can be exploited for biomarker discovery and diagnostics[8]. In addition to their molecular depth, *omic* approaches such as mass spectrometry offer the practical advantage of requiring only minimal quantities of archival renal tissue to retrieve a large amount of information, making them particularly suited for studies using patient-derived clinical material. Finally, whilst histomorphology remains central to renal pathology, uncovering the molecular drivers of renal damage would benefit from spatially resolved techniques, such as Mass Spectrometry Imaging (MSI), given their unique ability to correlate spatial tissue architecture and detailed molecular information obtained at the *omic* level.

Mass Spectrometry: principles and applications

Mass spectrometry: basic principles

Among analytical techniques for biomolecule analysis, mass spectrometry represents a cornerstone due to its unmatched sensitivity, throughput, and speed. A mass spectrometer is generally composed of three main elements: an ionisation source, one or more mass analysers, and a detector. During analysis, analytes are introduced into the ionisation source in solid, liquid, or gaseous form and subsequently converted into gas-phase ions. In the mass analyser, these ions are separated according to their mass-to-charge (m/z) ratio. The detector then measures their abundance and transforms the signal into a mass spectrum, which plots the m/z ratio on the x-axis and the ion counts (or relative intensity) on the y-axis[9].

Whilst several types of ionisation source exist, only a few are suitable for macro-biomolecules, such as larger metabolites, peptides and proteins[10]. The most widely employed ionisation source for the analysis of molecules of high molecular weight in biofluids is represented by Electrospray Ionisation (ESI). This approach is also suitable for solid samples, such as tissue or cell homogenates, if resuspended in an appropriate buffer. The strength of the ESI source lies in its ability to volatilise and detect large biomolecules by producing multiply charged ions that extend the measurable mass range by decreasing the m/z ratio. It also offers an unequalled sensitivity, detecting down to the femtomolar range in microlitres of sample volume, whilst providing qualitative and quantitative information[11]. Moreover, ESI-MS can be coupled to a Liquid Chromatography (LC) separation system for molecular fractionation prior to mass spectrometric analysis (LC-ESI-MS), enhancing the separation of complex samples into distinct molecular components[11]. Owing to its high ionisation

efficiency, compatibility with LC, and depth of analysis, ESI-MS is particularly advantageous in nephropathology for the study of liquid samples, such as tissue homogenates, when qualitative and quantitative analysis is required[9,11]. The main pitfall of this approach lies, however, in the lack of histomorphological context and in the extensive sample manipulation required.

Matrix-Assisted Laser Desorption/Ionisation (MALDI) is an ionisation source able to desorb gaseous ions from a solid sample, and it represents the most commonly employed alternative to ESI for the analysis of macromolecules when minimal sample handling is required. MALDI relies on the co-crystallisation of the analyte and a matrix, represented by small organic molecules with a strong absorption at the laser wavelength and acidic properties. The chemical nature of the matrix influences the class of biomolecules that will be desorbed, which can range from proteins, to peptides, lipids, metabolites or even glycans[9,12]. As an ionisation source, MALDI presents both strengths and weaknesses. From an analytical standpoint, MALDI has a lower ionisation efficiency compared to ESI, with 1 every 1000 molecules acquiring a charge within the source[12]. Moreover, a MALDI source cannot be interfaced with a chromatographic system and whilst this technical incompatibility hinders the resolution of complex analyte mixtures, it also enables the acquisition of a high-throughput snapshot of the sample's molecular landscape, represented by an *omic* profile. In addition, MALDI is highly tolerant of salts and contaminants within the analysed specimen, proposing it as a valuable approach for the study of tissue samples, which present a saline environment. Arguably, one of the greatest strengths of MALDI-MS lies in its unique ability to correlate a molecular profile to the raster position where it was acquired, enabling the spatially-resolved detection of analytes within solid samples. Therefore, whilst the analytical needs may

dictate whether ESI or MALDI are preferrable in the instance of liquid samples, such as urine, MALDI remains uniquely suited for spatially resolved molecular profiling of solid samples, enabling the analysis of biomolecules in their native spatial context by correlating the sample spot coordinates with the molecular information. The technique which enables the mapping of molecular distributions directly on a sample surface, such as a tissue section, is referred to as Mass Spectrometry Imaging[13].

In 1997, Caprioli *et al.* first demonstrated the generation of molecular images of intact proteins and endogenous peptides in rat pituitary and pancreatic tissue sections using MALDI-Time-Of-Flight (TOF) MS and coined the approach MALDI MS Imaging[14]. In this technique, an appropriate matrix is homogeneously applied onto a biological sample, such as a tissue section, which is subsequently divided into raster spots, referred to as pixels. Each individual spot is then analysed by laser ablation and consequent ion desorption, generating spatially resolved mass spectra that represent the molecular profile of each pixel. Finally, these distributions are rendered as colour gradients, resulting in molecular images where the coloration reflects the distribution and relative abundance of each ion within the specimen[13] (**Figure 1**).

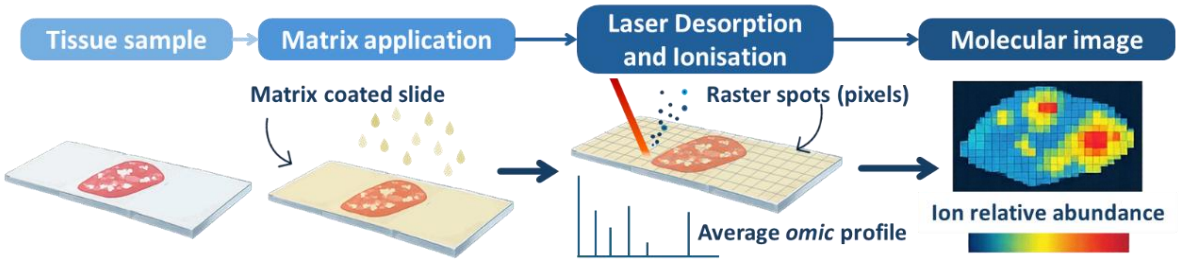

Figure 1. Schematic representation of the MALDI-MSI process.

Over the past four decades, MALDI-MSI has been subjected to significant technical advancements, enhancing every aspect of its output, from the range of biomolecules that can be analysed, to the achievable pixel size, and even its integration with other imaging modalities. The plasticity of MALDI-MSI has been a key factor in its diffusion, considering that it allows spatial maps of different classes of analytes, including endogenous biomolecules and xenobiotics, to be built, pushing its application across diverse disciplines ranging from toxicology and pharmacology to drug development[15]; however, arguably, some of its most promising applications have emerged in the clinical setting. Unlike conventional *omic* modalities that require tissue homogenisation, thereby neglecting the spatial context, MALDI-MSI enables the high-throughput mapping of biomolecular distributions while maintaining the integrity of the histomorphological architecture. By correlating the molecular profiles to each discrete histological compartment, this technology pinpoints regiospecific molecular alterations and provides an indispensable molecular lens for characterising heterogeneous pathological states, bridging the gap between traditional histopathology and molecular profiling.

Importantly, MALDI-MSI is compatible with fixed and embedded samples, which represent the most common form of archival human material and, despite requiring more complex analytical workflows in order to access the contained molecular information, remain a valuable resource for studying rare diseases and enabling large multicentre investigations[16].

MALDI Mass Spectrometry Imaging in renal pathology

Whilst the technique is now widely diffused across multiples areas of medicine, it is particularly well suited to the nephropathology setting. The kidney is anatomically characterised by highly heterogeneous structures, such

as tubuli and glomeruli, whose dimensions fall within the micrometer range. For example, a glomerulus typically measures 100-150 μm in diameter, whereas modern imaging mass spectrometers achieve spatial resolutions of 5-10 μm, enabling the detailed characterisation of renal structures. In Renal Cell Carcinoma (RCC), for instance, MSI enabled the identification of molecular markers and the characterisation of cancerous tissue, the surrounding microenvironment, and neighboring cell populations directly *in situ*, allowing the delineation of tumor margins at the molecular level. Beyond oncology, MALDI-MSI has been applied to the study of primary and secondary glomerulonephritis, including IgA nephropathy, membranous nephropathy, diabetic nephropathy, and lupus nephritis. The technique has also been employed to map lipid distributions in kidney diseases, including diabetic nephropathy and acute kidney injury, as well as to characterise endogenous metabolic profiles. Through its wider application in renal pathology, MALDI-MSI could provide deeper insights into the molecular mechanisms of disease and enable the identification of molecular panels that may provide support for diagnostics and guide more personalised treatment approaches[16,17,18].

References

1. D'Agati, V. D. & Mengel, M. The rise of renal pathology in nephrology: Structure illuminates function. *American Journal of Kidney Diseases* **61**, 1016–1025 (2013).
2. Weening, J. J. & Jennette, J. C. Historical milestones in renal pathology. *Virchows Archiv* vol. 461 3–11 Preprint at https://doi.org/10.1007/s00428-012-1254-7 (2012).
3. Matsumoto, A. *et al.* Quantitative Analyses of Foot Processes, Mitochondria, and Basement Membranes by Structured Illumination Microscopy Using Elastica-Masson– and Periodic-Acid-Schiff–Stained Kidney Sections. *Kidney Int Rep* **6**, 1923–1938 (2021).
4. Golberg, M. *et al.* Application of histochemical stains in anatomical research: A brief overview of the methods. *Translational Research in Anatomy* vol. 35 Preprint at https://doi.org/10.1016/j.tria.2024.100294 (2024).
5. Adam, B. & Mengel, M. Molecular nephropathology: ready for prime time? *Am J Physiol Renal Physiol* **309**, 185–188 (2015).
6. Harris, P. C. & Rossetti, S. Molecular diagnostics for autosomal dominant polycystic kidney disease. *Nature Reviews Nephrology* vol. 6 197–206 Preprint at https://doi.org/10.1038/nrneph.2010.18 (2010).
7. Fung, A. W. S., Sugumar, V., Ren, A. H. & Kulasingam, V. Emerging role of clinical mass spectrometry in pathology. *Journal of Clinical Pathology* vol. 73 61–69 Preprint at https://doi.org/10.1136/jclinpath-2019-206269 (2020).
8. Cummins, T. D. & Powell, D. W. Use of Quantitative Mass Spectrometry Analysis in Kidney Research. *Semin Nephrol* **27**, 574–583 (2007).
9. Hoffmann, E. de & Stroobant, Vi. *Mass Spectrometry: Principles and Applications*. *John Wiley & Sons* vol. 3rd editio (2007).
10. Cristoni, S. & Bernardi, L. R. Development of new methodologies for the mass spectrometry study of bioorganic macromolecules. *Mass Spectrom Rev* **22**, 369–406 (2003).
11. CS Ho *et al.* Electrospray Ionisation Mass Spectrometry: Principles and Clinical Applications. *Clin Biochem Rev* vol. 24 (2003).
12. Lai, Y.-H. & Wang, Y.-S. Matrix-Assisted Laser Desorption/Ionization Mass Spectrometry: Mechanistic Studies and Methods for Improving the Structural Identification of Carbohydrates. *Mass Spectrometry* **6**, S0072–S0072 (2017).
13. Millard, G. M., Krishna, R., Pearce, S. M., Cole, L. M. & Francese, S. *A Beginner's Guide to Mass Spectrometry Imaging Beginner's Guide*. http://portlandpress.com/biochemist/article-pdf/47/2/16/972161/bio_2025_110.pdf.
14. Karas, M. *et al. Molecular Imaging of Biological Samples: Localization of Peptides and Proteins Using MALDI-TOF MS*. *Rapid Commun. Mass Spectrom* vol. 78 https://pubs.acs.org/sharingguidelines (1987).
15. Schulz, S., Becker, M., Groseclose, M. R., Schadt, S. & Hopf, C. Advanced MALDI mass spectrometry imaging in pharmaceutical research and drug development. *Current Opinion in Biotechnology* vol. 55 51–59 Preprint at https://doi.org/10.1016/j.copbio.2018.08.003 (2019).
16. Denti, V. *et al.* Spatial Multiomics of Lipids, N-Glycans, and Tryptic Peptides on a Single FFPE Tissue Section. *J Proteome Res* **21**, 2798–2809 (2022).
17. L'Imperio, V., Smith, A., Chinello, C., Pagni, F. & Magni, F. Proteomics and glomerulonephritis: A complementary approach in renal pathology for the identification of chronic kidney disease related markers. *Proteomics Clin Appl* **10**, 371–383 (2016).
18. Angelotti, M. L., Antonelli, G., Conte, C. & Romagnani, P. Imaging the kidney: From light to super-resolution microscopy. *Nephrology Dialysis Transplantation* vol. 36 19–28 Preprint at https://doi.org/10.1093/NDT/GFZ136 (2021).

Aim

A comprehensive understanding of renal pathologies, as well as the identification of molecular panels of diagnostic relevance, require *omic* approaches capable of capturing the complexity of disease pathophysiology whilst preserving the spatial distribution of analytes within renal compartments. Mass spectrometry techniques, including mass spectrometry imaging, represent a promising and feasible approach in the realm of renal pathology, and whilst their use is rapidly emerging in this field, their full potential remains largely unexplored. The aim of this thesis is to investigate the implementation of these techniques in the nephropathological setting, ranging from greater disease understanding to clinical translation, to ultimately advance diagnostic, prognostic, stratification and therapeutic strategies in kidney disease.

Chapter 1: Novel strategies for disease investigation.
Elucidating the tumour-immune environment of clear cell Renal Cell Carcinoma

1.1 Introduction to Chapter 1

Renal Cell Carcinoma (RCC) is among the ten most commonly diagnosed cancers worldwide, with clear cell RCC (ccRCC) representing the predominant histological subtype[1]. The treatment of ccRCC is particularly challenging due to its unique tumour microenvironment (TME), which involves the presence of heterogeneous sets of cell populations, including fibroblasts, endothelial cells, and tissue-specific populations. Additionally, several types of immune cells, including $CD4^+$ and $CD8^+$ T cells, T regulatory cells, B cells, M1 and M2 macrophages, among others, play a crucial role in defining how the TME will respond to therapy[2]. Due to this ability to recruit T cells and tumour-associated macrophages, ccRCC is considered an "immunogenic" tumour[3]. In light of this characteristic, the standard of care for ccRCC has changed significantly in recent years with the introduction of Immune Checkpoint Inhibitors (ICIs), a major advancement in cancer immunotherapy that has reshaped treatment strategies[4]. However, whilst these therapies have improved survival in a subset of ccRCC patients, many do not respond, and even initial responders frequently relapse, leaving surgical resection as the primary treatment option for localised tumours[5].

In this context, the ability to investigate the diverse cell populations, and more importantly to delineate their interactions and molecular profiles within their native spatial context, is critical to understanding the mechanisms underlying the interplay of immune and tumour cells in the TME of ccRCC. MALDI-MSI offers a unique opportunity in this regard, enabling the untargeted mapping of proteolytic peptides, lipids, and other analytes within tissue whilst retaining spatial information[6]. Furthermore, integration with other spatial omics approaches permits the characterisation of cell phenotypes at multiple molecular levels. A particularly promising development is MALDI-

HiPLEX-IHC-MSI, which enables the targeted, antibody-based detection of tissue antigens via photocleavable mass tags[7] (**Figure 2**) and enables the confident and highly multiplexed mapping of proteins of interest within the TME.

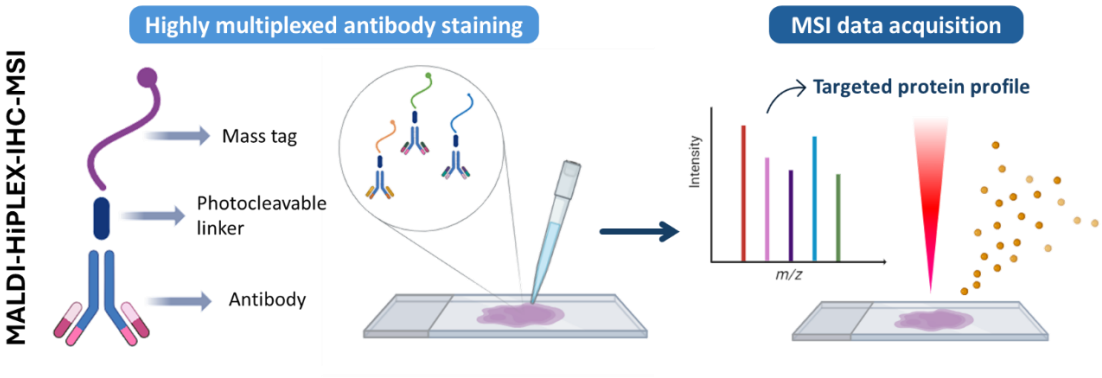

Figure 2. Schematic representation of MALDI-HiPLEX-IHC-MSI workflow.

The combination of targeted MALDI-HiPLEX-IHC-MSI and untargeted spatial proteomics on ccRCC clinical samples could provide pathophysiological insights into the reciprocal influence of immune and tumour cells, possibly enhancing the understanding of the molecular processes that drive resistance or sensitivity to immunotherapy. However, the integration of both facets of spatial proteomics on a single tissue section has not yet been explored.

The application of these techniques on clinical samples, such as tumour resections, would make it possible to capture the full complexity of the TME in ccRCC, providing an invaluable approach for studying mechanisms of immune evasion. However, these specimens may be less suited for isolating the impact of individual factors, such as specific immune cell populations, infiltration patterns, or treatment effects. For the characterisation of individual variables, cellular models provide a natural solution, as they can be tuned to accommodate specific experimental needs and enable the study of disease characteristics in a controlled environment. In recent years, the advent of 3D

cell cultures, comprising spheroids, organoids, and microfluidic systems, has proven more efficient in the reconstitution of the microenvironment of ccRCC. Specifically, the 3D environment better recapitulates key aspects of tumours in their native environment, including oxygenation, tissue architecture, pH gradient, and more[8]. While several experimental systems have been developed to mimic the TME of ccRCC, a simple yet comprehensive 3D model that enables the study of tumour-immune interactions in ccRCC is still lacking.

In the following Chapter, the development of novel approaches for the investigation of patient-derived tumour resections and 3D cellular models is described, aiming to provide mechanistic insights into the link between immune cell infiltration and TME reshaping. In the first line of research, a workflow to integrate targeted and untargeted spatial proteomics is established on ccRCC clinical samples to demonstrate the influence of specific subsets of immune cells on the proteomic profile of tumour cores. In a subsequent work, an approach for the co-culturing of allogeneic immune and ccRCC cells within 3D cellular models is developed. Subsequently, the model is characterised with multiomic MS techniques to assess the influence of immune cells in the TME, complementing the molecular information that can be derived from biologically variable human tissue and facilitating greater insights into the key molecular drivers of this phenomenon.

References

1. Hsieh, J. J., Le, V., Cao, D., Cheng, E. H. & Creighton, C. J. Genomic classifications of renal cell carcinoma: a critical step towards the future application of personalized kidney cancer care with pan-omics precision. *Journal of Pathology* vol. 244 525–537 Preprint at https://doi.org/10.1002/path.5022 (2018).
2. Morad, G., Helmink, B. A., Sharma, P. & Wargo, J. A. Hallmarks of response, resistance, and toxicity to immune checkpoint blockade. *Cell* vol. 184 5309–5337 Preprint at https://doi.org/10.1016/j.cell.2021.09.020 (2021).
3. Monjaras-Avila, C. U. *et al.* The Tumor Immune Microenvironment in Clear Cell Renal Cell Carcinoma. *International Journal of Molecular Sciences* vol. 24 Preprint at https://doi.org/10.3390/ijms24097946 (2023).
4. Sharma, P. *et al.* Immune checkpoint therapy—current perspectives and future directions. *Cell* vol. 186 1652–1669 Preprint at https://doi.org/10.1016/j.cell.2023.03.006 (2023).
5. Chen, Y. W., Rini, B. I. & Beckermann, K. E. Emerging Targets in Clear Cell Renal Cell Carcinoma. *Cancers* vol. 14 Preprint at https://doi.org/10.3390/cancers14194843 (2022).
6. Buchberger, A. R., DeLaney, K., Johnson, J. & Li, L. Mass Spectrometry Imaging: A Review of Emerging Advancements and Future Insights. *Analytical Chemistry* vol. 90 240–265 Preprint at https://doi.org/10.1021/acs.analchem.7b04733 (2018).
7. Claes, B. S. R. *et al.* MALDI-IHC-Guided In-Depth Spatial Proteomics: Targeted and Untargeted MSI Combined. *Anal Chem* **95**, 2329–2338 (2023).
8. Mieville, V., Griffioen, A. W., Benamran, D. & Nowak-Sliwinska, P. Advanced in vitro models for renal cell carcinoma therapy design. *Biochimica et Biophysica Acta - Reviews on Cancer* vol. 1878 Preprint at https://doi.org/10.1016/j.bbcan.2023.188942 (2023).

1.2 Sequential MALDI-HiPLEX-IHC and untargeted spatial proteomics MSI to detect proteomic alterations associated with Tumour Infiltrating Lymphocytes

Adapted from:

Bindi, G.[1], Monza, N.[1], de Oliveira, G. S.[1], Denti, V.[1], Fatahian, F.[2], Seyed-Golestan, S. J.[2], L'Imperio, V.[3], Pagni, F.[3], & Smith, A[1]. (**2025**).
Sequential MALDI-HiPLEX-IHC and Untargeted Spatial Proteomics Mass Spectrometry Imaging to Detect Proteomic Alterations Associated with Tumour Infiltrating Lymphocytes.
Journal of proteome research, *24* (2), 871–880.
https://doi.org/10.1021/acs.jproteome.4c00914

[1] Department of Medicine and Surgery, Proteomics and Metabolomics Units, University of Milano-Bicocca, Vedano al Lambro, 20854, Italy
[2] Medicinal Plants and Drug Research Institute, Shahid Beheshti University, Tehran, IR 1983969411, 00989034563002, Iran
[3] Department of Medicine and Surgery, Pathology Unit, Fondazione IRCCS San Gerardo dei Tintori, University of Milano-Bicocca, Monza, 20900, Italy

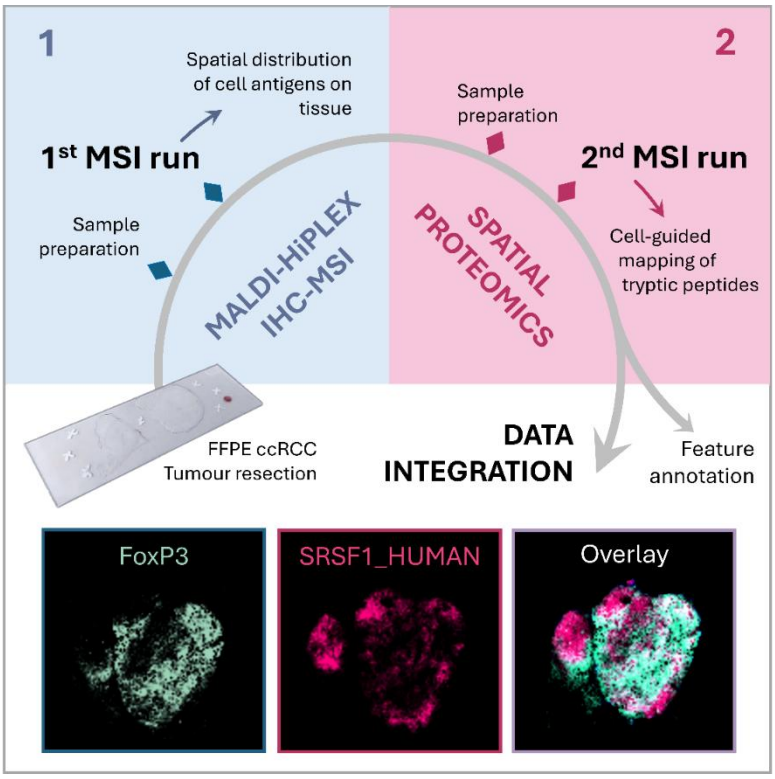

Abstract

MALDI-HiPLEX-IHC Mass Spectrometry Imaging (MSI) represents a newly established workflow to map tens of antibodies linked to photocleavable mass tags (PC-MTs), which report the distribution of antigens in formalin-fixed paraffin-embedded (FFPE) tissue sections. Whilst this highly multiplexed approach has previously been integrated with untargeted methods, the possibility of mapping target cell antigens and performing bottom-up spatial proteomics on the same tissue section has yet to be explored. This proof-of-concept study presents a novel workflow combining MALDI-HiPLEX-IHC with untargeted spatial proteomics to analyse a single FFPE tissue section of clinical clear cell Renal Cell Carcinoma (ccRCC) tissue. Workflow implementation highlighted the need for an additional antigen retrieval step following antibody staining to aid antibody detachment and enhance tryptic digestion. Moreover, this approach enabled the stratification of histologically similar tumour cores of the same grade based on varying lymphocyte populations, particularly T regulatory cells. Finally, integration with untargeted spatial proteomics revealed proteomic alterations associated with these lymphocyte infiltration patterns. These findings demonstrate the potential of this workflow to map and characterise the molecular environment of tumour-infiltrating lymphocytes, offering insights into the molecular impact of immune cells within the tumour microenvironment.

Introduction

The mapping of cell antigens in tissue is routinely carried out with immunohistochemistry (IHC), which represents a well-established technique in both diagnostics and clinical research. However, this approach commonly lacks multiplexing capabilities, with a limit of 3-5 antigens per tissue section[1,2], which represents a limitation when seeking to characterise highly heterogeneous tissue. MALDI-HiPLEX-IHC MSI is a newly established, non-destructive workflow which combines the multiplexing capabilities of mass spectrometry imaging (MSI) with immunohistochemistry (IHC) by staining tissues with tens of antibodies linked to photocleavable mass tags (PC-MTs) which are used to report the antibody-antigen binding[3–5]. Furthermore, this highly multiplexed approach can also be integrated with the untargeted spatial omics aspect commonly associated with MALDI-MSI, facilitating the multiomic characterisation of pathological tissue[3,6]. In particular, this approach has already been utilised to combine cell-antigen mapping with spatial lipidomics (on fresh tissue), N-glycomics, along with the characterisation of the extracellular matrix following *in situ* digestion with collagenase type III[3,6,7]. Moreover, it has also been employed to perform imaging-guided nLC-ESI-MS/MS proteomics through the determination of diverse cell phenotypes although, in this instance, it was noted that the presence of the antibody probes may hinder the enzymatic action of trypsin and reduce the number of ionisable tryptic peptides[3].

Notwithstanding, the possibility to perform mapping of target cell antigens and bottom-up spatial proteomics on the same tissue section has yet to be explored and doing so may further enhance the molecular characterisation of pathological tissue, especially in instances where both the targeted and untargeted facets of this technology are required. As such, this

application could be of particular relevance in the context of tumour immunology, where it is well-documented that the tumour infiltration of certain subsets of immune cells is a contributing factor in terms of patient outcome and response to immunotherapy[8,9], whilst there is more scarce information regarding how their presence may impact the molecular profile of tumour cells within their spatial proximity and where an untargeted approach may be particularly beneficial. Therefore, the integration of an untargeted spatial proteomics aspect within the MALDI-HiPLEX-IHC workflow may offer the potential to better characterise the tumour microenvironment of immunogenic tumours and, possibly, provide new insights into the complex cellular and molecular interplay that occurs.

Based on this premise, this proof-of-concept study describes a workflow in which sequential MALDI-HiPLEX-IHC and MALDI-MSI of untargeted proteins is carried out on clear cell Renal Cell Carcinoma (ccRCC) tissue. In particular, we highlight the importance of performing a second antigen retrieval step post MALDI-HiPLEX-IHC, in order to promote antibody detachment and improve the *in situ* tryptic peptide yield. Moreover, this approach was also used to differentiate histologically indistinct tumour nodules based upon lymphocyte infiltration patterns and highlight proteomic alterations associated with these environments.

Materials and Methods

Chemicals

HPLC grade Toluene, HPLC grade Ethanol (EtOH), HPLC grade Isopropanol and HPLC grade Acetonitrile (ACN) were purchased from Honeywell SC, Seelze, Germany. LC-MS grade Water was obtained from LiChrosolv®. Trifluoroacetic acid (TFA), citric acid monohydrate, eosin Y solution, 50% Octyl-b-D-glucopyranoside (OBG), concentrated alkalyne retrieval buffer (EDTA Buffer, pH 8.5, 10x), Bovine Serum Albumin (BSA), sodium chloride and ammonium bicarbonate (NH_4HCO_3) were obtained from Sigma-Aldrich, St. Louis, Missouri, USA. Mayer's hematoxylin was purchased from Bio Optica Milano Spa, Milan, Italy. Trypsin from the porcine pancreas was obtained from Sigma-Aldrich, St. Louis, MO, USA. α-cyano-4-hydroxycinnamic acid matrix, PepMix I and indium tin oxide (ITO) conductive glass slides were purchased from Bruker Daltonics, Bremen, Germany. Miralys™ Probes were purchased from AmberGen Inc., Billerica, MA, USA. Normal Rabbit Serum and Normal Mouse Serum were obtained from Jackson ImmunoResearch, West Grove, PA, USA. Molecular biology grade Tris-HCl and Tris-Base were purchased from Promega Corporation, Madison, Wisconsin, USA.

Specimen selection

Human tonsil tissue was kindly provided by AmberGen Inc. whilst the ccRCC tissue was derived from nephrectomy specimens performed for neoplasia at the University of Milano-Bicocca, Fondazione IRCCS San Gerardo dei Tintori, Monza, Italy. The appropriate Ethical Committee approved the collection of these specimens and informed consent was obtained from all

participants. The ccRCC tissue cohort was composed of three samples in total; of these, two were utilised to assess the distribution of PC-MTs and were composed of eight Grade G1 tumour nodules, five Grade G2 tumour nodules, and four regions of inflammatory tissue.

Sample preparation

Two formalin fixed and paraffin embedded (FFPE) ccRCC tumour resections were sectioned at a thickness of 4 microns and mounted onto conductive ITO slides. Furthermore, two 4-micron-thick FFPE human tonsil sections and two 4-micron-thick FFPE sections from a third ccRCC tumour resection were employed to assess the need for a second antigen retrieval step after performing MALDI-HiPLEX-IHC. For MALDI-HiPLEX-IHC, sections were processed according to the standardised workflow developed by Yagnik *et al*[4]. Human tonsil tissue was stained with six PC-MT antibody probes, including antibodies against CD68, Vimentin, Collagen α1, Ki67, CD3ε, PanCK at a fixed concentration of 2.50 μg/ml. ccRCC tumour resections were stained with eight PC-MT antibody probes, including antibodies against CD3ε (2.50 μg/ml), CD8α (2.00 μg/ml), CD4 (3.00 μg/ml), FoxP3 (2.00 μg/ml), Ki67 (2.00 μg/ml), PD-1 (2.00 μg/ml), and PD-L1 (2.50 μg/ml). Before antibody staining, alkaline antigen retrieval was performed at 95°C in a water bath for a total of 30 minutes, according to Yagnik *et al*[4]. Following photocleavage, *α*-cyano-4-hydroxycinnamic acid (*α*-CHCA, 10 mg/μl in 70% ACN, 30% LC-MS grade water and 1% TFA) was applied with an HTX TM-Sprayer (HTX Technologies, Chapel Hill, North Carolina, USA) using the following parameters: temperature = 60°C; flow rate = 0.1 ml/min; velocity = 1.350 mm/min; # passes = 8; track spacing = 3mm; nozzle height = 40 mm; PSI = 10; gas flow = 10 l/min; dry time = 10 s. After matrix application, slides were subjected to matrix re-

cristallisation at 55°C in an oven for 2 minutes whilst being exposed to 5% isopropanol vapours. PepMix I was added onto the ITO slide to perform external calibration.

Following MALDI-MSI of the PC-MT antibody probes, slides were washed with decreasing concentrations of EtOH (100%, 2 x 2 minutes; 95%, 1 x 3 min; 70%, 1 x 1 min; 50%, 1 x 3 min; 100% LC-MS-grade water, 2 x 2 min) to remove the matrix and perform tissue rehydration. Afterwards, one tissue section per sample was subjected to a second antigen retrieval in a 10mM citric acid solution at 95°C for 45 minutes, whilst the consecutive sections of tonsil and ccRCC tissue were used as a control. Slides were sprayed with a trypsin solution of 20 ng/µl using an iMatrixSpray sprayer (Tardo, Subingen, Switzerland) with the spraying parameters previously published[10,11] and then incubated at 40°C overnight (~18h) to promote tryptic digestion. The following day, slides were coated with α-CHCA according to previously published parameters[10,11]. PepMix I was added onto the ITO slides to perform external calibration. A visual representation of the workflow is displayed in **Supporting Information, S1**. Hematoxylin and eosin (H&E) staining was performed on the same sections used for the MALDI-MSI experiments. To do so, slides were washed with decreasing concentrations of EtOH (100%, 2 x 2 minutes; 95%, 1 x 3 min; 70%, 1 x 1 min) and stained with H&E. Lastly, slides were scanned using a scanner (NanoZoomer, Hamamatsu Photonics) to be converted to digital format.

MALDI-TOF-MSI analysis

All MALDI-MSI analyses were acquired with a rapifleX MALDI Tissuetyper™ (Bruker Daltonics, Bremen, Germany) equipped with a Smartbeam 3D laser operating at 10 kHz frequency, using FlexControl 4.0

(Bruker Daltonics, Bremen, Germany) to set the mass spectrometry parameters and FlexImaging 5.0 (Bruker Daltonics, Bremen, Germany) in order to set the image acquisition parameters. For all imaging analyses, MALDI-MS images were acquired with the beam scan setting of 46 μm and a raster sampling of 50 μm in both *x* and *y* dimensions. For MALDI-MSI of the PC-MT antibody probes, mass spectra were acquired in positive-ion mode within the *m*/*z* 1100-1600 range whilst the *m*/*z* 700-3000 range for MALDI-TOF-MSI proteomics. In both instances, external calibration with the PepMix I calibration mixture was performed within the relevant *m*/*z* range.

Data analysis

To assess the impact of a second antigen retrieval step, after mapping the PC-MT antibody probes, on the detected proteome, raw data derived from two consecutive sections of human tonsil tissue, and from two consecutive sections of ccRCC tissue, were imported in SCiLS Lab 2024b (Bruker Daltonics, Bremen, Germany). Normalisation (Total Ion Count algorithm) along with baseline subtraction (Convolution algorithm) were first performed. The Segmentation pipeline (which subsequently runs the "Feature Finding" with Orthogonal Matching Pursuit, "Move Peaks to Local Maximum", and "Bisecting k-means" algorithms) was performed on each sample separately. For all the relevant samples, mean spectra of tonsil parenchyma, tonsil connective tissue, ccRCC tumour tissue, and renal connective tissue were calculated and imported into mMass (version 5.5.0, http://www.mmass.org) to aid data visualisation. In mMass, spectra were smoothed using the Savitzky-Golay algorithm, and subsequently peak picking was performed setting a signal to noise threshold of 6.0 and a relative intensity threshold of 0.2%.

For elaboration of the MALDI-HiPLEX-IHC component of the dataset, a separate SCiLS Lab 2024b file was created and baseline subtraction and normalisation were carried out as previously described. A feature list was created to pinpoint those peaks corresponding to the PC-MTs, according to the manufacturer's specification sheet. Moreover, the histological annotations provided by the pathologist, including nodules/regions highlighted as grade G1 (n=9), G2 (n=5) ccRCC, or inflammation (n=4), were imported into the file. Subsequently, the signal intensity deriving from each of the PC-MTs within each of the annotated regions was imported into GraphPad Prism 5 (GraphPad Software Inc., California, USA) for further data visualisation and analysis. Receiver Operating Characteristic (ROC) analysis was performed in order to detect enrichment of any of the PC-MTs within the G2 tumour nodules, reporting those with an AUC≥0.70.

For elaboration of the proteomics MALDI-MSI component of the dataset, the "Feature finding" algorithm was used to generate a feature list for tryptic peptides, whilst deisotoping and the removal of matrix cluster peaks was performed manually. Subsequently, ROC analysis was performed to determine those *m*/*z* features which displayed an increased/decreased signal intensity in those G2 tumour nodules previously determined to have an enrichment in one of the PC-MTs. Feature annotation was performed by correlating the *m*/*z* of features obtained with MALDI-MSI and an *in-house* kidney protein database obtained with nLC-ESI-MS/MS, considering a mass error tolerance of 100 ppm between the measured mass of the tryptic peptide and the actual mass of the tryptic peptide identified by nLC-ESI-MS/MS, as according to previous works present in the literature[4,10–12], and using tissue distribution as an ulterior level of control. Finally, the SCiLS Ion Image Mapper (Bruker Daltonics, Bremen, Germany) tool was used to import ion images

corresponding to the PC-MTs into the MALDI-MSI proteomics data file in order to generate the overlaid ion images.

Results and Discussion

The characterisation of the molecular alterations of cell populations within tissue is of pivotal importance to understand the mechanisms which underpin disease onset and progression. Since their advent and diffusion, untargeted MSI-based spatial *omics* approaches have already led to a huge leap in knowledge in several fields of interest, including human pathology and tumour biology[12–14]. However, these techniques mostly rely on the correlation with histological images, and whilst useful, these often lack the capacity to fully recapitulate the intricate interplay of different cell populations which compose highly heterogeneous contexts such as the tumour microenvironment, where cells characterised by a different molecular phenotype might actually appear indistinguishable by conventional staining techniques. In this work, we assess the feasibility to perform sequential MALDI-MSI of targeted antigens with the AmberGen Miralys™ MALDI-HiPLEX-IHC workflow and untargeted, tryptically digested proteins on the same FFPE tissue section, to correlate cell populations with their specific proteomic signature in the context of the tumour microenvironment of ccRCC.

Antigen retrieval aids antibody detachment from tissue and enhances tryptic peptide yield

As previously reported in the literature[3], prior staining with the antibody probes may inhibit the enzymatic activity of trypsin, most presumably due to steric hindrance, and limit the tryptic peptide yield

observed following MALDI-HiPLEX-IHC. In fact, whilst performing sequential MALDI-HiPLEX-IHC and laser capture microdissection-aided LC-MS, Claes *et al.* reported an inverse correlation between measured protein abundance with untargeted proteomics and targeted abundance based on MALDI-HiPLEX-IHC peptide marker intensity[3], suggesting that the binding of the probes to the target protein might block the interaction with trypsin, thus resulting in a reduction of ionisable tryptic peptides for the target proteins. Therefore, to establish the sequential workflow in the context of *in situ* tryptic digestion, the impact of an additional antigen retrieval on probes detachment step was assessed. To do so, two consecutive sections of tonsil stained with the AmberGen Miralys™ standard Protocol Starter/Validation Kit antibody probe mixture (CD68, Vimentin, Collagen 1α1, Ki67, CD3ε, PanCK), and two consecutive sections of a ccRCC tumour resection stained with a panel of antibodies to target T cell populations, proliferating cells, and immune checkpoints (CD3ε, CD8α, CD4, FoxP3, Ki67, PD-1, and PD-L1) were employed. The probes for the tonsil tissue would stain both the parenchyma (e.g. CD68, CD3) and the connective tissue (e.g. Collagen 1α1), whereas probes for the ccRCC tumour resection would only bind to tumour tissue (e.g. Ki67), with little to no binding to connective tissue, enabling the impact of the antibody probes on the subsequent proteomic profile to also be observed within the same tissue section. Following MALDI-HiPLEX-IHC sample preparation, photocleavage and MSI analysis, some sections underwent a second, acidic antigen retrieval, subsequent to the alkaline antigen retrieval step which is required by the protocol developed by Yagnik *et al*[4]. This was done to promote antibody detachment, whilst also further eliminating formalin-mediated crosslinks through a citric acid buffer (pH 5.9), which is the mostly commonly employed buffer for heat-induced antigen retrieval[15]. **Figure 1** reports the average untargeted proteomic profile obtained from the tonsil

parenchyma and connective tissue (**Figure 1.a.3**) as well as ccRCC tumour tissue and connective tissue (**Figure 1.b.3**). As an example, **Figure 1.a.1** and **Figure 1.b.1** report the binding of an antibody probe, PanCK and FoxP3, respectively, to tonsils and ccRCC tissue samples, as a means to demonstrate the correct staining with PC-MTs in all tissue sections. **Figure 1.a.2** and **Figure 1.b.2** highlight the intensity of signals derived from peptides which are known to co-localise to tonsil parenchyma and tumour tissue (Histone 2A, *m*/*z* 944.6 (1); Histone H3, *m*/*z* 1032.7 (2))[16] or to connective tissue (Collagen 1α1, *m*/*z* 836.5 (3); Collagen 1αII, *m*/*z* 1562.7(4)), in samples which underwent a second antigen retrieval step (2 AR) and samples which were only subjected to one (1 AR). Interestingly, for the 1 AR tonsil samples the intensity of all tryptic peptides of interest was considerably lower in both parenchymal and connective tissue compared to the 2 AR counterpart; as an example, for signal *m*/*z* 944.6 of Histone 2A, a 6.2x fold change (FC) was measured when an additional antigen retrieval was performed. Instead, when considering the 2 AR and 1 AR samples of ccRCC tissue, the signal intensity of Histone 2A and Histone H3 were found to be significantly increased in 2 AR samples, with a FC of 4.6x and 5.0x, respectively, whilst the intensities of collagen 1αI and 1αII were not visibly altered in the connective tissue of 2 AR and 1 AR samples, with a FC of 1.1x and 1.0x, respectively. Furthermore, when looking at the average proteomic profile of the tonsil parenchyma and connective tissue (**Figure 1.a.3**), it is apparent that the peptide yield is significantly higher in 2 AR samples, both in 2 AR tonsil parenchyma compared to 1 AR tonsil parenchyma samples and in 2 AR connective tissue and 1 AR connective tissue (**Table 1**). In contrast, the average proteomic profile of tumour tissue in 2 AR samples of ccRCC shows a higher peptide yield compared to 1 AR samples, whilst the connective tissue spectra are comparable for 2 AR and 1 AR samples (**Figure 1.b.3, Table 1**). Lastly, the distribution of digested tryptic peptides of proteins which were

tagged with the PC-MTs were assessed in the untargeted spatial proteomics dataset. **Supporting Information, S2** displays the distributions of PC-MTs tagging vimentin and collagen 1αI, and the tryptic peptides of the same proteins (Vimentin, *m*/*z* 1527.9; Collagen 1αI, *m*/*z* 836.5) obtained with spatial proteomics after 1 or 2 antigen retrieval steps. Interestingly, the second antigen retrieval allows for the recovery of the signal, with tryptic peptides of digested proteins showing the same distribution of PC-MTs tagging intact proteins. Instead, spatial proteomics performed after a single antigen retrieval confirms a lack of signal, as anticipated in results displayed in **Figure 1**. Altogether, these results indicate that performing a second, acidic, antigen retrieval step aids antibody detachment and increases the peptide yield after performing MALDI-HiPLEX-IHC.

	Number of features		Fold Change
	1 AR	2 AR	(2 AR/1 AR)
Tonsil parenchyma	29	351	12.1
Tonsil connective tissue	43	379	8.8
ccRCC tumour tissue	354	632	1.8
ccRCC connective tissue	702	609	0.9

Table 1. The table reports the number of features detected in samples which underwent only one antigen retrieval step (1 AR) compared to samples who underwent a second antigen retrieval step (2 AR), along with their fold change (2 AR / 1 AR).

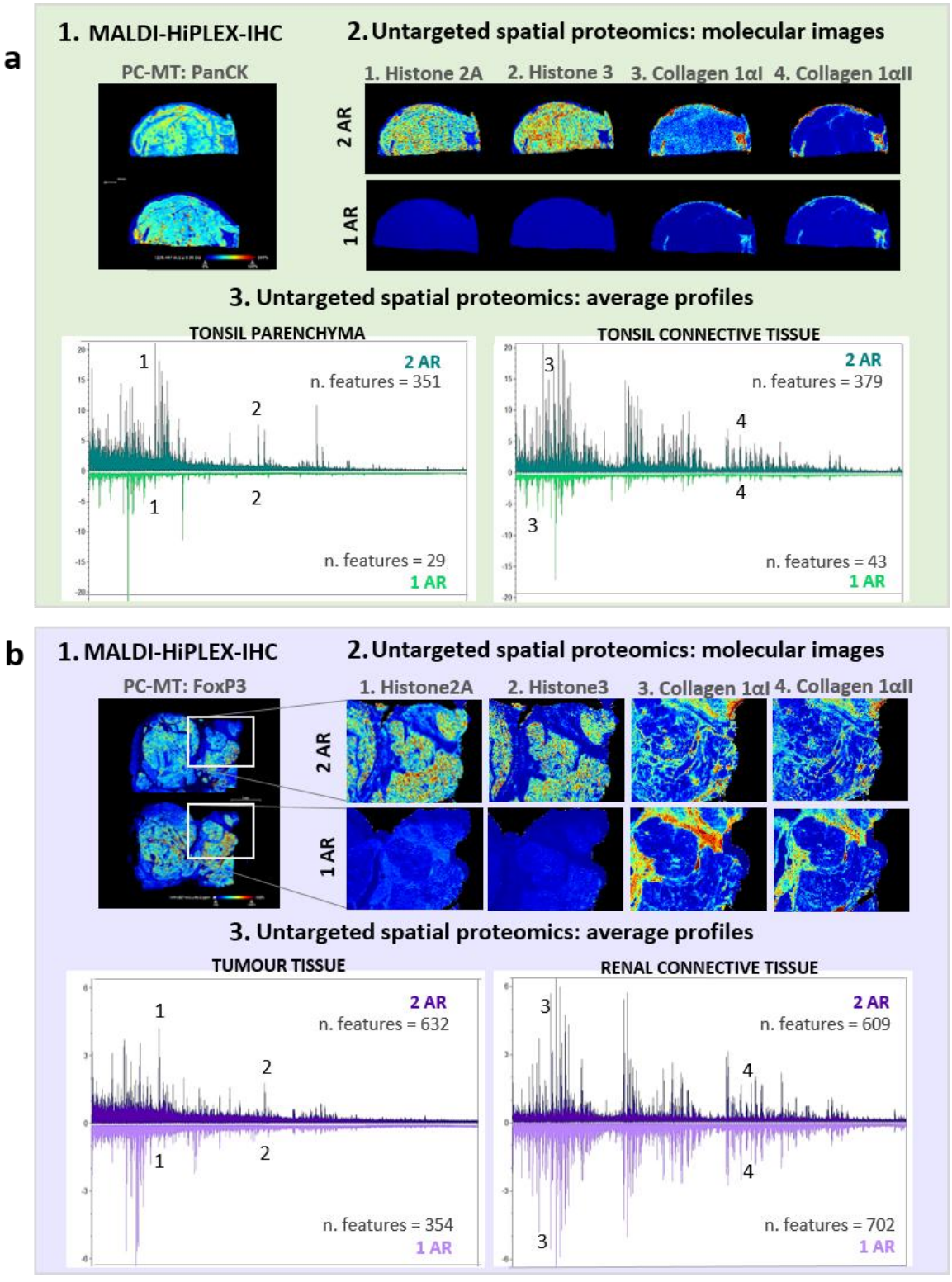

Figure 1. MALDI-HiPLEX-IHC and spatial proteomics were subsequently performed on two tonsil (**1.a**) and ccRCC (**1.b**) samples which either underwent a second antigen retrieval step (2 AR) or didn't (1 AR). **1.a.1**) The molecular image displays the binding of the antibody probe against PanCK in 2 AR and 1 AR tonsils samples; **1.a.2**) Molecular images displaying the intensity and distribution of proteins known to co-localise to parenchyma (Histone 2A, (1); Histone H3, (2)) or to connective tissue (Collagen a1, (3); Collagen aII,(4) in tonsils samples;

1.a.3) Average spectra of tonsil parenchyma and connective tissue when a second antigen retrieval is performed (2 AR, dark green) or isn't (1 AR, light green). **1.b.1**) The molecular image displays the binding of the antibody probe against FoxP3 in 2 AR and 1 AR ccRCC samples; **1.b.2**) Detail of molecular images displaying the intensity and distribution of proteins known to co-localise to tumour tissue (Histone 2A, (1); Histone H3, (2)) or to connective tissue (Collagen a1, (3); Collagen aII,(4)) in ccRCC samples; **1.b.3**) Average spectra of ccRCC tumour and connective tissue when a second antigen retrieval is performed (2 AR, purple) or isn't (1 AR, lilac).

MALDI-HiPLEX-IHC to map the distribution of tumour-infiltrating immune cells in ccRCC tissue

After assessing the need for a second antigen retrieval step following MALDI-HiPLEX-IHC, two further ccRCC tumour resections were subjected to the described workflow to highlight the distribution of T cells (CD3ε, T-cell surface glycoprotein CD3 epsilon chain), T cytotoxic cells (CD8α, T-cell surface glycoprotein CD8 alpha chain), T helper cells (CD4, T-cell surface glycoprotein CD4), T regulatory cells (FoxP3, Forkhead box protein P3), proliferating cells (Ki67, Proliferation marker protein Ki-67), and immune checkpoints (PD-1, Programmed cell death protein-1; PD-L1, Programmed cell death ligand-1) through the staining with PC-MTs. However, prior to evaluating their spatial arrangement in ccRCC tissue, the correct binding of the AmberGen Miralys™ antibody probes was evaluated. To do so, two (non-immediately consecutive) sections obtained from the same tissue specimens were also subjected to classical immunohistochemistry with a small subset of the antibodies, namely those against antigens Ki67, CD3ε, and CD8α, as these are routinely employed to map the distribution of proliferating cells, T cell receptors and T cytotoxic cells, which are expected to be found in highly immune-infiltrated ccRCC. A comparable tissue positivity was observed for the antibodies in both modalities, notwithstanding that the sections were not consecutive (**Supporting Information, S3**).

Considering the spatial arrangement of those probes mapped with MALDI-HiPLEX-IHC, **Figure 2** highlights the relative distribution of proliferating cells, which in the context of tumour pathology can be assumed as either proliferating tumour cells or activated T lymphocytes, and CD3ε$^+$, CD4$^+$, CD8α$^+$ and FoxP3$^+$ cells (**Figure 2.a-d**). Interestingly, proliferating and immune cells seem to display, on the whole, a complementary tissue distribution, with some cell populations showing a more sparse infiltration within tumour cores (*e.g.* T cytotoxic cells), and others presenting an increased presence within some specific nodules (*e.g.* T regulatory cells). Previous studies demonstrated that an increased presence of tumour-infiltrating T regulatory cells is significantly correlated with a poorer prognosis in a number of solid tumours. Therefore, it was not surprising that we assessed a higher number of FoxP3$^+$ cells (FC = 1.7) in tumour cores of higher histological grade (**Supporting Information, S4**). Finally, **Figure 2.e** represents the relative distribution of immune checkpoints PD-1 and PD-L1, which are respectively expressed by T cells, mostly T regulatory and T cytotoxic cells[17,18], and tumour cells[17]. It is known that, after engagement with its ligand PD-L1, PD1 is able to activate a molecular cascade which results in inhibition of T cell proliferation, cytokine production and killer functions, and eventually leads to the death of activated T cells[19]. Interestingly, MALDI-HiPLEX-IHC highlighted that, whilst some regions of tissue still display a complementary distribution of PD-1 and PD-L1, there are other areas in which these antigens show a higher degree of colocalisation, which could indicate an immunosuppressive interaction between tumour and immune cells[20].

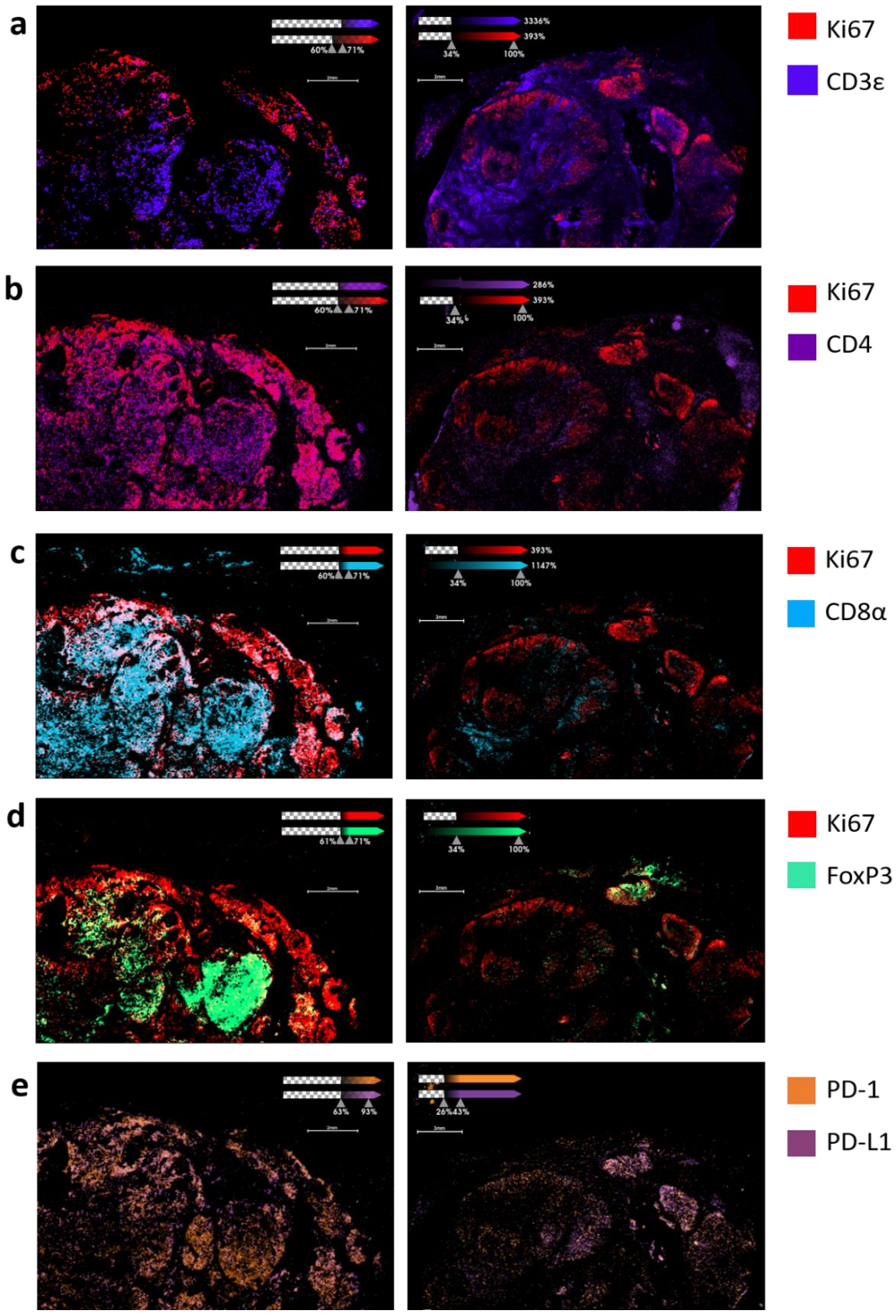

Figure 2. Molecular images obtained with MALDI-HiPLEX-IHC displaying the relative distribution of proliferative Ki67⁺ cells and CD3ε⁺ cells (**a**), CD4⁺ cells (**b**), CD8α⁺ cells (**c**), and FoxP3⁺ cells (**d**). Finally, (**e**) displays the relative distribution of immune checkpoints PD-1 and PD-L1.

The possibility to assess the relative distribution of proliferating cells and various population of immune cells, along with molecular signals mediating immunosuppression, such as immune checkpoint inhibitors, is of particular interest for the characterisation of the tumour microenvironment. In fact, several single-cell studies were able to correlate the quantity and quality of immune infiltration to tumour grading and progression in various types of cancer[21], and Imaging Mass Cytometry has already been employed for the highly multiplexed mapping of immune cell antigens on tissue[22]. However, at the moment little is known on the significance that the relative distribution of these populations entails in terms of cell-cell communication. To retrieve this information, the targeted mapping of immune cells needs to be correlated with techniques able to characterise their phenotype whilst also taking into account their spatial coordinates, such as spatial proteomics.

Integration with untargeted MALDI-MSI proteomics to detect proteomic alterations associated with immune cell infiltration

The distribution of antigens of interest on tissue visualised through MALDI-HiPLEX-IHC analysis suggested an increased presence of certain cell populations within specific tumour cores, based on the findings of the previous paragraph. In order to confirm which of these cell populations had an increased presence, the intensity of the PC-MTs was assessed by grouping tumour cores based on their grading (either G1, G2 or Inflammation), as shown in **Supporting Information, S5.a**. Doing so revealed an increased representation of Ki67, CD8a and PD-L1 positive cells, and a significantly increased presence of PD-1 and FoxP3 ($p < 0.05$) positive cells in G2 cores compared to regions of inflammation, correlated to tumour grade progression; this result indicates a higher abundance of proliferating cells, but also of T cytotoxic cells and of T

regulatory cells, along with immune checkpoints, in cores with a more aggressive phenotype. Based on the general increased presence of the antigens of interest, only G2 cores were taken into consideration for further analyses to differentiate histologically indistinct tumour nodules based upon lymphocyte infiltration patterns and highlight proteomic alterations associated with these environments. To do so, the intensity of each PC-MT in the grade G2 cores (n=5) was assessed as a means of revealing differences in proliferation, T cell infiltration, or immune checkpoint expression among different nodules of the same tumour grade (**Supporting Information, S5.b**). Subsequently, ROC analysis was performed to confront each individual core with the others in terms of PC-MT intensity, and this highlighted a significantly increased (AUC = 0.70) presence of FoxP3, the marker for T regulatory cells, within the core G2_B2#1. The proteomic profile of nodule G2_B2#1 was then confronted with the profiles of the other G2 cores using ROC analysis. This highlighted 6 molecular features corresponding to 4 proteins (Serine/arginine-rich splicing factor 1, SRSF1_HUMAN; Mitochondrial malate dehydrogenase, MDHM_HUMAN; Large ribosomal subunit protein mL39, RM39_HUMAN; Vimentin, VIME_HUMAN) which resulted significantly increased in the core G2_B2#1, and two molecular features corresponding to 2 proteins (Latent-transforming growth factor beta-binding protein 4, LTBP4_HUMAN; Collagen alpha-1(VIII) chain, CO8A1_HUMAN) significantly downregulated in the same core (**Supporting Information, TS1**). The molecular signal *m*/*z* 1314.66 was also found to be increased in G2_B2#1, but upon correlation with our nLC-ESI-MS/MS peptide library and assessment of its distribution within vessels it was annotated as hemoglobin subunit beta (HBB_HUMAN) and eliminated from the list of peptides of interest. **Figure 3.a** displays the distribution and relative intensity of FoxP3 within G2 nodules along with the distribution and relative intensity of two proteins over-represented in G2_B2#1 and two

proteins under-represented in G2_B2#1. Associated with these, **Figure 3.b** shows an overlay of SRSF1_HUMAN, FoxP3 and LTBP4_HUMAN, highlighting regions in which these signals colocalise and regions of complementary distribution of different classes of biomolecules on tissue.

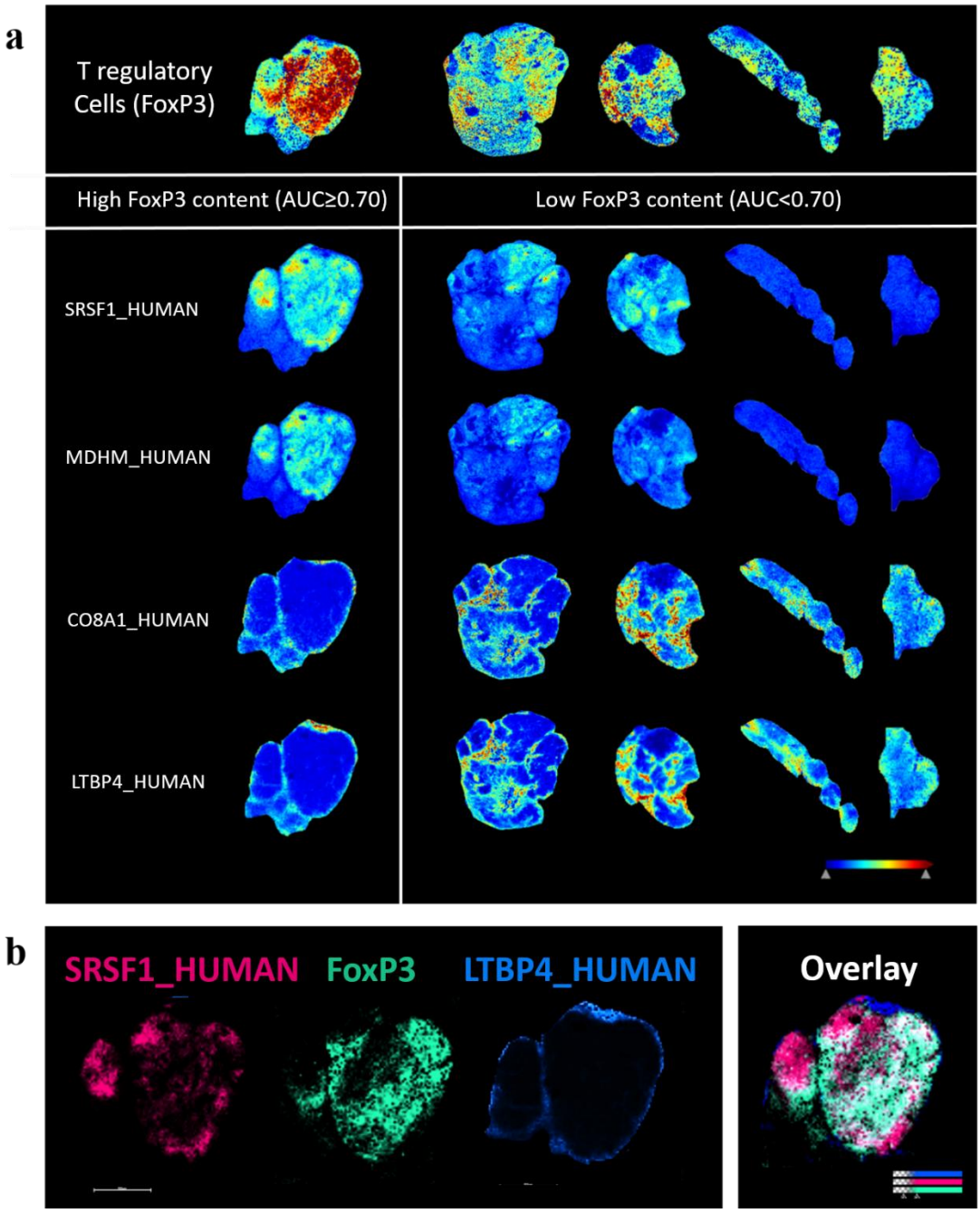

Figure 3 a) The distribution of FoxP3 within G2 cores highlights a nodule which shows a significantly increased (AUC = 0.70) presence of FoxP3⁺ cells, allowing for the division of the G2 cores into those with high and low FoxP3 content. The figure displays the molecular images

of two proteins which resulted enriched in the core high in FoxP3 (SRSF1_HUMAN, MDHM_HUMAN) and two proteins downregulated in the core high in FoxP3 (CO8A1_HUMAN, LTBP4_HUMAN). **b)** Overlay of protein SRSF1_HUMAN, of antigen FoxP3 and of protein LTBP4_HUMAN. Through the integration of multimodal datasets, it is possible to visualise the distribution of different classes of biomolecules on the same tissue slide.

It is interesting to point out that both SRSF1_HUMAN and MDHM_HUMAN have previously been linked to the activity of T cells, and T regulatory cells in particular. Specifically, Splicing factor SRSF1 was proven indispensable for the function and homeostasis of T regulatory cells, and its deficiency is correlated to profound T regulatory cell defects in mice[23]. Moreover, mitochondrial malate dehydrogenase (MDHM_HUMAN) is involved in the malate shuffle known to maintain the balance of NAD^+/NADH between the cytosol and mitochondria[24]. On the one hand, previous studies found an enhanced activity of the shuttle linked to exhausted T cells, which could support the increased presence of MDHM_HUMAN in correspondence with $FoxP3^+$ cells[25]. On the other hand, MDHM_HUMAN has also been linked to T cell activation, specifically in $CD4^+$ cells, of which T regulatory cells are a subset. Lastly, much is known about ribosomes (Large ribosomal subunit protein mL39, RM39_HUMAN) and vimentin (VIME_HUMAN) upregulation in tumour progression. Specifically, due to ribosomes' role as key mediators of translation, which increases proportionally with cell division, ribosomal activity is often increased in various cancers[26,27]. Moreover, countless studies indicated an increased production of vimentin linked to ccRCC progression and aggressiveness[28,29], and this was also confirmed with MALDI-MSI[16]; recently, extracellular vimentin was also proposed as a mediator for tumour-associated endothelial cell anergy, immune cell recruitment, and subsequent tumour-associated immune evasion, further justifying its association with a highly T_{reg}-infiltrated G2 tumour core[30,31].

When considering proteins which showed a negative correlation with the presence of FoxP3$^+$ cells, it is interesting to point out that both are associated with the extracellular matrix, where CO8A1_HUMAN functions as a structural protein and LTBP4_HUMAN is involved in TGFβ management. Interestingly, previous studies indicated that reduction of tumour collagen deposition increases T cell infiltration and reduces depletion of T cells. Moreover, most studies indicate a positive correlation between extracellular matrix-degrading enzymes, such as metalloproteinase, and T regulatory cell infiltration[32]. Furthermore, *in vitro* studies indicated that T cell proliferation was significantly reduced in a high-density matrix compared to a low-density matrix culture[33]. Altogether, these results support the negative correlation between extracellular matrix components and FoxP3$^+$ T cells.

When considering the immune cells which compose the tumour microenvironment, it is unclear whether tumour-infiltrating T regulatory cells are derived from resident immune cells in the tumour-associated tissue, or are derived from peripheral blood. However, a comparison of T regulatory cells taken from the blood, tissue, or tumour, demonstrated that, whilst tissue and tumour-infiltrating T regulatory cells still display a greater similarity due to an activated phenotype, the three groups remain fairly distinct[21]. These findings suggest that, once *in situ*, infiltrating cells may undergo phenotypic and functional changes after being exposed to tumour antigens[21] and molecular signals mediating cell-cell communication. Therefore, the application of a workflow which allows to simultaneously map the relative distribution of tumour and immune cell populations, including immunosuppressive T regulatory cells, whilst also allowing for the untargeted, omic characterisation of their specific expression profile in relation to their surroundings, is of pivotal importance to understand how the microenvironment influences their proteome.

This proof-of-concept work presents some limitations, such as the small subset of tumour cores included in the study, which hinders the possibility to obtain statistically relevant information on the expression profiles of cell populations and limits the biological interpretation of the preliminary results. Notwithstanding these drawbacks, this pilot study successfully highlighted the feasibility and potential of a workflow capable of integrating both targeted and untargeted information on T cell distribution and expression profiles. In future studies, this workflow will be applied to a broader sample cohort to obtain clinically relevant molecular information regarding tumour-immune cell interactions.

Conclusion

In conclusion, this proof-of-concept study describes a workflow to sequentially perform MALDI-HiPLEX-IHC and untargeted spatial proteomics on a single FFPE tissue section of clinical ccRCC tissue. Firstly, the need to perform a second acidic antigen retrieval step after antibody staining, as a means to aid antibody detachment from tissue and reduce the steric hindrance which limits the efficiency of trypsin digestion, was highlighted. Using this workflow, it was then possible to stratify histologically indistinguishable tumour cores of the same grade based upon the infiltration of different lymphocyte populations, in particular T regulatory cells. Finally, the integration of these findings with those obtained by the untargeted spatial proteomics portion of the workflow made it possible to highlight relevant proteomic alterations which may be associated with these specific lymphocyte infiltration patterns. Collectively, this study highlights the potential of this approach when seeking to map and characterise the molecular environment of tumours with an evident immune portion and, considering the advantage of

being able to monitor this through a spatial lens, could be leveraged to better understand the molecular impact that infiltrating immune cells have on their immediate surroundings.

Supporting Information

Supporting Information is available at https://drive.google.com/drive/folders/14ph4fe_yw-6V7AUfRP_knpftR3kLd4iX

References

1. Taube, J. M. *et al.* The Society for Immunotherapy in Cancer statement on best practices for multiplex immunohistochemistry (IHC) and immunofluorescence (IF) staining and validation. *J Immunother Cancer* **8**, (2020).
2. Kim, S. W., Roh, J. & Park, C. S. Immunohistochemistry for pathologists: Protocols, pitfalls, and tips. *Journal of Pathology and Translational Medicine* vol. 50 411–418 Preprint at https://doi.org/10.4132/jptm.2016.08.08 (2016).
3. Claes, B. S. R. *et al.* MALDI-IHC-Guided In-Depth Spatial Proteomics: Targeted and Untargeted MSI Combined. *Anal Chem* **95**, 2329–2338 (2023).
4. Yagnik, G., Liu, Z., Rothschild, K. J. & Lim, M. J. Highly Multiplexed Immunohistochemical MALDI-MS Imaging of Biomarkers in Tissues. *J Am Soc Mass Spectrom* **32**, 977–988 (2021).
5. Lim, M. J. *et al.* MALDI HiPLEX-IHC: multiomic and multimodal imaging of targeted intact proteins in tissues. *Front Chem* **11**, (2023).
6. Fischer, J. L., Lim, M. J. & Yagnik, G. *Multiplex and Multiomic Imaging of Targeted Proteins and Small Molecules: A New Application of the MALDI HiPLEX-IHC Workflow Spatial Proteomics Enables Drug-Target Localization Using MALDI Imaging*.
7. Dunne, J. *et al.* Evaluation of antibody-based single cell type imaging techniques coupled to multiplexed imaging of N-glycans and collagen peptides by matrix-assisted laser desorption/ionization mass spectrometry imaging. *Anal Bioanal Chem* **415**, 7011–7024 (2023).
8. Morad, G., Helmink, B. A., Sharma, P. & Wargo, J. A. Hallmarks of response, resistance, and toxicity to immune checkpoint blockade. *Cell* vol. 184 5309–5337 Preprint at https://doi.org/10.1016/j.cell.2021.09.020 (2021).
9. Jin, M. Z. & Jin, W. L. The updated landscape of tumor microenvironment and drug repurposing. *Signal Transduction and Targeted Therapy* vol. 5 Preprint at https://doi.org/10.1038/s41392-020-00280-x (2020).
10. Bindi, G. *et al.* Feasibility of MALDI-MSI-Based Proteomics Using Bouin-Fixed Pathology Samples: Untapping the Goldmine of Nephropathology Archives. *J Proteome Res* (2024) doi:10.1021/acs.jproteome.4c00198.
11. Bindi, G. *et al.* Spatial resolution of renal amyloid deposits through MALDI-MSI: a combined digital and molecular approach to monoclonal gammopathies. *J Clin Pathol* **77**, 402–410 (2024).
12. Denti, V. *et al.* Spatial Multiomics of Lipids, N-Glycans, and Tryptic Peptides on a Single FFPE Tissue Section. *J Proteome Res* **21**, 2798–2809 (2022).
13. Duncan, K. D., Pětrošová, H., Lum, J. J. & Goodlett, D. R. Mass spectrometry imaging methods for visualizing tumor heterogeneity. *Current Opinion in Biotechnology* vol. 86 Preprint at https://doi.org/10.1016/j.copbio.2024.103068 (2024).
14. Planque, M., Igelmann, S., Ferreira Campos, A. M. & Fendt, S. M. Spatial metabolomics principles and application to cancer research. *Current Opinion in Chemical Biology* vol. 76 Preprint at https://doi.org/10.1016/j.cbpa.2023.102362 (2023).
15. Yamashita, S. Heat-induced antigen retrieval: Mechanisms and application to histochemistry. *Prog Histochem Cytochem* **41**, 141–200 (2007).
16. Stella, M. *et al.* Histology-guided proteomic analysis to investigate the molecular profiles of clear cell Renal Cell Carcinoma grades. *J Proteomics* **191**, 38–47 (2019).
17. Cha, J. H., Chan, L. C., Li, C. W., Hsu, J. L. & Hung, M. C. Mechanisms Controlling PD-L1 Expression in Cancer. *Molecular Cell* vol. 76 359–370 Preprint at https://doi.org/10.1016/j.molcel.2019.09.030 (2019).
18. Kumagai, S. *et al.* The PD-1 expression balance between effector and regulatory T cells predicts the clinical efficacy of PD-1 blockade therapies. *Nat Immunol* **21**, 1346–1358 (2020).

19. Ai Luoyan and Xu, A. and X. J. Roles of PD-1/PD-L1 Pathway: Signaling, Cancer, and Beyond. in *Regulation of Cancer Immune Checkpoints: Molecular and Cellular Mechanisms and Therapy* (ed. Xu, J.) 33–59 (Springer Singapore, Singapore, 2020). doi:10.1007/978-981-15-3266-5_3.
20. Girault, I. *et al.* APD-1/PD-L1 Proximity Assay as a Theranostic Marker for PD-1 Blockade in Patients with Metastatic Melanoma. *Clinical Cancer Research* **28**, 518–525 (2022).
21. Sakaguchi, S. *et al.* Annual Review of Immunology Regulatory T Cells and Human Disease. (2020) doi:10.1146/annurev-immunol-042718.
22. Ijsselsteijn, M. E., van der Breggen, R., Sarasqueta, A. F., Koning, F. & de Miranda, N. F. C. C. A 40-marker panel for high dimensional characterization of cancer immune microenvironments by imaging mass cytometry. *Front Immunol* **10**, (2019).
23. Cassidy, M. F., Herbert, Z. T. & Moulton, V. R. Splicing factor SRSF1 controls autoimmune-related molecular pathways in regulatory T cells distinct from FoxP3. *Mol Immunol* **152**, 140–152 (2022).
24. Kumar, A. & Delgoffe, G. M. Redox and detox: Malate shuttle metabolism keeps exhausted T cells fit. *Cell Metabolism* vol. 35 2101–2103 Preprint at https://doi.org/10.1016/j.cmet.2023.11.005 (2023).
25. Lee, J., Ahn, E., Kissick, H. T. & Ahmed, R. Reinvigorating exhausted T cells by blockade of the PD-1 pathway. *For Immunopathol Dis Therap* **6**, 7–18 (2015).
26. Hwang, S. P. & Denicourt, C. The impact of ribosome biogenesis in cancer: from proliferation to metastasis. *NAR Cancer* vol. 6 Preprint at https://doi.org/10.1093/narcan/zcae017 (2024).
27. Elhamamsy, A. R., Metge, B. J., Alsheikh, H. A., Shevde, L. A. & Samant, R. S. Ribosome Biogenesis: A Central Player in Cancer Metastasis and Therapeutic Resistance. *Cancer Research* vol. 82 2344–2353 Preprint at https://doi.org/10.1158/0008-5472.CAN-21-4087 (2022).
28. Lin, H. *et al.* Vimentin Overexpressions Induced by Cell Hypoxia Promote Vasculogenic Mimicry by Renal Cell Carcinoma Cells. *Biomed Res Int* **2019**, (2019).
29. El-Shorbagy, S. & Alshenawy, H. Diagnostic utility of vimentin, CD117, cytokeratin-7 and caveolin-1 in differentiation between clear cell renal cell carcinoma, chromophobe renal cell carcinoma and oncocytoma. *J Microsc Ultrastruct* **5**, 90 (2017).
30. Zhang, W. *et al.* The intrarenal landscape of T cell receptor repertoire in clear cell renal cell cancer. *J Transl Med* **20**, (2022).
31. Yu, M. B., Guerra, J., Firek, A. & Langridge, W. H. R. Extracellular vimentin modulates human dendritic cell activation. *Mol Immunol* **104**, 37–46 (2018).
32. Lv, D. *et al.* Crosstalk between T lymphocyte and extracellular matrix in tumor microenvironment. *Frontiers in Immunology* vol. 15 Preprint at https://doi.org/10.3389/fimmu.2024.1340702 (2024).
33. Kuczek, D. E. *et al.* Collagen density regulates the activity of tumor-infiltrating T cells. *J Immunother Cancer* **7**, (2019)

1.3 Exploring the influence of immune cells in the tumour microenvironment of clear cell Renal Cell Carcinoma: insights from 3D in-vitro models

Manuscript in preparation for submission

Greta Bindi[1], Lisa Pagani[1], Clizia Chinello[1], Simone Serrao[1], Eleonora Bossi[1], Manon Van Der Ploeg[2], Manfred Wuhrer[3], Fulvio Magni[1], Ieva Palubeckaite[3] and Andrew Smith[1]

[1] Proteomics and Metabolomics Unit, Department of Medicine and Surgery, University of Milan-Bicocca, Vedano al Lambro, Italy
[2] Pathology Unit, Leiden University Medical Centre, Leiden, Netherlands
[3] Centre for Proteomics and Metabolomics (CPM), Leiden University Medical Centre, Leiden, Netherlands

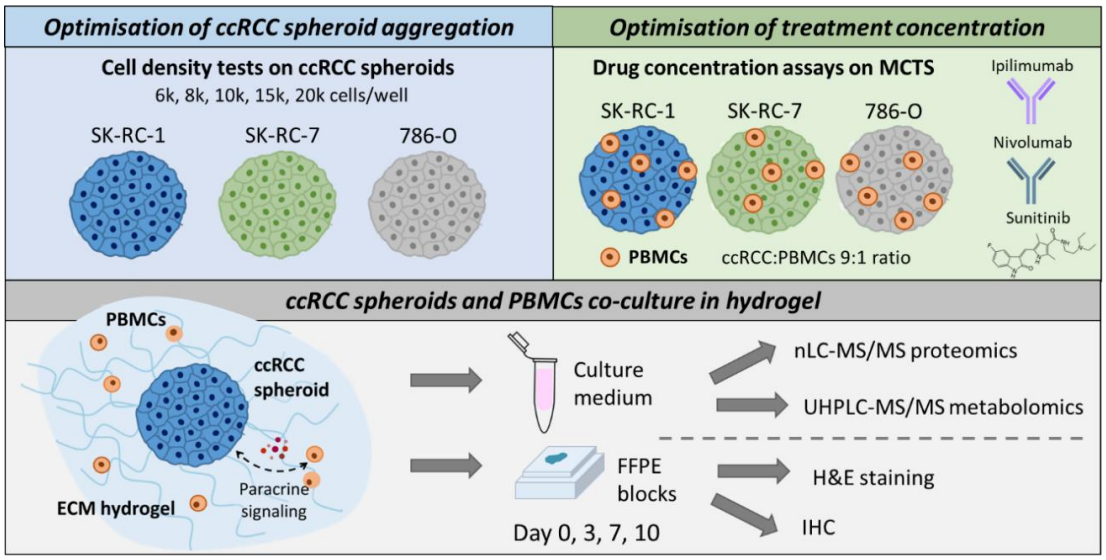

Abstract

Clear cell Renal Cell Carcinoma (ccRCC) is characterised by extensive immune cell infiltration, metabolic reprogramming, and extracellular matrix remodelling. These features contribute to tumour growth and drug resistance, and therefore their characterisation might help predict outcomes and guide pharmacological treatment. In this setting, 3D multicellular models hold the potential to reproduce the complex dynamics of the ccRCC microenvironment, offering a deeper understanding of the interplay of tumour and immune cells in a controlled experimental setting. In this work, we describe the development of 3D cellular models to mimic tumour-immune interactions. Parameters for ccRCC spheroid aggregation and treatment concentrations were first optimised, and subsequently tumour spheroids were embedded in a collagen-based hydrogel containing peripheral blood mononuclear cells (PBMCs). Immune checkpoint inhibitors were also administered to assess their effects on these dynamics. Culture viability over 10 days was evaluated using Presto Blue assay and histological/immune-staining. To characterise the effect of co-culturing with high-throughput, multiomic approaches, culture medium was withdrawn at relevant timepoints to perform proteomic and metabolomic analyses. This work confirmed the feasibility of the proposed model, which enables the *in-vitro* study of the tumour-immune dynamics which characterise ccRCC. Moreover, multiomic culture medium profiling revealed key pathways modulated by PBMCs, including the coagulation cascade, epithelial-to-mesenchymal transition, glutamine/glutamate metabolism, and inflammatory processes. Overall, this study demonstrates the potential of the proposed model to recapitulate the ccRCC tumour microenvironment and, through metabolomic and proteomic approaches, provided new insights into mechanisms of tumour-immune interaction.

Introduction

Renal Cell Carcinoma (RCC) represents the most commonly diagnosed kidney cancer, accounting for approximately 3% of all tumours worldwide[1–3]. In recent years, the advent of systemic targeted therapies, such as Tyrosine Kinase Inhibitors (TKI) and Immune Checkpoint Inhibitors (ICIs), has greatly improved patients' overall survival[4–8]. However, at present, the 5-year survival rate remains at 74%[9], with 10-25% of metastatic patients not responding to first line treatments[9,10], underscoring the need to better understand the biology of this disease[11]. RCC is notably one of the most immune-infiltrated solid tumours, with the predominant subtype, clear cell Renal Cell Carcinoma (ccRCC), showing the highest degree of immune cell infiltration[9,10,12]. Over the years, the role of the immune system in influencing tumour growth and metastasis has gained increasing importance in the study of the tumour microenvironment (TME) of ccRCC[11,13]. Several efforts have been made to understand the contribution of different immune cell phenotypes and key pro-tumoural signalling molecules, as well as their association with prognosis and response to therapy[11,12]. However, established immune-related prognostic and predictive biomarkers have proven insufficient for determining tumour outcome or guiding clinical decision-making in ccRCC[9,10,14].

Interestingly, a well-known characteristic of ccRCC is its metabolic dysregulation or "reprogramming", which actively drives tumorigenesis and influences tumour-immune microenvironment dynamics[10,11,15,16]. Altogether, these metabolic alterations are known to have repercussions on T cell functions[10,17]; for example, arginine and tryptophan metabolism are critical for T cells given that their removal from the microenvironment causes an arrest in T cell division.[18] Instead, the presence of kynurenin, a downstream metabolite of tryptophan metabolism, has been associated with ICIs resistance in

ccRCC[10,15,17]. Beyond metabolic reprogramming, extracellular matrix (ECM) remodelling stands out as another critical aspect of the TME, significantly influencing the interplay of cancer and immune cells[19,20]. Whilst the process is primarily driven by stromal cells, ECM remodelling both shapes and is shaped by immune cell activity[21–25]. For instance, ECM turnover facilitates the release of growth factors and cytokines bound to proteoglycans and glycosaminoglycans, thereby activating downstream signalling pathways that drive cancer cell proliferation and immunoregulation[19,20]. Conversely, increased ECM stiffness can induce immunotherapy resistance by restricting immune cell infiltration and drug perfusion to the tumour[19,26,27]. Interestingly, Prakash *et al.* suggested that the administration of targeted therapies, such as ICIs, could also potentially influence ECM remodelling, though this relationship remains poorly understood[19].

Given that a high degree of immune infiltration, altered metabolism, and ECM dynamics represent key hallmarks of ccRCC[17], exploring their interplay could provide new insights into the mechanisms driving tumour immune escape and immunotherapy resistance. Regarding this aspect, 3D cell cultures have emerged as viable approaches to model tumour and immune cell interactions, as they reduce the complexity of highly heterogeneous diseases, such as ccRCC, whilst still mimicking key aspects of tumours in their native environment, including oxygenation, tissue architecture, and pH gradient[9]. For instance, studies were conducted to generate immune-infiltrated ccRCC models, where tumour spheroids and Peripheral Blood Mononuclear Cells (PBMCs) were co-cultured with a liquid overlay approach or co-aggregated through the formation of Multi-Cellular Tumour Spheroids (MCTS)[28,29]. In their work, Rausch *et al.* characterised heterotypic 3D ccRCC models co-cultured with immune cells to evaluate the influence of diverse drugs on immune infiltration within ccRCC spheroids[28]. Whilst this easy-to-use approach proved

to be a valuable tool to study tumour-immune cell interactions, as well as treatment screening, experiments were limited to a short duration (up to 5 days), which may restrict the model's ability to capture the longer-term dynamics of immune and tumour cell interactions. Additionally, as immune cells were either mixed within the spheroid or seeded on top of it, certain aspects such as immune cell migration and ECM remodelling could not be fully explored within this system[30]. In prior studies, alternative methodologies have incorporated pre-aggregated spheroids into ECM-mimicking hydrogels composed of Collagen I and basal membrane extracts (BME), which provide essential ligands needed for integrin adhesion during cancer cell invasion. The studies were conducted on a panel of cancer cells (mammary, epidermoid, breast, pancreas, prostate, glioblastoma, astrocytoma), excluding ccRCC, to study cell behaviour in a TME-like environment where cells are able to migrate and interact[31–35]. Interestingly, it was found that spheroid formation was further promoted in cell lines with enhanced epithelial features, as would be the case for ccRCC, as this process originates from the epithelial cells lining renal tubules. Several other 3D cellular models of ccRCC have also been developed[28,36,37], albeit no study was conducted in a setup where the migration-promoting abilities of basement membrane extracts and the structural and mechanical properties of collagen were combined in a single scaffold. Altogether, a long-term co-culture system that reproduces the complexity and 3D architecture of the TME of ccRCC has yet to be established.

Building on this groundwork, the scope of this work was to develop advanced 3D cellular models to reproduce immune-tumour cell interactions in the TME of ccRCC. Specifically, spheroid formation capability by aggregation was assessed for a panel of ccRCC cell lines. Subsequently, spheroids were embedded in a collagen-based hydrogel with basement-membrane extract, as per previous works, and co-cultured with allogeneic PBMCs derived from a

pool of 10 healthy donors to minimise HLA mismatch. Specifically, PBMCs were incorporated within the gel to enable direct and paracrine interactions between tumour and immune cells to be studied in a physiologically relevant 3D context. Then, to evaluate alterations on the secretome related to cell metabolism and ECM remodelling driven by the presence of immune cells, mass spectrometry-based approaches were utilised to assess metabolomic and proteomic alterations in culture media. Finally, the established model was treated with a TKI (Sunitinib) or ICIs (Ipilimumab, Nivolumab), to assess the influence of pharmacological treatments on ECM dynamics. Altogether, this study demonstrated the feasibility of the proposed model, offering novel insights into the role of immune cells and ICIs in altering metabolic pathways and ECM dynamics in ccRCC.

Materials and methods

Cell lines and preparation

Three ccRCC cell lines, 786-O (CLS Cell Lines Service GmbH, Eppelheim, Germany), SK-RC-7 and SK-RC-1 (courtesy of Leiden University Medical Centre, Leiden, Netherlands) were employed for this study. PBMCs were obtained from the blood of 10 healthy donors from Sanquin bloodbank (Netherlands) using a Ficoll™ gradient; after PBMC retrieval, cells were pooled. ccRCC cells were thawed and cultured in 2D with a complete medium composed of Gibco™ DMEM, high glucose, GlutaMAX™ Supplement (**Supplementary Information, T1**) with 10% heat inactivated Fetal Bovine Serum (Sigma, St. Louis, USA) and 0.5% penicillin G and streptomycin (Sigma, St. Louis, USA).

Spheroid aggregation

Ultra-low-adhesion plates were prepared by dissolving agarose (UltraPure Agarose, Invitrogen) in ddH_2O (1% w/v) and heating at 90˚C for 30 minutes. 80 µl of agarose solution was added to each well of a 96-well plate, avoiding edge wells. Plates were let cool for 2 hours, then stored at 4˚C with the edge wells filled with PBS to prevent drying out until the day of use. For density tests, cells were trypsinised and seeded at a density of 6000, 8000, 10000, 15000 and 20000 cells/well. Cell aggregation was promoted through a methylcellulose supplemented medium prepared at 0.24% (w/v) in complete DMEM medium. After seeding, cells were left to aggregate for 3 days in the incubator with 5% CO_2 at 37°C.

Inclusion of spheroids in hydrogel

After three days of aggregation, single spheroids were moved to an ultra-low-attachment agarose-coated plate (1 spheroid/well) and all excess medium was removed. The hydrogel mix was prepared as follows: 50% Collagen Type I (Rat Tail, Ibidi GmbH, Gräfelfing, Germany), 10% 10X DMEM, 31.7% BME (Cultrex® Reduced Growth Factor Basement Membrane Matrix, Type R1, Trevigen, Gaithersburg, Maryland), 8.3% of 0.1M NaOH. After the hydrogel-mixture was prepared, PBMCs were added to reach a final ratio of 9:1 ccRCC:PBMCs, which is consistent with ratios used in previous immune-tumour co-culturing models[28,38,39]. 10 µl of the mixture of PBMCs in hydrogel was then deposited on top of each spheroid, and subsequently the plate was incubated for 30 min at 37°C to enable gelation. After incubation, plates were acclimatised to room temperature for 5 minutes and supplemented with complete DMEM. Hydrogels were cultured for a total of 10 days. Experiments

were performed with the SK-RC-1 cell line, with two technical replicates per timepoint, and three biological replicates (passage 73, 77, and 81). At the end of the experimentation period, STR profiling was performed on SK-RC-1 cells targeting alleles TH01, D21S11, D5S818, D13S317, D7S820, D16S539, CSF1P0, Amelogenin, vWA, TP0X, to confirm the authenticity of the cell lines used. The obtained STR profile was compared to reference profiles from the database https://www.cellosaurus.org/CVCL_4017.

Hydrogel treatment

Hydrogels were treated with a TKI, Sunitinib (Sellerchem, Houston, USA), and two ICIs, Ipilimumab and Nivolumab (Sellerchem, Houston, USA). To assess optimal drug concentration, initially MCTS were aggregated with a ccRCC:PBMCs 9:1 ratio and treated with 5 concentrations of Sunitinib (1 mM, 5 mM, 10 mM, 15 mM and 20 mM) and 4 concentrations of ICIs (10 μg/ml, 33.3 μg/ml, 56.6 μg/ml and 80 μg/ml) for 7 days. When the optimal concentration for each drug was assessed, hydrogel samples were organised according to the scheme reported in **Table 1**. Additional controls, specifically Ctrl PBS and Ctrl DMSO, were included in the sample cohort to evaluate whether the solutions used to dissolve the drugs (0.8% PBS for ICIs and 0.1% DMSO for the TKI) exhibited any cytotoxic effects on the cells.

Cell type	Treatment	Sample name
ccRCC	Complete medium	IF (Immune Free)
ccRCC:PBMCs (9:1)	Complete medium	CC (Co-Cultured)
ccRCC:PBMCs (9:1)	0.8% PBS	Ctrl PBS
ccRCC:PBMCs (9:1)	0.1% DMSO	Ctrl DMSO
ccRCC:PBMCs (9:1)	Ipilimumab	Ipilimumab
ccRCC:PBMCs (9:1)	Nivolumab	Nivolumab
ccRCC:PBMCs (9:1)	Sunitinib	Sunitinib

Table 1. Panel of generated samples and their corresponding pharmacological treatments. Each sample is listed with its assigned name.

Cell culture monitoring

Medium replacement was performed at discrete timepoints (Day 3, Day 7) by removing half of the exhausted medium and replacing it with fresh complete medium. Exhausted medium (Day 3, Day 7, Day 10) was collected and stored at -80°C for proteomics and metabolomics analysis. Cell cultures were monitored daily through visual examination under the inverted Zeiss Primovert microscope. Moreover, for each selected timepoint, cell viability was determined by Presto Blue Cell Viability reagent; specifically, after a 90-minute incubation, fluorescence was measured at 550/600 nm using a microplate reader (Infinite M Plex, Tecan Group Ltd., Zürich, Switzerland). For each timepoint, some hydrogels were harvested and washed with Phosphate-Buffer Saline (PBS) to wash away medium, and subsequently fixed with formalin for a total of 30 min. After fixation, samples were embedded in paraffin to obtain FFPE blocks.

Histological staining

FFPE samples were sectioned at a 4 μm-thickness and mounted onto Superfrost slides. After deparaffinisation and rehydration, the sections were either stained using haematoxylin and eosin to observe morphology or subjected to immunohistochemical staining to assess cell proliferation (marker Ki67, clone 8F5, CTS Antibody) and immune cell presence (marker CD45, clone D9M8I, CST Antibody) throughout time. Briefly, endogenous peroxidase was blocked for 20 minutes with 0.3% H2O2 in methanol (Merck Millipore, Burlington, MA, USA) and subsequently antigen retrieval was performed by boiling the sections in 10mM citrate buffer (pH 6) for 10 minutes. After tissue blocking with SuperblockTM Blocking Buffer (Thermofisher scientific), sections were incubated with a primary antibody (Ki67: 1:100; CD45: 1:200) overnight at 4°C. The next day, the primary antibody was visualised by incubation with BrightVision poly-horseradish peroxidase (Immunologic, Duiven, The Netherlands) for 30 minutes, followed by development using the DAB+ chromogen (DAKO, Agilent Technologies, Santa Clara, CA, USA) for 5 minutes. Slides were counterstained with haematoxylin. After histological staining, slides were converted to digital format using a Vectra 3.0 Automated Quantitative Pathology Imaging System (Perkin Elmer).

UHPLC-ESI-MS/MS analysis of polar metabolites

Culture medium was removed from -80°C storage and placed on ice. Extraction was performed by adding 60 μL of cold LC-MS grade-LiChrosolv® acetonitrile (Merck KGaA, Darmstadt, Germany) to 15 μL of medium, followed by 30 seconds of vortex mixing. The samples were then centrifuged for 5 minutes at 4°C and 13,000 rpm (Centrifuge 5424 R, Eppendorf, Hamburg,

Germany). The supernatants were recovered, samples were freeze-dried at RT using the HetoVac VR-I (A. De Mori, Milan, Italy) and reconstituted with 75 µL of ACN/H_2O (50/50 v/v) for polar metabolite analysis, as these represent low-molecular-weight signalling molecules that potentially contribute to cell–cell communication, metabolic crosstalk, and microenvironment modulation. Quality control (QC) samples were prepared by pooling 10 µL of each sample.

The UHPLC-MS platform for the analysis consisted of an Agilent 1290 II liquid chromatography system coupled to a quadrupole time-of-flight mass spectrometer (Agilent 6546 LC/Q-TOF - Agilent Technologies, Palo Alto, CA, USA). Chromatographic separation was performed using an InfinityLab Poroshell 120 HILIC-Z (2.1 × 150 mm, 2.7 µm) column (Agilent Technologies, Palo Alto, CA, USA) equipped with a UHPLC InfinityLab Poroshell 120 HILIC (2.1 × 5 mm, 2.7 µm) guard column. Mobile phase A consisted of 20 mM ammonium acetate and 5 µM medronic acid (Sigma-Aldrich/Merck, Darmstadt, Germany) in LC-MS-LiChrosolv® H_2O (Merck KGaA, Darmstadt, Germany). Mobile phase B was made of ACN 100%. The following solvent gradient was used to elute the samples: 0 min 90% B, 1 min 90% B, 8 min 78% B, 12 min 60% B, 15 min 10% B, 18 min 10% B, 23 min 90% B, at a flow rate of 0.4 ml/min. The analysis was performed in both positive and negative ionisation modes, with injection volumes of 2 µL and 5 µL, respectively. The resolution was set to 40,000 FWHM with a full scan range of m/z 40-1200. Samples were analysed as technical triplicate. QCs were injected every six injections to monitor the performance of the analysis. Five QCs were added at the end of the worklist to gather MS/MS spectra using an iterative approach for data-dependent analysis (DDA). Agilent LC-MS platform was operated using Data Acquisition (Agilent Technologies, Santa Clara, CA, USA).

Feature annotation was accomplished with MassHunter Profinder (Agilent Technologies, Santa Clara, CA, USA). The in-house library for polar

metabolites was built through five consecutive injections of QC samples in DDA mode, utilised to acquire MS/MS data. The library was based on accurate mass, MS/MS fragmentation, isotopic pattern, and retention time, and using online databases (HMDB [10.1093/nar/gkx1089] and METLIN [10.1021/acs.analchem.7b04424]). Samples analysed in full scan mode were matched with our in-house library according to mass formula, isotope pattern, and retention time and integrated with MassHunter Personal Compound Database and Library (PCDL) Manager Software (Agilent Technologies, Santa Clara, CA, USA).

Label-free quantitative proteomics with nLC-ESI-MS/MS

For each selected timepoint and condition, culture media samples were treated with DL-Dithiothreitol (DTT) (Sigma-Aldrich, St. Louis, MO, USA, ≥99.5%) at a final concentration of 10 mM and incubated for 45 min at 56°C. Then, iodoacetamide (IAA) (Sigma-Aldrich, St. Louis, MO, USA) at a final concentration of 20 mM was added, and the samples were left at room temperature in the dark for 30 min for the carbamidomethylation reaction. Proteins were enzymatically digested by adding 2 µg of trypsin (trypsin from porcine pancreas, Sigma-Aldrich, St. Louis, MO, USA) and were incubated overnight at 37°C. The enzymatic reaction was stopped by adding formic acid (FA) (LiChropur®, Merck KGaA, Darmstadt, Germany) to reach an acidic pH (<2). Peptide content was quantified by using a Nanodrop spectrophotometer (NanoDrop OneC, Thermo Scientific, Wilmington, DE, USA).

Samples were analysed in triplicate with Evosep One (Evosep Biosystems, Odense, Denmark) LC system coupled online with timsTOF fleX™ (Bruker Daltonics, Bremen, Germany) mass spectrometer, as already reported (with some modifications)[40]. Peptides were loaded into a disposable trap

column, Evotip Pure™ (Evosep Biosystems, Odense, Denmark) following the manufacturer protocol. Desalted and concentrated peptides were separated into an analytical 15 cm column (PepSep C18, 15 cm Performance column, particle size of 1.5 μm and internal diameter of 150 μm) at a temperature of 40°C. A gradient of 44 minutes (30 SPD) with solvent A (0.1 % FA) and solvent B (ACN + 0.1 % FA) was used for the separation. The eluted peptides were ionised using a nanoCaptiveSpray™ (Bruker Daltonics, Bremen, Germany). The mass spectrometer was operated in DIA (Data Independent Acquisition)-PASEF (Parallel Accumulation-Serial Fragmentation) mode. Ions were scanned in positive mode, over an *m*/*z* of 100-1700 and a mobility range of 0.60-1.60 V·s/cm². Dry gas flow was 3.0 l/min at 180°C and capillary voltage was 1400 V. For tandem mass PASEF analysis, the cluster of mono-charged ions was excluded to reduce the complexity of MS2 spectra using the following parameters: mass range 300-1201 Da and 0.60-1.43 $1/K_0$, the estimated cycle time for each PASEF analysis was 1.8 seconds with a total of 16 cycles using DIA windows of 26 Da. The mass spectrometer was calibrated for mass accuracy using a mix of ten standards with known mass (MMI-L Low Concentration Tuning Mix, Agilent Technologies, Santa Clara, CA, USA). With nano- source, mass and ion mobility calibration was performed with three specific lock masses (*m*/*z* 622.0290, *m*/*z* 922.0098, and *m*/*z* 1221.9906) applied on a filter.

Raw data were elaborated by using the PEAKS® Studio 12.5 platform following a library-free processing method based on Human database (Swissprot, downloadED on September 2024). The parameters were set as follows: Trypsin as enzyme, carbamidomethylation (C) as the fixed modification, acetylation (protein N-term) and oxidation (M) as the variable modifications. An FDR of 1% at the peptide level and a -10logP ≥ 13 at the protein level was considered; Proteins were considered identified only if

supported by at least one significantly matched proteotypic peptide. For label-free quantification, only proteins with at least two unique peptides were included.

Statistical analysis

The statistical analysis of continuous variables measured during cell culture monitoring (absorbance, radial distance, spheroid size) was carried out with GraphPad Prism 5 (GraphPad Software Inc., California, USA). For the metabolomics dataset, the statistical analysis was conducted with MetaboAnalyst 6.0[41], an open-source platform for the analysis of metabolomics datasets. Sample normalisation was preliminarily carried out (Sum), along with data transformation (Log transformation). Subsequently, Student's t-test was performed to highlight metabolites which were significantly up or downregulated in samples ($p < 0.05$). A quantitative enrichment analysis was also performed, selecting SMPDB as metabolite set library. The proteomics dataset was analysed in MetaboAnalyst 6.0 after performing data transformation (Log transform). A t-test was used to highlight statistically significant alteration among samples ($p < 0.05$), and subsequently identified proteins were inputted onto STRING[42], an open-source database of known and predicted protein-protein interactions, to perform a network analysis. Lastly, those proteins that emerged as being statistically altered among samples were utilised to perform a quantitative functional enrichment analysis with the open-source platform g:Profiler[43] (g:GOSt Functional profiling; show all results; significance threshold: gSCS threshold; user threshold: 0.05).

Results

Optimisation of aggregation and treatment parameters

Cell density tests were conducted using three ccRCC cell lines, SK-RC-1, SK-RC-7, and 786-O, to pinpoint a cell density that could support continuous proliferation over a 10-day period without reaching a plateau. The extended culture time was chosen to account for the prolonged half-life of ICIs[44,45]. Results are shown in **Supplementary Information, S1**. The homogeneity of spheroids formed by each cell line was assessed using a Presto Blue assay, based on the assumption that spheroid metabolic activity is proportional to cell count. **Figure 1.a** displays results obtained on twenty spheroids for each cell line. Specifically, SK-RC-1 spheroids had a mean fluorescence of 13958 ± 1964 (mean ± st.dev.), SK-RC-7 spheroids of 16388 ± 4371 and 786-O spheroids of 3337 ± 1640. Notably, 786-O spheroids demonstrated a lower standard deviation, indicating higher uniformity, though their reduced absorbance relative to the other lines reflects the lower seeding density of 1000 cells/well.

Following these preliminary assessments, MCTS composed of ccRCC cells and PBMCs at a 9:1 ratio, which is within the range commonly used[28,46], were aggregated using the optimised cell densities to assess optimal treatment concentrations. MCTS were subsequently treated with three drugs (Ipilimumab, Nivolumab, and Sunitinib) at five different concentrations. Results of the Presto Blue assay of cell line SK-RC-1 are reported in **Figure 1.b**, whilst results derived from the remaining cell lines are reported in **Supplementary Information, S2.a**. By Day 7, the MCTS began to disaggregate within the wells, prompting the cessation of treatment earlier than the initially planned 10-day period. However, this experiment was useful in determining the optimal concentration for each drug, established as 80 μg/ml for

Ipilimumab and Nivolumab and 20 nM for Sunitinib, considering that these concentrations showed the strongest effects on cell viability compared to untreated controls at Day 7. Notably, 786-O MCTS, which were seeded at a lower density due to prior considerations, reached 0% viability by Day 7 when treated with Sunitinib (**Supplementary information, 2.b**). Altogether, the results indicate that 786-O is not an ideal cell line for long-term pharmacological treatments due to its rapid proliferation rate. Whilst a low cell density is necessary to sustain proliferation over a 10-day period, smaller spheroids were found more susceptible to the toxic effects of drugs such as Sunitinib. When considering SK-RC-1 and SK-RC-7 MCTS, the latter demonstrated higher heterogeneity in terms of spheroid size, whereas SK-RC-1 exhibited lower standard deviation and a more linear response to drug treatment, enabling a higher reproducibility for further experiments (*e.g.*, **S2.b**). Based on these observations, subsequent experiments were performed using spheroids derived from the SK-RC-1 ccRCC cell line. To assess the size of SK-RC-1 spheroids, an inverted microscope was employed to measure the diameter of each of the spheroids, yielding a mean diameter of 436.5 ± 42.1 μm (mean ± st. dev.), as shown in **Figure 1.c**.

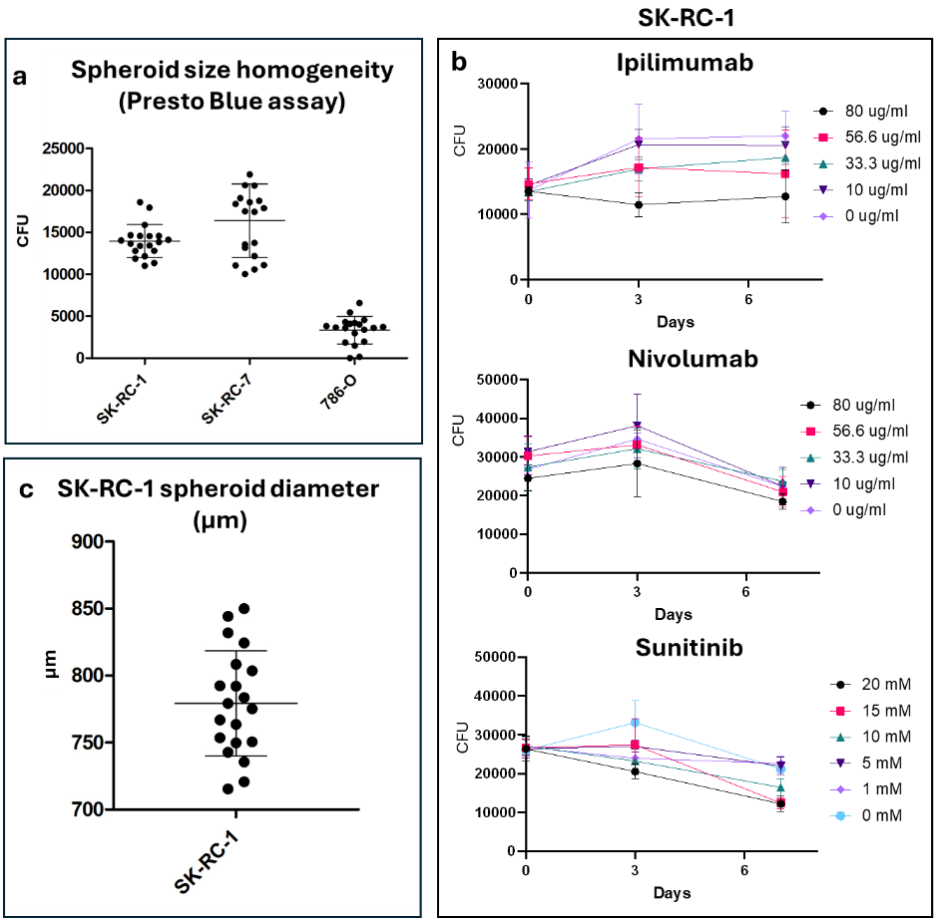

Figure 1. a) Presto Blue assay was used to infer the homogeneity of twenty spheroids of each cell line in terms of size, based on the assumption that metabolic activity is proportional to cell count. **b)** Drug concentration tests performed on the SK-RC-1 cell line utilising four different concentrations for ICIs and five for the TKI. **c)** The diameter of SK-RC-1 spheroids obtained after three days of aggregation was assessed on n = 20 spheroids using an inverted microscope.

Optimisation of ccRCC and PBMC co-culture in hydrogel

SK-RC-1 spheroids were embedded in a hydrogel matrix containing PBMCs at a 9:1 SK-RC-1:PBMCs ratio and treated as described in **Table 1**. The spheroids were cultured within the hydrogel for a total of 10 days, allowing cells to migrate through the ECM-like scaffold. To evaluate cell migration, the maximum radial distance from the spheroid centre to the furthest point of cell expansion (in µm) was measured using an inverted microscope[31]. Over time, cells exhibited migratory behaviour, extending outward from the spheroid and

forming elongated structures within the gel matrix. **Figure 2.a** presents the results of cell migration in non-treated samples (CC, IF), in samples treated with ICIs (Ipilimumab, Nivolumab), and in samples treated with Sunitinib. No statistically significant differences were observed in the migration capacity of control samples and those treated with ICIs. However, spheroids treated with Sunitinib displayed a complete inhibition of cell migration, maintaining their initial size throughout the culture period. ANOVA results confirmed that Sunitinib treatment significantly impaired cell expansion as early as Day 2 (p = 0.003). Representative images captured via inverted microscopy are provided in **Supplementary Information, S3**. At relevant timepoints (Day 0, Day 3, Day 7, and Day 10) a Presto Blue assay was performed to assess metabolic activity. Notably, obtained measures displayed a high variability among replicates (**Figure 2.b**). These results suggest that the diffusion of metabolites within the gel matrix might have been hindered, as evidenced by the non-uniform coloration that was observed within each well after incubation (**Supplementary Information, S4**). However, the resulting findings could also be indicative of an initial cell proliferation up to the third day of co-culture, and subsequently a plateau phase, with a downward trend at Day 10. Moreover, the assay indicates the progressive death of cells treated with Sunitinib, although statistical analysis could not be performed due to the scarcity of replicates. Control samples "Ctrl PBS" and "Ctrl DMSO" did not display a different trajectory in respect to CC, indicating a lack of toxicity of 0.8% PBS and 0.1% DMSO on SK-RC-1 cells. Samples containing only SK-RC-1 cells (IF) demonstrated a decreased absorbance at Day 7, which might indicate a decreased metabolic activity or cellular death. However, for this timepoint only one measurement could be performed on these samples, and therefore this result cannot be considered statistically relevant.

To visualise cell migration over time, H&E staining was performed on FFPE hydrogels obtained at relevant timepoints, as shown in **Figure 2.c**. Consistent with cell observations reported through inverted microscopy, this histological analysis revealed the progressive expansion of SK-RC-1 cells within the hydrogel. Over time, spheroids underwent structural disintegration, giving rise to elongated cell formations and linings, in line with the epithelial phenotype of SK-RC-1 cells. Furthermore, IHC staining was employed to evaluate cell proliferation ($Ki67^{+}$) and the presence of immune cells ($CD45^{+}$) within the hydrogel up to Day 10 (**Figure 2.d-e**). Ki67 staining confirmed sustained proliferation of tumour cells over the entire experimental period, whilst CD45 staining demonstrated the presence of immune cells within the matrix. Nevertheless, despite the co-culture conditions, no chemotaxis or direct cell-cell interactions between tumour and immune cells were observed.

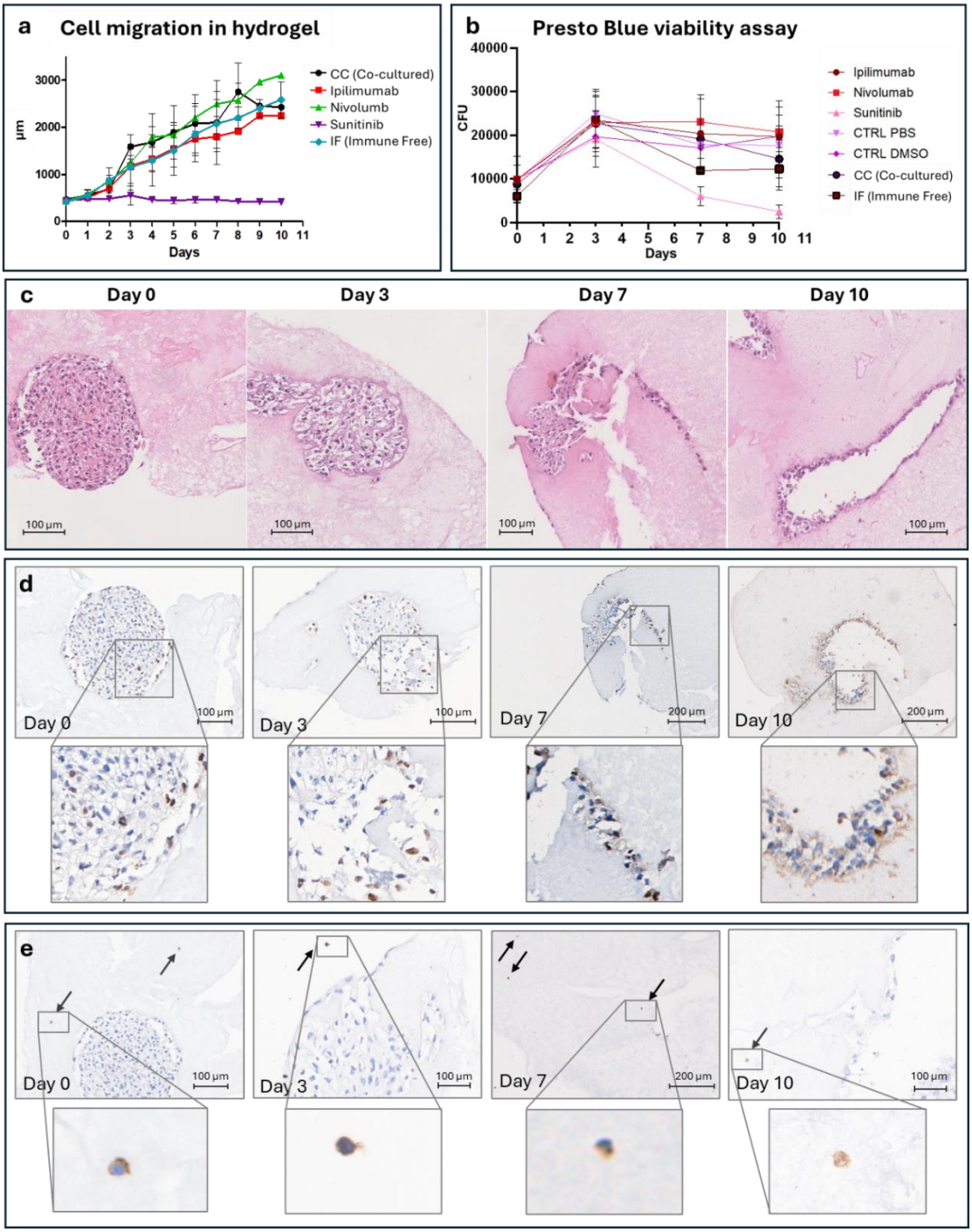

Figure 2. a) Migration of cells within hydrogels, expressed as the maximum radial distance from the spheroid centre to the furthest point of cell expansion (in µm). **b)** A Presto Blue viability assay was performed at relevant timepoints for all samples, indicating progressive death of cells treated with Sunitinib and a decreased absorbance of those samples containing only cancerous cells (IF). **c)** Histological staining with H&E was performed to evaluate cell expansion in hydrogels throughout the culture period. **d)** Immunohistochemistry was performed to assess cell proliferation up to Day 10 (marker: Ki67). **e)** Immunohistochemistry was performed to assess the presence of immune cells up to Day 10 (marker: CD45). Positively stained immune cells are indicated by a black arrow.

Multiomic LC-MS analysis of culture media

Culture media samples were collected on days 3, 7, and 10 after the co-culture of SK-RC-1 cells and PBMCs in hydrogel. Metabolomics and proteomics analyses were performed on the extracellular environment to assess the influence of immune cells and immune checkpoint inhibitors on cell metabolism and ECM remodelling. The complete list of all metabolites and proteins identified is available at **Supplementary Information, T2**. Considering that these analyses were conducted on culture media rather than intact cells, in order to explore alterations in the secretome, the findings rely on the premise that detected compounds were either actively secreted from cells, passively released due to osmotic balance, or already present in the culture medium and consumed to sustain cell metabolism.

1. *Influence of PBMCs on metabolism*

The metabolic changes induced by the presence of PBMCs were assessed by investigating metabolites involved in immune-tumour communication, identified based on literature references and compared between co-cultured samples (CC) and immune free samples (IF). Considering the downward trend in absorbance from Day 7 to Day 10 observed in the Presto Blue assay, which may indicate cellular death, the results from Day 10 are not presented, as cell membrane disruption could lead to the release of cytoplasmic content into the culture media, potentially confounding the analysis. To highlight those metabolic pathways altered by the presence/absence of PBMCs throughout time, a quantitative enrichment analysis was initially performed comparing CC and IF samples. **Figure 3.a** displays the enriched metabolic pathways involved in tumour-immune communication. Of note, most of these demonstrated a higher enrichment at Day 7, including key pathways associated with tumour-

immune cell interaction such as glycolysis, BCAA metabolism (valine, leucine and isoleucine degradation, ketone body metabolism), as well as arachidonic acid, glutamate and tryptophan metabolism. On Day 3, 31 metabolites were found to be significantly altered among CC and IF samples ($p < 0.05$, **Supplementary Information, T3**), 6 of which are known to have a role in tumour-immune cell dynamics (5'-methyladenosine[15,47,48], 5-hydroxyl-L-tryptophan[49], L-tryptophan[50–53], L-arginine[54–56], L-glutamine and alanyl glutamine[15,57–59], **Supplementary Information, S5.a**). On Day 7, 63 metabolites were found significantly altered amongst CC and IF samples (**Supplementary Information, T3**), several of which are involved in the interaction of tumour and immune cells (**Supplementary Information, S5.a**)[60]. Notably, significant changes were observed in metabolites involved in key pathways, such as branched-amino acid (BCAA) metabolism[61,62]. Branched-chain amino acids (BCAAs: valine, leucine, isoleucine) undergo transamination by BCATc and BCATm, generating glutamate and branched-chain α-keto acids (BCKAs: α-ketoisovaleric acid, ketoleucine, and α-keto-β-methylvaleric acid)[18,63,64] which are then further metabolised to acetyl-CoA, acetoacetate, or propionyl-CoA.[65]. CC samples presented an increase in BCKAs, with a decrease of α-ketoglutaric acid, pointing at the catabolism of BCAAs. Moreover, the levels of acetoacetate were also found to be increased, hinting at the further degradation of BCKAs. Interestingly, the byproduct of this pathway, glutamate, was found to be downregulated in the same samples, suggesting its prompt utilisation after production. Typically, in cancer metabolism, glutamate is converted to α-ketoglutaric acid to fuel the reductive TCA cycle[57,58,66]; indeed, various metabolites of the TCA cycle, including α-ketoglutaric acid, succinic acid and malic acid were found downregulated, further corroborating their swift usage in CC samples. This hypothesis is reinforced by pyruvate downregulation coupled to lactic acid increase in CC samples, indicating that pyruvate

produced through glycolysis is preferably converted to lactic acid rather than entering the TCA cycle, triggering the need to fuel this pathway through α-ketoglutaric acid. This metabolic shift towards lactic acid production and α-ketoglutaric acid consumption is summarised in **Supplementary Information, S5.b**. Another relevant result is the upregulation of betaine biosynthesis in CC samples, indicated by a loss of glycine and sarcosine coupled to an increase in dimethylglycine and betaine [67–70]. Finally, oxidative stress could also represent an interesting phenomenon in co-cultured samples, with a 74-fold increase in allantoin, a byproduct of uric acid non-enzymatic oxidation and an oxidative stress marker[71,72]. Intensity box plots of metabolites of interest are reported in **Supplementary Information, S5.a**.

2. *Influence of PBMCs on ECM remodelling*

The influence of PBMCs on ECM remodelling was evaluated through proteomic analysis of the culture media obtained from CC and IF samples. As performed previously, quantitative enrichment analysis was conducted, underscoring the enrichment of coagulation pathways at Day 3 and Day 7, whilst also highlighting that by Day 7 the pathways of cell motility and regulation of cell migration were significantly enriched (**Figure 2.b**). Moreover, the pathway of response to stress was also determined to be enriched, with a slight upregulation at Day 7 with respect to Day 3. On Day 3, 47 proteins were found to be significantly altered, whilst on Day 7, 26 proteins showed a statistically significant variation (**Supplementary Information, T2**). Noteworthy alterations included the upregulation of several intermediate filaments, including keratins (K1C10_HUMAN, K2C14_HUMAN, K1C16_HUMAN, K22E_HUMAN, K2C28_HUMAN, K1C9_HUMAN), tubulins (TBA1A_HUMAN, TBA1B_HUMAN, TBA1C_HUMAN, TBAA3_HUMAN), and vimentin (VIM_HUMAN) at Day 3 in CC samples.

Notably, whilst intermediate filaments are usually involved in cytoskeletal organisation within the cell, their extracellular localisation may be justified by their role as regulators of cell-ECM interactions and mechanotransduction signaling[73,74]. Moreover, at Day 3, an upregulation of keratin K2C16_HUMAN coupled to an upregulation of vimentin in CC samples could be symptomatic of the Epithelial-Mesenchymal Transition (EMT), which is typical of invasive tumours[75,76]. Moreover, at Day 7 CC samples showed an increased presence of laminins (LAMA1_HUMAN, LAMB1_HUMAN, LAMC1_HUMAN), which may be expected considering they are key actors in cell migration[77]. To further explore these results, a network analysis was conducted on those proteins found to be statistically altered at Day 7 (**Figure 2.b**). Results confirmed a positive regulation of the integrin-mediated signalling pathway, extracellular matrix assembly, cell migration, along with ECM-receptor interaction and ECM-proteoglycans. The proteomic analysis of culture media also highlighted several proteins which are known to play a role in blood coagulation and fibrin clot formation, including prothrombin (THRB_HUMAN), Factor V (FA5_HUMAN), plasminogen (PLMN_HUMAN), beta-2-glycoprotein 1 (APOH_HUMAN), fibulin-1 (FBLN1_HUMAN), filamin-A (FLNA_HUMAN), peptidyl-prolyl cis-trans isomerase A (PPIA_HUMAN), talin-1 (TLN1_HUMAN), collagen type III alpha 1 chain (CO3A1_HUMAN), and the von Willebrand factor (VWF_HUMAN)[78]. Specifically, at Day 3 the downregulation of the upstream blood clotting cascade protein Factor V in favour of an upregulation of the downstream prothrombin, in addition to the downregulation of the plasmin precursor plasminogen, suggests an upregulation of the blood coagulation pathway in CC samples. Moreover, the von Willebrand factor, a key facilitator of platelet adhesion to the site of injury, was found upregulated in CC samples at Day 7, further pointing to the activation of the coagulation cascade.

Altogether, these results indicate that by Day 7 the presence of PBMCs induced an upregulation of the coagulation pathway, promoted ECM remodelling and the EMT, potentially leading to an increased cell migration.

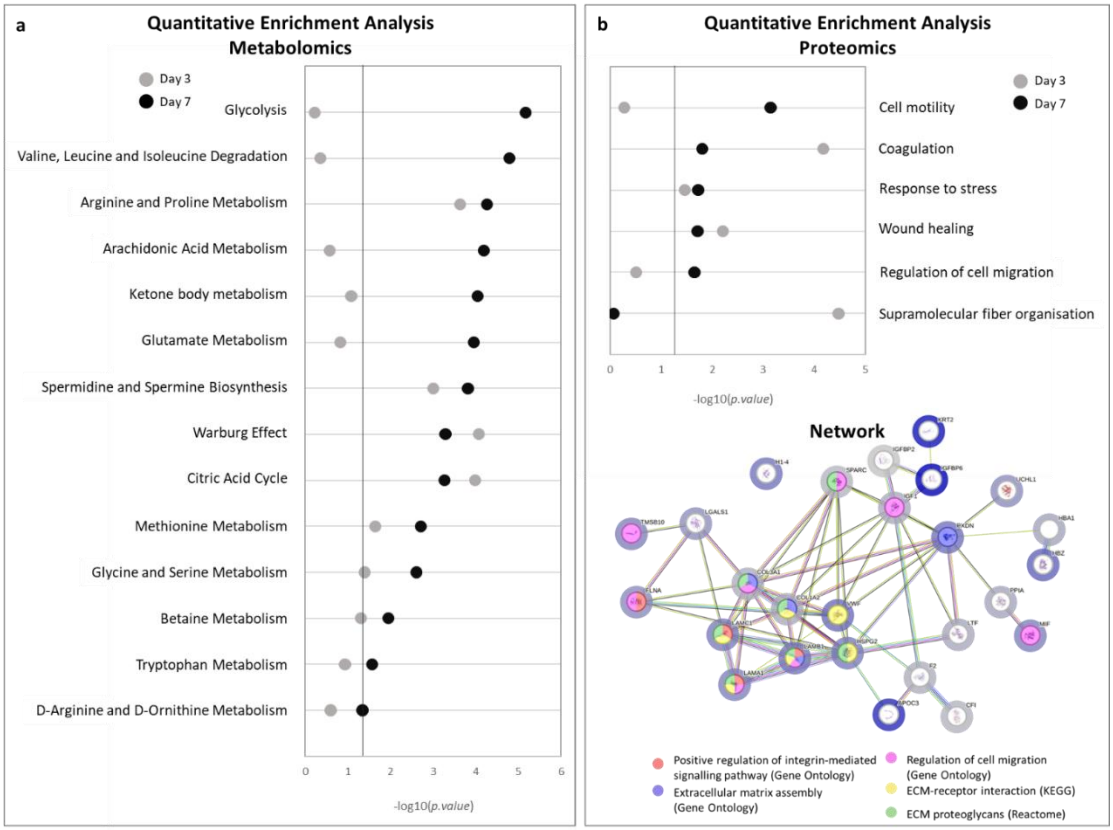

Figure 3 a) Quantitative enrichment analysis obtained at Day 3 (grey) and Day 7 (black) from the metabolomics analysis of CC and IF samples. Among the significantly enriched pathways, here are displayed those that are known to have a role in the interaction of tumour and immune cells. The statistical significance of the enrichment is expressed as $-\log_{10}(p\text{-}value)$ on the x axis. The statistical significance threshold ($p = 0.05$; $-\log_{10}(0.05) = 1.30$) is represented by a vertical line. **b)** (Upper) The dot plot illustrated results from the quantitative enrichment analysis obtained at Day 3 (red) and Day 7 (green) from the proteomics analysis of CC and IF samples. Only pathways enriched in either of the two days are shown. The statistical significance of the enrichment is expressed as $-\log_{10}(p\text{-}value)$ on the x axis. The statistical significance threshold ($p = 0.05$; $-\log_{10}(0.05) = 1.30$) is represented by a vertical line. (Lower) Statistically altered proteins emerged from the proteomic analysis of CC and IF samples (Day 7) are displayed in this protein network. The main biological processes in which these proteins are involved regard positive regulation of integrin-mediated signalling pathway and extracellular matrix assembly.

3. *Influence of Immune Checkpoint Inhibitors on ECM remodelling in the TME*

The potential influence of targeted therapies, such as ICIs, on ECM remodelling remains poorly understood, highlighting a significant gap in knowledge on this topic[19]. To address this, a proteomic analysis of culture media was performed on CC samples and samples treated with ICIs (Ipilimumab and Nivolumab). Results are reported in **Supplementary Information, T2**. On Day 3, samples treated with Ipilimumab demonstrated an upregulation of vimentin, along with several laminins (LAMA1_HUMAN, LAMB1_HUMAN, LAMC1_HUMAN), keratins (K1C10_HUMAN, K1C14_HUMAN, K2C16_HUMAN, K2C1_HUMAN, K2C8_HUMAN) and tubulins (TBA1A/B_HUMAN, TBA1C_HUMAN, TBA3C/D/E_HUMAN, TBA4A_HUMAN, TBA8_HUMAN). Then, on Day 7, a downregulation of cytoskeletal keratins (K1C1_HUMAN, K22E_HUMAN, K1C9_HUMAN) coupled to an upregulation of laminins and vimentin was observed. As previously stated, the upregulation of vimentin coupled to an increase of K2C16_HUMAN is a characteristic of the EMT, and the consequent decrease of keratins, which are cellular markers of the epithelial phenotype, at Day 7 of treatment is another strong indication of a change in cells from an epithelial to a mesenchymal phenotype[75,76] amplified by Ipilimumab. Interestingly, whilst a parallel downregulation of keratins could be demonstrated in Nivolumab-treated samples, both at Day 3 and at Day 7, a corresponding upregulation of vimentin could not be assessed, indicating a more subtle influence of Nivolumab with respect to Ipilimumab on ECM dynamics. Notably, at Day 3, samples treated with Ipilimumab demonstrated a statistically significant downregulation of the tissue factor (TF_HUMAN), the primary initiator of the coagulation cascade[79]. At Day 7, a significant downregulation of von Willebrand Factor (VWF_HUMAN) was observed in the same samples. For samples treated with Nivolumab, this influence on the coagulation cascade

could not be parallelly assessed. Altogether, these findings indicate that Ipilimumab might be exerting a negative regulation of the coagulation cascade on CC samples and a positive regulation of the epithelial-to-mesenchymal transition.

Discussion

Clear cell Renal Cell Carcinoma is an epithelial tumour characterised by significant immune cell infiltration and distinctive metabolic hallmarks whose complex biology remains incompletely understood, presenting challenges for therapeutic targeting and biomarker discovery. In this research paper, a novel approach for co-culturing PBMCs and ccRCC cells to evaluate alterations in metabolism and ECM dynamics was presented. In this model, ccRCC cells were pre-aggregated into a spheroid, which was subsequently embedded in a collagen-based hydrogel containing dispersed allogeneic PBMCs. Allogeneic PBMCs contain an ample panel of immune cells, including lymphocytes, monocytes, dendritic cells, and rarer populations, however, the mismatch of HLA between immune and tumor cells could negatively impact the outcome of the immune response[80]. Moreover, PBMCs culturing is generally associated with difficulty in long-term assessment of immune response, partly due to their activation (AICD: Activation-Induced Cell Death)[81]. In the proposed model, PBMCs derived from 10 healthy donors were pooled to achieve a representative cohort of HLA, minimising limited immune response associated with HLA mismatch. Before co-culturing, PBMCs were not subjected to stimulation, enabling their culture for a longer period of time whilst effectively measuring their baseline response starting from a quiescent state. Whilst this approach is at the early stages of its development, the strength of this methodology lies in its ability to study paracrine interactions of cancer cells and PBMCs for a long-

term period, whilst supporting cell migration within the ECM-like hydrogel, allowing immune and tumour cells to organise spatially and interact in a three-dimensional context. This relatively simple experimental setup advances existing *in vitro* models by more closely recapitulating the complexity of the tumour microenvironment, providing a relevant platform to study immune-tumour crosstalk within the ECM, and the impact of ICIs on these interactions. Moreover, this design permits the harvesting of hydrogels for fixation and embedding, enabling the preparation of sections for further imaging analyses. Immunohistochemistry (IHC) staining with CD45 was performed to assess direct cell-cell interactions within the model. Despite this, PBMCs did not exhibit chemotactic migration toward the tumour spheroid, and the distance between tumour and immune cells was found to be well over the minimum radius required for direct cell contact, estimated at 10-30 μm[82,83]. However, only a small volume of hydrogel (10 μl) was used for embedding, ensuring the placement of immune cells close to the tumour spheroid. Therefore, while not enabling direct cell-cell contact, this setup still allows for paracrine communication via the diffusion of signalling molecules through the matrix and culture medium, considering that the radius of paracrine communication is estimated to extend a few hundred micrometers[84–86].

Indeed, metabolomic analysis of the culture media successfully highlighted pathway alterations induced by the presence of PBMCs within the gel. The quantitative enrichment analysis indicated that at Day 3 key pathways involved in tumour-immune cell communication were shown to be upregulated in CC samples, with their enrichment being even more significant by Day 7, indicating an influence of PBMCs on ccRCC cells driven by paracrine communication. Notably, branched chain amino acid catabolism was altered in CC samples. In cancer, branched-chain amino acid catabolism is upregulated in immune system processes, contributing to lymphocyte expansion, dendritic

cell maturation, and enhanced cytotoxic T cell activity [64,65]. Concurrently, the enhanced conversion of pyruvate in lactic acid (Warburg effect) observed in CC samples from the quantitative enrichment analysis would link BCAA metabolism to the production and prompt utilisation of glutamic acid, which is partly utilised to fuel the TCA cycle through α-ketoglutaric acid production. Whilst the Warburg effect is a well-known characteristic of several cancers, including ccRCC, it was interesting to find it enhanced when PBMCs were present within the hydrogel[87]. Other than its use to support the TCA cycle, glutamate and its amide, glutamine, are key metabolites in the cancer-immune crosstalk, considering that tumour cells increase their usage to foster growth and proliferation, whilst immune cells rely on them for their activation and proliferation[66]. Glutamine's increased uptake from the culture medium in CC samples could be assessed through the significant downregulation of L-alanyl-glutamine (a component of the culture medium), and L-glutamine was also found downregulated at Day 3 and Day 7 in CC samples, confirming this tendency. This metabolic shift suggests that ccRCC cells might exploit BCAA metabolism as an alternative pathway for glutamate synthesis, especially under conditions of glutamine depletion. Moreover, CC samples showed the upregulation of another interesting metabolite, allantoin. In most mammals, allantoin is produced through the catabolism of uric acid catalysed by urate oxidase. In humans, the loss of this enzyme prevents this reaction, and therefore allantoin can only be produced through the non-enzymatic oxidation of uric acid, which occurs in the event of high reactive oxygen species (ROS) content. Therefore, allantoin is considered a urinary biomarker of oxidative stress[72,88]. In ccRCC, as in other tumours, activated immune cells are known to upregulate ROS levels[89,90], upholding the presence of an oxidative stress biomarker in CC samples. This was also confirmed through the quantitative functional enrichment analysis conducted with proteomic data, where the

pathway of response to stress was enriched both at Day 3 and 7 of co-culture. Interestingly, an upregulation of the ROS scavenger glutathione represents a hallmark of ccRCC, and its biosynthesis is limited by the availability of glutamate[91,92]. Taken together, these results suggest that in CC samples the increased need for glutamine ("glutamine addiction"[92]) due to the presence of PBMCs, which enhance the Warburg effect, along with ROS overproduction due to T cell activation, could be triggering an increased need for glutamic acid. Some studies also suggest that glutamine metabolism could be related to Sunitinib resistance in ccRCC, emphasising its importance not only in disease progression, but also in drug efficacy[60,93]. Whilst these preliminary findings require further investigations to confirm this pathway's role under conditions of immune activation, this work underscores the possibility to address these metabolic steps, including glutamine deamination or α-ketoglutaric acid transamination, as potential targets for arresting ccRCC metabolic reprogramming.

The nLC-ESI-MS/MS proteomic analysis of culture media offered provided insights into the influence of PBMCs and ICIs on the epithelial to mesenchymal transition, which is a topic of growing scientific interest yet to be fully elucidated. In ccRCC, the EMT is associated to fibrosis, early recurrence and worse overall survival, prompting its targeting for therapeutics[94,95]. Several studies previously reported that immune cells can actively trigger the EMT in ccRCC through the secretion of chemokines, cytokines and growth factors[96–98]. In this study, signals of EMT were observed by Day 7 of co-culture of ccRCC cells and PBMCs, suggesting an increased motility of these samples in respect to those which only contained ccRCC cells. However, the monitoring of the expansion of cells in the hydrogel could not confirm a statistically significant difference between the motility of CC and IF samples. In future work, the setup could be refined to prompt a longer culture period, to verify whether the

culture of immune and tumour cells induces an increased motility of cells from the spheroid.

Whilst the relationship between immune cells and the EMT in ccRCC has been addressed by previous studies, little is known about the effect of immune checkpoint inhibitors on the shift from an epithelial to a mesenchymal phenotype. In the presented study, Ipilimumab prompted a downregulation of keratins and upregulation of tubulin and vimentin, suggesting that this ICI might be directly involved in the induction of the EMT[99]. In the authors' opinion, this represents a relevant result of the work, and future studies will be conducted to reinforce this preliminary hypothesis. Indeed, previous research has established a strong connection between immune checkpoints (ICs) and EMT, suggesting that ICs may induce EMT, or conversely EMT may induce the upregulation of ICs[100], or even that both may be upregulated in response to similar stimuli[75,101]. Naturally, the upregulation of ICs should make ccRCC more responsive to ICIs like Ipilimumab. This raises the intriguing possibility that EMT could play a direct role in treatment efficacy, whilst Ipilimumab itself might contribute to the upregulation of EMT.

This study also offered some interesting insights on the relationship between blood clotting, immune invasion, and immune treatment. Specifically, several coagulation-related proteins were determined to be enriched in CC samples in respect to samples which only contained tumour cells. Considering that this analysis was conducted on culture medium, which contains foetal bovine serum (FBS), the presence of coagulation proteins in the medium raised the question of whether these proteins could be attributed to the medium composition. Serum is derived from plasma but, by definition, contains nearly absent levels of fibrinogen and clotting factors due to their consumption during clotting. Whilst certain components of the coagulation cascade, such as inactive proenzymes or partially activated factors, may still be present in small

amounts[102], for cell culturing FBS is inactivated at 56°C for 30 min, which triggers protein partial degradation[103]. Based on these premises, it can be concluded with reasonable confidence that the coagulation proteins detected in the media were not contributed by FBS. Therefore, it was initially surprising to find the coagulation cascade pathway enriched in the culture medium of ccRCC cell cultures, considering that most of the proteins of the coagulation cascade are produced by the liver[104]. However, based on literature, aberrant coagulation is a well-established characteristic of advanced ccRCC and contemplates increased TF and prothrombin (or Factor II, F2) expression[105,106]. Interestingly, a recent consensus clustering study conducted by Yang Qiu *et al.* on ccRCC patients from a genome database (TCGA) indicated a strong correlation between the mutational burden of genes involved in the coagulation cascade and the increased infiltration of immune cells[107]. Specifically, the upregulation of MMP9 (a metalloprotease) and F2, was found positively correlated with the density of $CD8^+$, FOXP3, and $CD4^+$ cells. This suggests a strong association between the activation of the coagulation pathway, immune-related pathways, and the advancement of ccRCC. Additionally, Guicao Yin *et al.* confirmed a more extensive hypercoagulable state in advanced ccRCC patients based on clinical data and highlighted, among others, PLG as a possible prognostic factor of ccRCC. In the presented work, several proteins of the coagulation cascade were found altered between conditions, including TF, F2 and PLG, and strong indications of an upregulated coagulation cascade in response to the presence of PBMCs were assessed. These findings confirm the association between the coagulation cascade in ccRCC, which is a marker of malignancy, and the presence of PBMCs in the TME, in *in vitro* models. Interestingly, in this study, the ICI Ipilimumab was found to inhibit the coagulation cascade. This was evidenced by the downregulation of vWF at Day 7 of co-culture, and more notably, by the suppression of TF, a key initiator of the coagulation pathway.

Whilst previous studies have reported alterations in blood clotting associated with ICI treatment, including Ipilimumab, the observed effects have varied. For instance, differences in the pro-coagulant effects of Ipilimumab and Nivolumab have been previously reported and were thought to be due to differences in their molecular targets, CTLA-4 and PD-1, respectively[108]. Although the mechanisms linking ICIs to thrombosis are not yet fully understood, they are thought to involve immune-mediated vasculitis and an increase in platelet-derived microparticles, which can promote activation of the coagulation cascade[108,109]. In contrast to these prior reports, our findings suggest an overall downregulation of coagulation following Ipilimumab treatment. However, in the presented model the intrinsic lack of platelets, platelet-derived microparticles or vasculature hinders a thorough study of the mechanisms linking ICIs and coagulation. Nonetheless, the observation that two ICIs can differentially modulate hemostasis highlights the importance of their distinct immunological mechanisms and supports the hypothesis that target specificity may drive divergent effects on coagulation.

This novel approach to co-culture ccRCC cells and PBMCs within an ECM-like hydrogel scaffold has provided valuable insights into the intricate interactions between immune and tumour cells in the TME. The principal mechanisms proposed to be influenced by the presence of PBMCs are summarised in **Figure 4**. Whilst the methodology is highly promising, there remains room for further refinement and optimisation, especially when considering that this setup opens new avenues for TME exploration. For example, considering the crucial role of fibroblasts in ECM remodelling within the ccRCC microenvironment, future iterations of this model could incorporate fibroblasts to better recapitulate the TME. Additionally, optimising parameters such as the immune-to-tumour cell ratio and integrating chemotaxis-stimulating factors could further improve the physiological relevance of the

system. Importantly, the use of patient-derived cells in this model could enable personalised medicine approaches, allowing for tailored investigations into individual patient tumour biology and responses to therapies. This would not only enhance the translational value of the findings but also contribute to the development of precision oncology strategies. In conclusion, this study represents a significant step forward in understanding the metabolic and ECM dynamics of ccRCC, offering a foundation for more comprehensive models and potential therapeutic interventions.

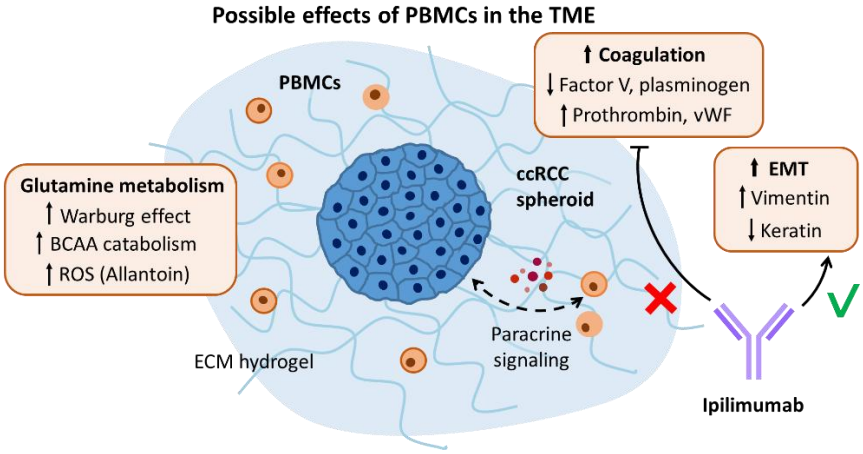

Figure 4) Summary of the possible mechanisms affected by the presence of PBMCs within the ECM hydrogel. Immune cells within the tumour microenvironment (TME) induced the upregulation of coagulation pathway components (*e.g.*, Factor V, plasminogen, prothrombin, vWF) and promoted epithelial-to-mesenchymal transition (EMT), as indicated by increased vimentin and decreased keratin expression. Additionally, alterations in glutamine/glutamate metabolism were inferred based on increased Warburg effect, BCAA catabolism and reactive oxygen species (allantoin). Treatment with the immune checkpoint inhibitor ipilimumab attenuated the immune cell-driven coagulation response whilst further enhancing EMT.

Conclusions

This work presented a novel methodology to study paracrine interactions between ccRCC tumour cells and PBMCs co-cultured in an ECM-mimicking scaffold. This approach proved effective in characterising key metabolic pathway alterations, ECM remodelling, and blood coagulation, which all represent hallmark features of ccRCC that could be exploited as therapeutic targets. Moreover, it also highlighted the influence that key drugs, such as ICIs, may have on metabolism and ECM dynamics, proposing a possible role of Ipilimumab in inducing the epithelial-to-mesenchymal transition and reducing the production of tissue factor. Altogether, the preliminary findings reported in this work highlight the promising potential of this approach and future studies will be conducted in order to consolidate the key observations arising from the study. This will then be directed toward the aim of identifying novel targets for therapeutics and paving the way for more personalised strategies in this area of oncology.

Supporting Information

Supporting Information is available at https://drive.google.com/drive/folders/14ph4fe_yw-6V7AUfRP_knpftR3kLd4iX

References

1. Grigolo, S. & Filgueira, L. Immunotherapy of Clear-Cell Renal-Cell Carcinoma. *Cancers* vol. 16 Preprint at https://doi.org/10.3390/cancers16112092 (2024).
2. Bahadoram, S. *et al.* In Depth Review Renal cell carcinoma: an overview of the epidemiology, diagnosis, and treatment. (2022).
3. Makino, T., Kadomoto, S., Izumi, K. & Mizokami, A. Epidemiology and Prevention of Renal Cell Carcinoma. *Cancers* vol. 14 Preprint at https://doi.org/10.3390/cancers14164059 (2022).
4. Maksimovic, S. *et al.* Antiangiogenic tyrosine kinase inhibitors have differential efficacy in clear cell renal cell carcinoma in bone. *Cancer Research Communications* (2024) doi:10.1158/2767-9764.crc-24-0304.
5. Li, Q., Yang, W., Lu, M. & Zhang, R. Identification of a 6-gene signature associated with resistance to tyrosine kinase inhibitors: Prognosis for clear cell renal cell carcinoma. *Medical Science Monitor* **26**, (2020).
6. Zhuang, T. Z. *et al.* Metastatic Clear-Cell Renal Cell Carcinoma in the Era of Immune Checkpoint Inhibitors: Therapies and Ongoing Trials. *Cancers* vol. 14 Preprint at https://doi.org/10.3390/cancers14122867 (2022).
7. Chen, Y. W. *et al.* Treatment Landscape of Renal Cell Carcinoma. *Current Treatment Options in Oncology* vol. 24 1889–1916 Preprint at https://doi.org/10.1007/s11864-023-01161-5 (2023).
8. Tung, I. & Sahu, A. Immune Checkpoint Inhibitor in First-Line Treatment of Metastatic Renal Cell Carcinoma: A Review of Current Evidence and Future Directions. *Frontiers in Oncology* vol. 11 Preprint at https://doi.org/10.3389/fonc.2021.707214 (2021).
9. Mieville, V., Griffioen, A. W., Benamran, D. & Nowak-Sliwinska, P. Advanced in vitro models for renal cell carcinoma therapy design. *Biochimica et Biophysica Acta - Reviews on Cancer* vol. 1878 Preprint at https://doi.org/10.1016/j.bbcan.2023.188942 (2023).
10. Braun, D. A. & Chakraborty, A. A. *Immunobiology and Metabolic Pathways of Renal Cell Carcinoma*. (2023).
11. Zheng, X., Liu, Y., Yang, Z. & Tian, Y. Metabolic reprogramming and immune microenvironment profiling in clear cell renal cell carcinoma: implications for prognosis, targeted therapy, and drug resistance. *Discover Oncology* **16**, 850 (2025).
12. Shapiro, D. D. *et al.* Understanding the Tumor Immune Microenvironment in Renal Cell Carcinoma. *Cancers* vol. 15 Preprint at https://doi.org/10.3390/cancers15092500 (2023).
13. Monjaras-Avila, C. U. *et al.* The Tumor Immune Microenvironment in Clear Cell Renal Cell Carcinoma. *International Journal of Molecular Sciences* vol. 24 Preprint at https://doi.org/10.3390/ijms24097946 (2023).
14. Martin, S. D., Bhuiyan, I., Soleimani, M. & Wang, G. Biomarkers for Immune Checkpoint Inhibitors in Renal Cell Carcinoma. *Journal of Clinical Medicine* vol. 12 Preprint at https://doi.org/10.3390/jcm12154987 (2023).
15. Zheng, Y. *et al.* Metabolic gatekeepers: harnessing tumor-derived metabolites to optimize T cell-based immunotherapy efficacy in the tumor microenvironment. *Cell Death Dis* **15**, 775 (2024).
16. Zhu, H., Wang, X., Lu, S. & Ou, K. Metabolic reprogramming of clear cell renal cell carcinoma. *Frontiers in Endocrinology* vol. 14 Preprint at https://doi.org/10.3389/fendo.2023.1195500 (2023).
17. Zheng, X., Liu, Y., Yang, Z. & Tian, Y. Metabolic reprogramming and immune microenvironment profiling in clear cell renal cell carcinoma: implications for prognosis, targeted therapy, and drug resistance. *Discover Oncology* **16**, 850 (2025).
18. Wetzel, T. J., Erfan, S. C. & Ananieva, E. A. The emerging role of the branched chain aminotransferases, BCATc and BCATm, for anti-Tumor T-cell immunity. *Immunometabolism (United States)* vol. 5 Preprint at https://doi.org/10.1097/IN9.0000000000000014 (2023).

19. Prakash, J. & Shaked, Y. The Interplay between Extracellular Matrix Remodeling and Cancer Therapeutics. *Cancer Discovery* vol. 14 1375–1388 Preprint at https://doi.org/10.1158/2159-8290.CD-24-0002 (2024).
20. Wei, J., Hu, M., Huang, K., Lin, S. & Du, H. Roles of proteoglycans and glycosaminoglycans in cancer development and progression. *International Journal of Molecular Sciences* vol. 21 1–28 Preprint at https://doi.org/10.3390/ijms21175983 (2020).
21. Xiong, G.-F. & Xu, R. Function of cancer cell-derived extracellular matrix in tumor progression. *J Cancer Metastasis Treat* **2**, 357 (2016).
22. Popova, N. V. & Jücker, M. The Functional Role of Extracellular Matrix Proteins in Cancer. *Cancers* vol. 14 Preprint at https://doi.org/10.3390/cancers14010238 (2022).
23. Winkler, J., Abisoye-Ogunniyan, A., Metcalf, K. J. & Werb, Z. Concepts of extracellular matrix remodelling in tumour progression and metastasis. *Nature Communications* vol. 11 Preprint at https://doi.org/10.1038/s41467-020-18794-x (2020).
24. Kolesnikoff, N., Chen, C. H. & Samuel, M. S. Interrelationships between the extracellular matrix and the immune microenvironment that govern epithelial tumour progression. *Clinical Science* vol. 136 361–377 Preprint at https://doi.org/10.1042/CS20210679 (2022).
25. Sutherland, T. E., Dyer, D. P. & Allen, J. E. The extracellular matrix and the immune system: A mutually dependent relationship. *Science* vol. 379 Preprint at https://doi.org/10.1126/science.abp8964 (2023).
26. Mai, Z., Lin, Y., Lin, P., Zhao, X. & Cui, L. Modulating extracellular matrix stiffness: a strategic approach to boost cancer immunotherapy. *Cell Death and Disease* vol. 15 Preprint at https://doi.org/10.1038/s41419-024-06697-4 (2024).
27. Feng, X. *et al.* Targeting extracellular matrix stiffness for cancer therapy. *Frontiers in Immunology* vol. 15 Preprint at https://doi.org/10.3389/fimmu.2024.1467602 (2024).
28. Rausch, M. *et al.* Characterization of renal cell carcinoma heterotypic 3d co-cultures with immune cell subsets. *Cancers (Basel)* **13**, (2021).
29. Lugand, L. *et al.* Methods for Establishing a Renal Cell Carcinoma Tumor Spheroid Model With Immune Infiltration for Immunotherapeutic Studies. *Front Oncol* **12**, (2022).
30. Shabalina, E. Y. *et al.* The matrix-dependent 3D spheroid model of the migration of non-small cell lung cancer: a step towards a rapid automated screening. *Front Pharmacol* **8**, (2021).
31. Berens, E. B., Holy, J. M., Riegel, A. T. & Wellstein, A. A cancer cell spheroid assay to assess invasion in a 3D setting. *Journal of Visualized Experiments* **2015**, (2015).
32. Duca, D. Del, Werbowetski, T. & Del Maestro, R. F. *Spheroid Preparation from Hanging Drops: Characterization of a Model of Brain Tumor Invasion*. *Journal of Neuro-Oncology* vol. 67 (2004).
33. Nazari, S. S., Doyle, A. D. & Yamada, K. M. Mechanisms of Basement Membrane Micro-Perforation during Cancer Cell Invasion into a 3D Collagen Gel. *Gels* **8**, (2022).
34. Yu, L. *et al.* Core-shell hydrogel beads with extracellular matrix for tumor spheroid formation. *Biomicrofluidics* **9**, (2015).
35. Nazari, S. S. Generation of 3D Tumor Spheroids with Encapsulating Basement Membranes for Invasion Studies. *Curr Protoc Cell Biol* **87**, (2020).
36. Séraudie, I. *et al.* A new scaffold-free tumoroid model provides a robust preclinical tool to investigate invasion and drug response in Renal Cell Carcinoma. *Cell Death Dis* **14**, (2023).
37. Miller, C. P. *et al.* Therapeutic targeting of tumor spheroids in a 3D microphysiological renal cell carcinoma-on-a-chip system. *Neoplasia (United States)* **46**, (2023).
38. Arora, L. *et al.* Development of a Multicellular 3D Tumor Model to Study Cellular Heterogeneity and Plasticity in NSCLC Tumor Microenvironment. *Front Oncol* **12**, (2022).
39. Courau, T. *et al.* Cocultures of human colorectal tumor spheroids with immune cells reveal the therapeutic potential of MICA/B and NKG2A targeting for cancer treatment. *J Immunother Cancer* **7**, (2019).

40. Previtali, P. *et al.* Towards the Definition of the Molecular Hallmarks of Idiopathic Membranous Nephropathy in Serum Proteome: A DIA-PASEF Approach. *Int J Mol Sci* **24**, (2023).
41. Pang, Z. *et al.* MetaboAnalyst 6.0: towards a unified platform for metabolomics data processing, analysis and interpretation. *Nucleic Acids Res* **52**, W398–W406 (2024).
42. Szklarczyk, D. *et al.* The STRING database in 2023: protein-protein association networks and functional enrichment analyses for any sequenced genome of interest. *Nucleic Acids Res* **51**, D638–D646 (2023).
43. Kolberg, L. *et al.* G:Profiler-interoperable web service for functional enrichment analysis and gene identifier mapping (2023 update). *Nucleic Acids Res* **51**, W207–W212 (2023).
44. Liu, J. C. & Yu, H. J. A Review of the Pharmacokinetic Characteristics of Immune Checkpoint Inhibitors and Their Clinical Impact Factors. *Pharmacogenomics and Personalized Medicine* vol. 16 29–36 Preprint at https://doi.org/10.2147/PGPM.S391756 (2023).
45. O'Brien, T. & Dolan, L. Immune checkpoint inhibitors and timing of administration. *The Lancet Oncology* vol. 23 e55 Preprint at https://doi.org/10.1016/S1470-2045(21)00704-X (2022).
46. Li, P., Huang, M., Ma, Y., Zhang, Y. & Shi, C. Novel research model for in vitro immunotherapy: co-culturing tumor organoids with peripheral blood mononuclear cells. *Cancer Cell International* vol. 24 Preprint at https://doi.org/10.1186/s12935-024-03628-3 (2024).
47. Li, Y., Wang, Y. & Wu, P. 5′-methylthioadenosine and cancer: old molecules, new understanding. *Journal of Cancer* vol. 10 927–936 Preprint at https://doi.org/10.7150/jca.27160 (2019).
48. Gjuka, D. *et al.* Enzyme-mediated depletion of methylthioadenosine restores T cell function in MTAP-deficient tumors and reverses immunotherapy resistance. *Cancer Cell* **41**, 1774-1787.e9 (2023).
49. Huang, J. *et al.* L-5-hydroxytryptophan promotes antitumor immunity by inhibiting PD-L1 inducible expression. *J Immunother Cancer* **10**, (2022).
50. Tanaka, M. *et al.* Immune Influencers in Action: Metabolites and Enzymes of the Tryptophan-Kynurenine Metabolic Pathway. *Biomedicines* **9**, 734 (2021).
51. Liu, Z. Q., Ciudad, M. T. & McGaha, T. L. New insights into tryptophan metabolism in cancer. *Trends in Cancer* Preprint at https://doi.org/10.1016/j.trecan.2025.03.008 (2025).
52. Peyraud, F. *et al.* Targeting Tryptophan Catabolism in Cancer Immunotherapy Era: Challenges and Perspectives. *Frontiers in Immunology* vol. 13 Preprint at https://doi.org/10.3389/fimmu.2022.807271 (2022).
53. Kim, M. & Tomek, P. Tryptophan: A Rheostat of Cancer Immune Escape Mediated by Immunosuppressive Enzymes IDO1 and TDO. *Front Immunol* **12**, (2021).
54. Yu, H. *et al.* Tumor microenvironment: Nurturing cancer cells for immunoevasion and druggable vulnerabilities for cancer immunotherapy. *Cancer Letters* vol. 611 Preprint at https://doi.org/10.1016/j.canlet.2024.217385 (2025).
55. Kim, S. H., Roszik, J., Grimm, E. A. & Ekmekcioglu, S. Impact of l-arginine metabolism on immune response and anticancer immunotherapy. *Frontiers in Oncology* vol. 8 Preprint at https://doi.org/10.3389/fonc.2018.00067 (2018).
56. Albaugh, V. L., Pinzon-Guzman, C. & Barbul, A. Arginine—Dual roles as an onconutrient and immunonutrient. *Journal of Surgical Oncology* vol. 115 273–280 Preprint at https://doi.org/10.1002/jso.24490 (2017).
57. Nan, D. *et al.* Glutamine and cancer: metabolism, immune microenvironment, and therapeutic targets. *Cell communication and signaling : CCS* vol. 23 45 Preprint at https://doi.org/10.1186/s12964-024-02018-6 (2025).
58. Jin, J., Byun, J. K., Choi, Y. K. & Park, K. G. Targeting glutamine metabolism as a therapeutic strategy for cancer. *Experimental and Molecular Medicine* vol. 55 706–715 Preprint at https://doi.org/10.1038/s12276-023-00971-9 (2023).

59. Fan, Y. *et al.* Exploiting the Achilles' heel of cancer: disrupting glutamine metabolism for effective cancer treatment. *Frontiers in Pharmacology* vol. 15 Preprint at https://doi.org/10.3389/fphar.2024.1345522 (2024).
60. Qi, X., Li, Q., Che, X., Wang, Q. & Wu, G. The Uniqueness of Clear Cell Renal Cell Carcinoma: Summary of the Process and Abnormality of Glucose Metabolism and Lipid Metabolism in ccRCC. *Frontiers in Oncology* vol. 11 Preprint at https://doi.org/10.3389/fonc.2021.727778 (2021).
61. Cai, Z. *et al.* Branched-chain ketoacids derived from cancer cells modulate macrophage polarization and metabolic reprogramming. *Front Immunol* **13**, (2022).
62. Peng, H., Wang, Y. & Luo, W. Multifaceted role of branched-chain amino acid metabolism in cancer. *Oncogene* vol. 39 6747–6756 Preprint at https://doi.org/10.1038/s41388-020-01480-z (2020).
63. Ichihara, A. & Koyama, E. *Transaminase of Branched Chain Amino Acids I. Branched Chain Amino Acids-a-Ketoglutarate Transaminase*. *The Journal of Biochemistry* vol. 59 https://academic.oup.com/jb/article/59/2/160/895484 (1966).
64. Xu, E., Ji, B., Jin, K. & Chen, Y. Branched-chain amino acids catabolism and cancer progression: focus on therapeutic interventions. *Frontiers in Oncology* vol. 13 Preprint at https://doi.org/10.3389/fonc.2023.1220638 (2023).
65. Blair, M. C., Neinast, M. D. & Arany, Z. Whole-body metabolic fate of branched-chain amino acids. *Biochemical Journal* vol. 478 765–776 Preprint at https://doi.org/10.1042/BCJ20200686 (2021).
66. Wang, B., Pei, J., Xu, S., Liu, J. & Yu, J. A glutamine tug-of-war between cancer and immune cells: recent advances in unraveling the ongoing battle. *Journal of Experimental and Clinical Cancer Research* vol. 43 Preprint at https://doi.org/10.1186/s13046-024-02994-0 (2024).
67. Zhao, G. *et al.* Betaine in inflammation: Mechanistic aspects and applications. *Frontiers in Immunology* vol. 9 Preprint at https://doi.org/10.3389/fimmu.2018.01070 (2018).
68. Grunewald, R. W. & Eckstein, A. *Osmotic Regulation of the Betaine Metabolism in Immortalized Renal Cells*. *Kidney International* vol. 48 (1995).
69. Xie, H. *et al.* The association of serum betaine concentrations with the risk of new-onset cancers: results from two independent nested case-control studies. *Nutr Metab (Lond)* **20**, (2023).
70. Day, C. R. & Kempson, S. A. Betaine chemistry, roles, and potential use in liver disease. *Biochimica et Biophysica Acta - General Subjects* vol. 1860 1098–1106 Preprint at https://doi.org/10.1016/j.bbagen.2016.02.001 (2016).
71. Kand'ár, R. & Žáková, P. Allantoin as a marker of oxidative stress in human erythrocytes. *Clin Chem Lab Med* **46**, 1270–1274 (2008).
72. Martinez-Moral, M. P. & Kannan, K. Allantoin as a Marker of Oxidative Stress: Inter- and Intraindividual Variability in Urinary Concentrations in Healthy Individuals. *Environ Sci Technol Lett* **6**, 283–288 (2019).
73. Infante, E. & Etienne-Manneville, S. Intermediate filaments: Integration of cell mechanical properties during migration. *Frontiers in Cell and Developmental Biology* vol. 10 Preprint at https://doi.org/10.3389/fcell.2022.951816 (2022).
74. Sanghvi-Shah, R. & Weber, G. F. Intermediate filaments at the junction of mechanotransduction, migration, and development. *Frontiers in Cell and Developmental Biology* vol. 5 Preprint at https://doi.org/10.3389/fcell.2017.00081 (2017).
75. Gu, Y., Zhang, Z. & ten Dijke, P. Harnessing epithelial-mesenchymal plasticity to boost cancer immunotherapy. *Cellular and Molecular Immunology* vol. 20 318–340 Preprint at https://doi.org/10.1038/s41423-023-00980-8 (2023).
76. Takan, I., Karakülah, G., Louka, A. & Pavlopoulou, A. "In the light of evolution:" keratins as exceptional tumor biomarkers. *PeerJ* **3**, (2023).

77. Aleman, J. D., Young, C. D., Karam, S. D. & Wang, X. J. Revisiting laminin and extracellular matrix remodeling in metastatic squamous cell carcinoma: What have we learned after more than four decades of research? *Mol Carcinog* **62**, 5–23 (2023).
78. Palta, S., Saroa, R. & Palta, A. Overview of the coagulation system. *Indian Journal of Anaesthesia* vol. 58 515–523 Preprint at https://doi.org/10.4103/0019-5049.144643 (2014).
79. Mackman, N. Role of tissue factor in hemostasis, thrombosis, and vascular development. *Arteriosclerosis, Thrombosis, and Vascular Biology* vol. 24 1015–1022 Preprint at https://doi.org/10.1161/01.ATV.0000130465.23430.74 (2004).
80. Li, P., Huang, M., Ma, Y., Zhang, Y. & Shi, C. Novel research model for in vitro immunotherapy: co-culturing tumor organoids with peripheral blood mononuclear cells. *Cancer Cell International* vol. 24 Preprint at https://doi.org/10.1186/s12935-024-03628-3 (2024).
81. Mehta, P. H. *et al.* Choice of activation protocol impacts the yield and quality of CAR T cell product, particularly with older individuals. *Clin Transl Immunology* **13**, (2024).
82. Liu, X. *et al.* Spatial heterogeneity of infiltrating immune cells in the tumor microenvironment of non-small cell lung cancer. *Transl Oncol* **50**, 102143 (2024).
83. Maffuid, K. & Cao, Y. Decoding the Complexity of Immune–Cancer Cell Interactions: Empowering the Future of Cancer Immunotherapy. *Cancers* vol. 15 Preprint at https://doi.org/10.3390/cancers15164188 (2023).
84. Francis, K. & Palsson, B. O. *Effective Intercellular Communication Distances Are Determined by the Relative Time Constants for Cytochemokine Secretion and Diffusion (Cell Signalingbioreactor Designtissue Engineering)*. vol. 94 www.pnas.org. (1997).
85. Kornberg, T. B. Distributing signaling proteins in space and time: the province of cytonemes. *Current Opinion in Genetics and Development* vol. 45 22–27 Preprint at https://doi.org/10.1016/j.gde.2017.02.010 (2017).
86. Kuraitis, D., Giordano, C., Ruel, M., Musarò, A. & Suuronen, E. J. Exploiting extracellular matrix-stem cell interactions: A review of natural materials for therapeutic muscle regeneration. *Biomaterials* vol. 33 428–443 Preprint at https://doi.org/10.1016/j.biomaterials.2011.09.078 (2012).
87. Kornberg, M. D. The immunologic Warburg effect: Evidence and therapeutic opportunities in autoimmunity. *Wiley Interdisciplinary Reviews: Systems Biology and Medicine* vol. 12 Preprint at https://doi.org/10.1002/wsbm.1486 (2020).
88. Il'yasova, D., Scarbrough, P. & Spasojevic, I. Urinary biomarkers of oxidative status. *Clinica Chimica Acta* vol. 413 1446–1453 Preprint at https://doi.org/10.1016/j.cca.2012.06.012 (2012).
89. Kennel, K. B. & Greten, F. R. Immune cell - produced ROS and their impact on tumor growth and metastasis. *Redox Biol* **42**, (2021).
90. Liu, H. *et al.* A reactive oxygen species–related signature to predict prognosis and aid immunotherapy in clear cell renal cell carcinoma. *Front Oncol* **13**, (2023).
91. Xiao, Y. & Meierhofer, D. Glutathione metabolism in renal cell carcinoma progression and implications for therapies. *International Journal of Molecular Sciences* vol. 20 Preprint at https://doi.org/10.3390/ijms20153672 (2019).
92. Aboud, O. A. *et al.* Glutamine addiction in kidney cancer suppresses oxidative stress and can be exploited for real-time imaging. *Cancer Res* **77**, 6746–6758 (2017).
93. Zhang, Q. *et al.* Decoding sunitinib resistance in ccRCC: Metabolic-reprogramming-induced ABAT and GABAergic system shifts. *iScience* **27**, (2024).
94. Landolt, L. *et al.* Clear Cell Renal Cell Carcinoma is linked to Epithelial-to-Mesenchymal Transition and to Fibrosis. *Physiol Rep* **5**, (2017).
95. Ge, Y. *et al.* Integrating bioinformatic analysis and detailed experiments reveal an EMT-related biomarker for clear cell renal cell carcinoma. *Cancer Med* **12**, 19320–19336 (2023).
96. Zhu, S. *et al.* Construction of an Epithelial-Mesenchymal Transition-Related Model for Clear Cell Renal Cell Carcinoma Prognosis Prediction. *Dis Markers* **2022**, (2022).

97. Chou, M. Y. & Yang, M. H. Interplay of immunometabolism and epithelial–mesenchymal transition in the tumor microenvironment. *International Journal of Molecular Sciences* vol. 22 Preprint at https://doi.org/10.3390/ijms22189878 (2021).
98. Zhang, J., Hu, Z., Horta, C. A. & Yang, J. Regulation of epithelial-mesenchymal transition by tumor microenvironmental signals and its implication in cancer therapeutics. *Seminars in Cancer Biology* vol. 88 46–66 Preprint at https://doi.org/10.1016/j.semcancer.2022.12.002 (2023).
99. Huang, Y., Hong, W. & Wei, X. The molecular mechanisms and therapeutic strategies of EMT in tumor progression and metastasis. *Journal of Hematology and Oncology* vol. 15 Preprint at https://doi.org/10.1186/s13045-022-01347-8 (2022).
100. Redfern, A. D., Spalding, L. J. & Thompson, E. W. The Kraken Wakes: induced EMT as a driver of tumour aggression and poor outcome. *Clin Exp Metastasis* **35**, 285–308 (2018).
101. Cordani, M. *et al.* Immune checkpoints between epithelial-mesenchymal transition and autophagy: A conflicting triangle. *Cancer Lett* **585**, (2024).
102. Lee, D. Y. *et al.* Review of the Current Research on Fetal Bovine Serum and the Development of Cultured Meat. *Food Science of Animal Resources* vol. 42 775–799 Preprint at https://doi.org/10.5851/kosfa.2022.e46 (2022).
103. Simon, J. *et al.* Protein denaturation caused by heat inactivation detrimentally affects biomolecular corona formation and cellular uptake. *Nanoscale* **10**, 21096–21105 (2018).
104. Eshmuminov, D. *et al.* Synthesis of coagulation factors during long-term ex situ liver perfusion. *Artif Organs* **46**, 273–280 (2022).
105. Puzanov, G. A. Identification of key genes of the ccRCC subtype with poor prognosis. *Sci Rep* **12**, (2022).
106. Yang, H. *et al.* Exploring the mechanism of clear cell renal cell carcinoma metastasis and key genes based on multi-tool joint analysis. *Gene* **720**, (2019).
107. Qiu, Y. *et al.* Exploring the role of coagulation-related genes in renal cell carcinoma: Implications for tumor microenvironment and prognostic biomarkers. *Comput Biol Chem* **110**, (2024).
108. Patalakh, I. *et al.* Influence of the Immune Checkpoint Inhibitors on the Hemostatic Potential of Blood Plasma. *Transfusion Medicine and Hemotherapy* (2024) doi:10.1159/000535926.
109. Wang, T. F., Khorana, A. A. & Carrier, M. Thrombotic complications associated with immune checkpoint inhibitors. *Cancers* vol. 13 Preprint at https://doi.org/10.3390/cancers13184606 (2021).

1.4 Conclusions to Chapter 1

Among the hallmarks of clear cell Renal Cell Carcinoma, a high degree of immune infiltration remains one of the most distinctive features, particularly given its strong impact on prognosis, relapse, and response to treatment. However, the process of immune infiltration is highly heterogeneous, as different subsets of immune cells, such as $CD4^+$, $CD8^+$, and $FoxP3^+$ cells, can lead to markedly different alterations of the tumour microenvironment, some pro-tumorigenic and others anti-tumorigenic.

Tissue staining approaches, including H&E and immunostaining, provide valuable information regarding the degree and type of immune infiltration but remain insufficient to characterise, on a single tissue slide, the molecular alterations induced by immune cells within the TME in an *omic* manner. In this Chapter, we described a novel approach for immune cell typing and characterisation based on the integration of a targeted spatial approach (MALDI-HiPLEX-IHC) with untargeted spatial proteomics. This work uniquely enabled the visualisation of cell antigen distributions within heterogeneous tissue sections in a highly multiplexed manner, whilst also allowing the correlation of cell populations with their specific proteomic alterations in their native spatial context. This workflow represents a new frontier in cancer immunology, as currently the targeted mapping of diverse immune populations within cancer tissue is hindered by the inherent limitations of immunohistochemistry, which only permits low levels of multiplexing. Moreover, whilst flow cytometry is considered the most widely used approach for immune cell profiling within tumour samples, it also contemplates the destruction of the spatial architecture of tissue, neglecting the reciprocal role that proximal immune and tumour cells can have and how this aspect shapes the responsiveness of the TME to treatment. With the proposed

workflow, not only diverse immune subsets can be mapped simultaneously, but also their specific proteomic alterations can be studied within the same tissue section, enabling correlation between the relative spatial arrangement of cells and their reciprocal influence of their phenotypic characteristics. At single-cell resolution, this approach could enable both immune cell typing and proteomic characterisation for each individual cell, while preserving information about its molecular surroundings. Therefore, future studies will be directed towards the implementation of this approach on a larger sample cohort characterised by different degrees of immune infiltration, whilst enhancing spatial resolution and possibly integrating additional molecular levels.

Whilst patient-derived tumour resections best capture the heterogeneity and diversity of ccRCC, this same complexity makes it difficult to pinpoint the specific mechanisms driving tumour-immune cell communication. Therefore, in a second line of research, we developed three-dimensional co-culture models to study tumour-immune cell interactions in a setting that permits cell migration and reorganisation. Although the proposed setup is relatively elementary, it enables the investigation of tumour-immune dynamics under controlled conditions with several tunable parameters, including ccRCC:PBMC ratio, hydrogel composition, co-culture duration, and treatment concentration. Moreover, this approach uniquely sustains the co-culture of ccRCC cell lines and PBMCs for a longer period of time, which is one of the critical aspects of tumour-immune co-cultures. The feasibility of this model was further confirmed by mass spectrometry analysis of culture media, which revealed metabolic and proteomic pathways modulated by the presence of PBMCs within the hydrogel. Whilst preliminary, this setup represents a step forward in the investigation of tumour-immune dynamics in ccRCC, providing a

biologically relevant platform for the characterisation of this highly complex and heterogeneous disease.

Altogether, the work presented in this Chapter introduces new strategies for the investigation of ccRCC, both through novel analytical workflows and advanced disease models, thereby contributing to the development of precision oncology approaches and laying the foundation for more targeted therapeutic interventions.

Chapter 2: Toward clinical translation.
Mass Spectrometry Imaging for the one-slide detection and typing of Renal Amyloidosis

2.1 Introduction to Chapter 2

"Amyloidosis" is an umbrella term grouping a heterogeneous set of diseases characterised by the extracellular deposition of amyloid at a systemic level. Commonly involved organs include the heart, the lungs, and most importantly the kidneys, with nephropathy being a frequent manifestation of the disease[1,2]. Amyloid deposition is a gradual process that may result from primary or secondary causes; in both cases, the outcome is the buildup of a precursor protein in the form of amyloid plaques composed of insoluble fibrils primarily arranged in antiparallel β-sheets[2-5]. Histological manifestations of renal involvement in amyloidosis are marked by amyloid deposits across all renal compartments, with glomeruli and arterioles being the most frequently and severely affected. As a consequence of glomerular deposition, renal amyloidosis typically presents with heavy proteinuria and nephrotic syndrome, which may progress to renal insufficiency and ultimately End-Stage Renal Disease (ESRD)[5,6]. These manifestations are common to all types of amyloidosis, irrespective of which amyloidogenic protein initiated amyloid deposition. However, the identification of the correct precursor protein, or *amyloid typing*, is pivotal, as different amyloid precursor proteins demand disease-specific treatment.

Amyloid typing is routinely performed with immunohistochemistry, immunofluorescence, and immunoelectron microscopy[1,6,7]. These approaches, singularly or combined, are generally efficient for the typing of renal amyloid. However, they present some common pitfalls which limit their accuracy and, crucially, they represent low-plexed techniques which require several dedicated tissue sections[6–8]. As a consequence, the currently most employed pipeline for amyloid detection and typing often leads to sample depletion, especially considering that a core needle biopsy is between 15-20 mm long with

a diameter of 1-2 mm[9], resulting in sample volumes of only 25-35 mm[3]. LC-MS/MS proteomics is rapidly emerging as an alternative approach for amyloid typing, but it still represents a niche technique which requires qualified personnel and dedicated instrumentation. Moreover, to reach a satisfactory sensitivity, a considerable number of deposits need to be ablated from tissue sections, once again leading to tissue loss[3,7].

In this context, the application of a high-throughput proteomic approach able to simultaneously detect amyloid-specific proteins whilst also taking into account their spatial distribution within renal compartments could represent a valid alternative to detect and type amyloid deposition in a single tissue section, limiting sample depletion.

Based on this premise, the following Chapter will discuss the potential of employing MALDI-MSI to perform spatial proteomics on single sections, enabling the simultaneous detection and typing of amyloid deposits within a defined workflow. In the first proof-of-concept study, formalin-fixed renal biopsies are subjected to spatial proteomics to detect deposits through a molecular approach based on the mapping of amyloid *fingerprint* proteins. The obtained proteomic profile, indicative specifically of the amyloid deposits, is then used to measure the relative abundance of the principal amyloid precursor proteins within the deposits, allowing for amyloid typing. To extend the applicability of the workflow, a second study explores the feasibility of MALDI-MSI on samples processed with Bouin's fixative, commonly used in nephropathology but not previously analysed with this technique, and fixated for diverse lengths of time. Finally, in a third study, a larger cohort of light chain amyloidosis samples fixed with either fixatives and sourced from two separate clinical centres is analysed to confirm the preliminary findings and to demonstrate the possibility to integrate the approach with a novel digital pathology-based computational method for amyloid detection.

References

1. Ihne, S. *et al.* Review article amyloidosis—the diagnosis and treatment of an underdiagnosed disease. *Dtsch Arztebl Int* 117, 159–166 (2020).
2. Wechalekar, A. D., Gillmore, J. D. & Hawkins, P. N. Systemic amyloidosis. *The Lancet* vol. 387 2641–2654 Preprint at https://doi.org/10.1016/S0140-6736(15)01274-X (2016).
3. Winter, M., Tholey, A., Kristen, A. & Röcken, C. MALDI Mass Spectrometry Imaging: A Novel Tool for the Identification and Classification of Amyloidosis. *Proteomics* 17, (2017).
4. Winter, M., Tholey, A., Krüger, S., Schmidt, H. & Röcken, C. MALDI-Mass Spectrometry Imaging Identifies Vitronectin as a Common Constituent of Amyloid Deposits. *Journal of Histochemistry and Cytochemistry* 63, 772–779 (2015).
5. Kidd, J. & Carl, D. E. Renal amyloidosis. *Current Problems in Cancer* vol. 40 209–219 Preprint at https://doi.org/10.1016/j.currproblcancer.2016.08.002 (2016).
6. Gupta, N., Kaur, H. & Wajid, S. Renal amyloidosis: an update on diagnosis and pathogenesis. doi:10.1007/s00709-020-01513-0/Published.
7. Wisniowski, B. & Wechalekar, A. Confirming the diagnosis of amyloidosis. *Acta Haematologica* vol. 143 312–321 Preprint at https://doi.org/10.1159/000508022 (2020).
8. Dasari, S. *et al.* Amyloid Typing by Mass Spectrometry in Clinical Practice: a Comprehensive Review of 16,175 Samples. *Mayo Clin Proc* 95, 1852–1864 (2020).
9. Xu, S. *et al.* Efficacy and safety of percutaneous renal biopsy performed using 18G needle versus 16G needle: a single-center retrospective study. *Int Urol Nephrol* 54, 3255–3261 (2022).

2.2 Spatial resolution of renal amyloid deposits through MALDI-MSI: a combined digital and molecular approach to monoclonal gammopathies

Adapted from:

Bindi, G.[1], Smith, A.[1], Oliveira, G.[1], Eccher, A.[2], Vatrano, S.[3], Alberici, F.[4], Cazzaniga, G.[5], Galimberti, S.[6], Capitoli, G.[6], Magni, F.[1], Pagni, F.[5], L'Imperio, V.[5] (**2024**).
Spatial resolution of renal amyloid deposits through MALDI-MSI: a combined digital and molecular approach to monoclonal gammopathies.
Journal of clinical pathology, *77*(6), 402–410.
https://doi.org/10.1136/jcp-2023-208790

[1] Department of Medicine and Surgery, Proteomics and Metabolomics Units, University of Milano-Bicocca, Monza, Italy
[2] Department of Pathology and Diagnostics, University and Hospital Trust of Verona, Italy
[3] Pathology Unit, ASP Catania, "Gravina" Hospital, Caltagirone, Italy
[4] Nephrology Unit, Spedali Civili Hospital, ASST Spedali Civili di Brescia, Brescia, Italy
[5] Department of Medicine and Surgery, Pathology, University of Milano-Bicocca, IRCCS Fondazione San Gerardo dei Tintori, Monza, Italy
[6] Bicocca Bioinformatics Biostatistics and Bioimaging B4 Centre, School of Medicine and Surgery, University of Milano-Bicocca, Monza, Italy

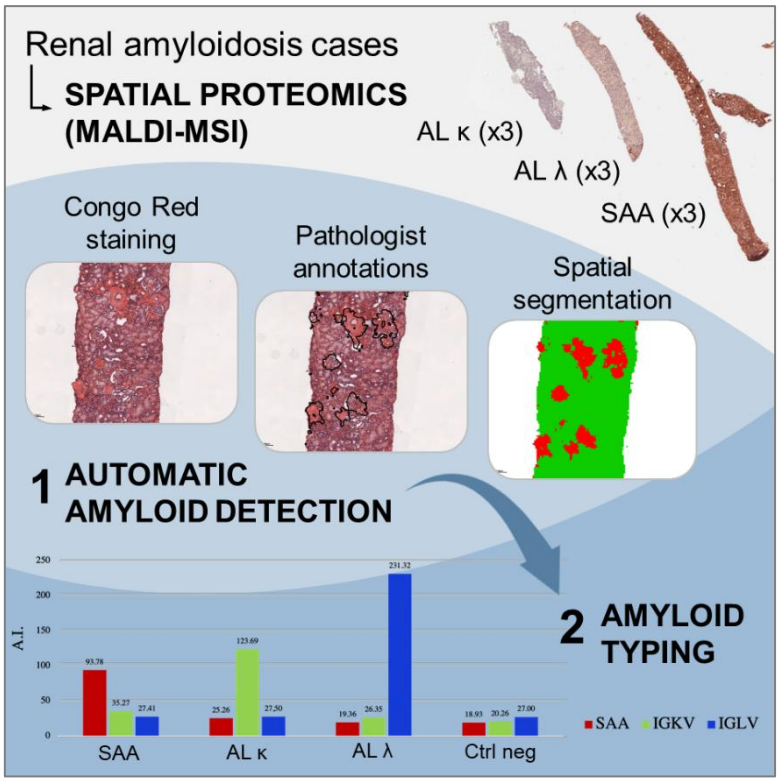

Abstract

The identification and characterisation of monoclonal gammopathies of renal significance (MGRS) are critical to selecting the optimal treatment strategy. Amyloidosis is one of the most common forms of MGRS, and immunofluorescence/immunohistochemistry (IF/IHC) remains the standard approach for its classification. However, proteomics offers a higher sensitivity and enables precise identification of the amyloidogenic protein, or *amyloid typing*. In this study, the potential of an emerging *in situ* proteomic technique, Matrix-Assisted Laser Desorption/Ionisation Mass Spectrometry Imaging (MALDI-MSI), was evaluated as an alternative to conventional Congo red staining combined with IF/IHC for amyloid detection and typing. MALDI-MSI was applied to 16 renal biopsies, including 6 with light chain amyloidosis (AL; 3 AL λ, 3 AL κ), 3 with serum amyloid A (SAA) amyloidosis, 2 with λ light chain deposition disease (LCDD), 2 minimal amyloidosis cases, and 3 negative controls. Pathologists manually annotated amyloid deposits, which were then used as references for automated computational segmentation of amyloid plaques. A panel of diagnostic tryptic peptide fragments was established to optimise automated plaque segmentation. MALDI-MSI successfully detected amyloid precursor proteins within annotated regions, correctly identifying and typing AL κ, AL λ, and SAA cases. Notably, MALDI-MSI also correctly assigned challenging cases with minimal amyloid deposition to AL λ and detected λ light chains in LCDD cases. These results highlight MALDI-MSI as a promising tool for sensitive detection and accurate typing of renal amyloidosis.

Introduction

Renal amyloidosis is a disease characterised by the extracellular deposition of one of many possible amyloid precursor proteins. It can fall under the umbrella of Monoclonal Gammopathies of Renal Significance (MGRS) if monoclonal immunoglobulins produced by white cell dyscrasias (B cells or plasma cells) are deposited within the kidney, leading to the formation of amyloid plaques[1,2]. In the instance of MGRS, the characterisation of the correct precursor is of paramount importance for therapeutic reasons, as cases related to monoclonal components (light chain amyloidosis, AL; heavy chain amyloidosis, AH) should be treated with aggressive chemotherapy[1]. Amyloidosis is conventionally detected by light microscopy (LM), immunofluorescence/immunohistochemistry (IF/IHC), or transmission electron microscopy (TEM)[3]. In challenging cases, such as those containing minimal amyloid deposits, the identification of the correct amyloid precursor protein (amyloid typing) may be compromised by the inherent limitations of IF/IHC[4], leading to a paradigm shift towards more sensitive and specific techniques such as proteomics through laser capture microdissection (LMD) followed by mass spectrometry (MS)[5]. Being an *omic* technique, proteomics simultaneously provides information about precursor proteins (*e.g.*, monoclonal light chains), as well as so-called *fingerprint* proteins (*e.g.*, serum amyloid P component, SAP), which are not causative of amyloidosis but are consistently present within the deposits[6]. Notwithstanding these advantages, LMD-MS requires tissue sections *ad hoc* for the morphological identification of fibrillar deposits with Congo red, which may not always be sufficient to detect subtle or minimal manifestations of the disease and can lead to sample depletion[5,7]. Finally, the lack of histo-molecular correlation caused by tissue destruction during microdissection is another limitation of this approach,

especially in the era of digital spatial profiling[8]. To overcome these limitations, the use of Matrix-Assisted Laser Desorption/Ionisation Mass Spectrometry Imaging (MALDI-MSI) has been proposed as a promising alternative. MSI is a high throughput, MS-based technology used to visualise the spatial distribution of compounds *in situ* in an *omic* manner[9]. Pivotal experiments have already applied MALDI-MSI in the context of renal amyloidosis[10-12]. In 2017, Winter *et al.* assessed the feasibility of MALDI-MSI for the detection and typing of FFPE renal amyloidosis tissue sections at a 200 μm lateral resolution. The study's approach aimed to replace Congo red staining for the identification of amyloid deposits in renal biopsies, whilst detecting the masses of the principal amyloidogenic proteins *in situ*. They showed that the technology was capable of detecting principal amyloid *fingerprint* proteins and precursors, whilst also investigating the proteome of the amyloidotic kidney to broaden understanding of its pathophysiology. Still, despite the suggested feasibility of MALDI-MSI as a novel tool for the diagnosis and subtyping of renal amyloidosis, this work lacked a sufficient lateral resolution to thoroughly investigate the distribution of amyloid associated proteins within glomeruli and other renal compartments. Moreover, the study was not able to identify tryptic peptides derived from immunoglobulin light chains, which represent the most common amyloid precursors. Based on this groundwork, the aim of the present study was to develop an automated pipeline based on MALDI-MSI for the detection and typing of renal amyloidosis on a single tissue slide, including the frequent AL amyloidosis, in the complex molecular background of the kidney.

Materials and Methods

Patient selection

Archival formalin-fixed paraffin-embedded (FFPE) renal biopsies were obtained from the archives of the Department of Nephropathology, Division of Pathology, Fondazione IRCCS San Gerardo dei Tintori, University of Milano-Bicocca (Italy). A total of 16 cases were selected from the open-source Spectrum dataset. These included 9 cases with a defined amyloidosis diagnosis (3 ALλ, 3 ALκ and 3 Serum Amyloid A amyloidosis, SAA; cases #1-9), 2 cases with immunoglobulin λ light chain deposition without concomitant amyloid formation (Light Chain Deposition Disease, LCDD, cases #10, #11), 2 cases of minimal glomerular amyloidosis with insufficient material for IF/IHC typing (cases #12, #13) and 3 cases of IgA nephropathy used as negative controls (cases #14-16). For all cases, a Composite Scarring Injury Score (CSIS) was calculated jointly by two experienced renal pathologists (VL'I and FP) based on the percentage of globally sclerosed (GS) glomeruli and interstitial fibrosis and tubular atrophy (IFTA). In amyloidosis cases, this score was complemented by a previously proposed and validated system consisting in the quantification and localisation of the deposits, the Amyloid Score (AS)[14,15]. Clinical data (sex, age, serum creatinine at diagnosis, proteinuria, and serum/urine monoclonal component, M-spike) was also collected. For continuous variables, mean and SD or quartiles (Q1, median and Q3) were calculated, whereas qualitative variables were expressed as number and frequency. For comparison of means and qualitative variables, t-test and χ^2 test were used as appropriate, and a *p value* of $p < 0.05$ was considered as a statistically significant threshold.

Sample preparation for MALDI-MSI

Four-micrometre-thick sections were cut and mounted on conductive indium tin oxide glass slides. The slides were stored at room temperature until the day of analysis. Each slide was treated according to our previously published method[16], which included deparaffinisation with toluene (3×5 min) and rehydration of the tissue with decreasing concentrations of ethanol and water (100% ethanol 2×5 min, 70% ethanol 1×3 min and high-performance liquid chromatography (HPLC) grade H_2O 2×2 min. Antigen retrieval was performed in a bath containing 10 mM citric acid buffer at 97°C for 45 min before washing the tissue in HPLC-grade H_2O (1×2 min) prior to trypsin application (20 ng/μL) using an iMatrixSpray sprayer (Tardo, Subingen, Switzerland) with an optimised method (heat bed temperature: 37°C; number of spray cycles: 15; enzyme density: 1.2 μL/cm²; movement speed: 160 mm/s; distance between spray lines: 2 mm; needle height: 45 mm). Tissues were incubated overnight at 40°C in a humidity chamber. After enzymatic digestion, matrix deposition was performed by spraying α-cyano-4-hydroxycinnamic acid (10 mg/μL in 70% acetonitrile, 30% H2O and 1% trifluoroacetic acid) using the HTX TM-Sprayer (HTX Technologies, Chapel Hill, North Carolina, USA) with the following parameters: temperature 75°C; number of passes 4; flow rate 0.12 mL/min; speed 1200 mm/min; lane spacing 2 mm; pressure 10 psi.

MALDI-MSI analysis

Mass spectra were acquired in reflectron positive mode within the *m*/*z* 700-3000 range using a rapifleX MALDI Tissuetyper (Bruker Daltonics, Bremen, Germany). MALDI-MS Images were acquired with a beam scan setting of 6 μm and a raster scan of 10 μm in the x-dimension and y-dimension. A mixture of standard peptides in the mass range of *m*/*z* 750–3150 (PepMix I,

Bruker Daltonics) was used for external calibration directly on the glass slide. FlexControl 4.0 (Bruker Daltonics) was used to set up instrument parameters and FlexImaging 5.0 (Bruker Daltonics) was used to set up imaging parameters. After the MSI analysis, the matrix was removed with 1-minute washes in decreasing concentrations of ethanol (100%, 90%, 70%) and slides were stained with Congo red. Finally, slides were converted to digital format using a digital scanner MIDI II (3DHISTECH, Budapest, Hungary), which allowed integration of molecular and optical imaging data. The whole-slide images were then evaluated by experienced nephropathologists (VL'I and FP) to determine regions of interest (ROIs) based on areas of bright Congo red in amyloidosis cases. In negative controls (IgA nephropathy) and LCDD cases, whole glomeruli were labelled due of the general absence of amyloid deposits.

Statistical analysis

The data files containing individual spectra from each entire measurement region were imported into SCiLS Lab 2023a Pro software (http://scils.de/; Bruker Daltonics, Bremen, Germany) to perform data preprocessing, consisting in baseline subtraction (TopHat algorithm), normalisation (Total Ion Count algorithm) and spatial denoising. ROIs previously labelled by the pathologist were then defined using the same software. Feature selection, that considered the signal-to-noise ratio, peak shape, and the frequency of the spectra in which it appeared, was performed to eliminate chemical noise and generate an *m*/*z* feature list specific to this kidney tissue and the pathologist's annotations. Subsequently, amyloid *fingerprint* proteins (apolipoprotein E, ApoE; apolipoprotein A1, ApoA1; apolipoprotein A4, ApoA4; serum amyloid P-component, SAP; vitronectin, VTNC)[176] and amyloid precursor proteins (serum amyloid A-component, SAA; immunoglobulin λ light chain, IGLV; immunoglobulin κ light chain, IGKV)

were subjected to *in silico* digestion through the open source software https://web.expasy.org/peptide_mass/ to obtain the *m*/*z* values of possible tryptic peptides derived from the above proteins. Briefly, trypsin was selected as a digestion enzyme allowing for 0 missed cleavages, including the possibility of methionine oxidation, and displaying results in the form $[M+H]^+$, including all possible post-translational modifications. The *m*/*z* values obtained from *in silico* digestion were then compared with the *m*/*z* feature list obtained from the mean spectrum of the analysed biopsies: theoretical *m*/*z* values whose mass error was above 150 ppm, which was determined based on the mass accuracy of the mass spectrometer used in this study, were removed from the list. To further confirm the reliable correlation between the *m*/*z* values and the proteins of interest, only peaks whose distribution correlated with regions of suspected amyloidosis manually annotated by a pathologist (Pearson Correlation Coefficient ≥ 0.25) were included in the final curated list of *m*/*z* values of putative tryptic peptides. The complete panel of tryptic fragments obtained after the filtering procedure is listed in **Table 1**. To detect regions of putative amyloid deposition in each individual biopsy, the single measurement regions obtained from each biopsy were subjected to spatial segmentation with the panel of *fingerprint* tryptic fragments, utilising the bisecting k-means algorithm with very strong denoising to account for the intervariability of adjacent pixels. To assess the specificity of amyloid *fingerprint* proteins within deposits, receiver operating characteristic (ROC) analysis was performed, requiring an area under the curve (AUC) of ≥ 0.70 and a *p value* ≤ 0.05 (calculated using the Wilcoxon rank sum test) for a peak to be considered statistically significant. In addition, the maximum intensities of features of interest were exported to excel, where the mean of the maximum peak intensities was calculated for each tryptic fragment of the same protein, to account for the different ionisation abilities of the tryptic peptides. The obtained intensities imported into

MetaboAnalyst 5.0, an open-source software for the statistical analysis of omic data, and normalised with log transformation to obtain a Hierarchical Clustering Heatmap using the Euclidean distance measure and Ward clustering method as parameters. Finally, data was imported in GraphPad Prism 5 (GraphPad Software Inc., California, USA) to generate a bar chart of the intensities of target proteins in different sample types.

Amyloid *fingerprint* proteins	**Abbreviation**	***m/z***	**Error (ppm)**
Apolipoprotein E	ApoE	948.50	27
		968.50	7
		1497.80	54
Apolipoprotein A1	ApoA1	831.40	43
		1031.50	145
Apolipoprotein A4	ApoA4	983.43	124
Serum amyloid P	SAP	764.37	98
Vitronectin	VTNC	1503.80	27
		1666.83	30
Amyloid precursor proteins	**Abbreviation**	***m/z***	**Error (ppm)**
742.39 96	SAA	742.39	96
		1457.07	38
		1550.58	52
Immunoglobulin kappa variable 1–17	IGKV117	1434.12	38
Immunoglobulin kappa variable 2–29	IGKV229	1158.58	9
Immunoglobulin lambda variable 2–11	IGLV211	883.47	5
Immunoglobulin lambda variable 3–25	IGLV325	1242.69	64

Table 1. The filtered list of amyloid *fingerprint* and precursor proteins. Only *m/z* values with a mass error ≤ 150 ppm and a PCC ≥ 0.25 in respect the pathologist's annotations were included in the panel.

Results

Clinical and histological characteristics of the cohort

The clinical, laboratory and histological characteristics of the patients included in the study are shown in **Table T2**. 63% of patients were male, patients' mean age was 56.2 (±19.2) years, mean serum creatinine was 1.3 (±1.6 mg/dL) and mean proteinuria was 4.4 (±3.6 g/24 hours) at the time of diagnosis. All six cases diagnosed with AL amyloidosis and two LCDD cases had a circulating M-spike, with IF/IHC showing concordant positivity for the immunoglobulin light chain involved. In contrast, in the minimal amyloidosis cases, IF/IHC failed to type the deposits, with only case #13 showing an elevated circulating free λ light chain and case #12 showing no detectable M-spike at the time of diagnosis. All three cases of AA-amyloidosis were strongly and diffusely positive for the protein SAA and negative for κ and λ light chains with IF/IHC. Two of these cases were affected by rheumatoid arthritis and one by Crohn's disease. On histopathological examination, the mean number of glomeruli in the renal biopsy was 15.4 (± 8.0), with an overall mild chronicity score composed of 18.4% GS glomeruli and 18.4% IFTA. The overall mean AS calculated in amyloidosis cases was 1.2 (±0.8), with a predominance of the glomerular compartment (mesangial score 1.5±1.2, capillary score 1.7±1.0) compared with the vascular (1.4±1.1) and interstitial (0.3±0.6) compartments.

Case ID (#)	Sex	Age (y)	Serum creatinine (mg/dl)	Proteinuria (g/die)	M-spike	N° glomeruli	CSIS		AS					Final diagnosis	IHC/IF typing
							GS (%)	IFTA (%)	M	Cap	Vasc	Int	Total		
1	F	80	4.60	1.8	-	31	58	60	3	3	1	0	1.75	Amyloidosis	SAA
2	F	64	0.80	6.3	-	5	0	5	1	1	1	0	0.75	Amyloidosis	SAA
3	M	30	1.43	3.8	-	14	14	20	3	3	2	0	2	Amyloidosis	SAA
4	F	74	0.64	3.5	IgG λ	27	15	5	1	1	2	0	1	Amyloidosis	λ
5	F	50	3.60	5.8	FLC λ	12	0	30	3	3	2	1	2.25	Amyloidosis	λ
6	F	70	0.90	8.0	FLC λ	7	0	0	1	1	0	0	0.5	Amyloidosis	λ
7	M	83	5.00	1.0	IgM κ	13	38	40	1	1	3	0	1.25	Amyloidosis	κ
8	M	26	2.00	11.0	IgG κ	15	0	5	1	1	1	0	0.75	Amyloidosis	κ
9	M	71	1.90	0.6	IgA κ	28	61	50	3	3	3	2	2.75	Amyloidosis	κ
10	M	44	2.00	1.6	FLC λ	20	20	40	-	-	-	-	-	LCDD	λ
11	M	60	1.50	3.0	FLC λ	12	33	20	-	-	-	-	-	LCDD	λ
12	F	57	0.80	6.8	-	11	0	5	0	1	0	0	0.25	Amyloidosis (minimal)	NA
13	M	62	0.87	3.0	FLC λ	10	0	0	0	1	0	0	0.25	Amyloidosis (minimal)	NA
14	M	54	1.36	1.9	-	9	33	10	-	-	-	-	-	IgA nephropathy	-
15	M	58	1.32	3.0	-	9	22	5	-	-	-	-	-	IgA nephropathy	-
16	M	16	1.00	2.0	-	23	0	0	-	-	-	-	-	IgA nephropathy	-

Table 2. Clinical, laboratory and histological characteristics of samples. F, female; M, male; CSIS, composite scarring injury score; GS, global glomerulosclerosis; IFTA, interstitial fibrosis and tubular atrophy; AS, amyloid score; M, mesangial; Cap, capillary; Vasc, vascular; Int, interstitial; IHC, immunohistochemistry; IF, immunofluorescence; SAA, serum amyloid A protein; NA, not assessed.

Detection of fingerprint proteins in amyloid deposits with MALDI-MSI

The MALDI-MSI analysis performed on nine fully typed amyloidosis cases (#1–#9) and on three amyloid-negative controls (IgA nephropathy, #14–#16) revealed a higher abundance of amyloid *fingerprint* proteins in the latter group regardless of amyloid subtype, as shown in **Figure 1**.

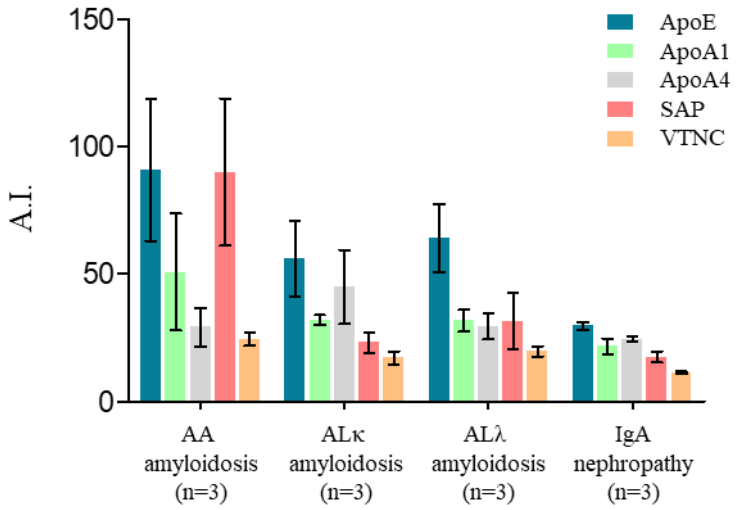

Figure 1. Averaged maximum intensities of ApoE, SAP, ApoA1, ApoA4 and VTNC in AA amyloidosis, ALκ amyloidosis, ALλ amyloidosis and IgA nephropathy cases. All amyloidosis cases showed an increased maximum intensity of amyloid fingerprint proteins compared with controls (ALκ: n=3, spectra=10 731; ALλ: n=3; spectra=19 026; AA: n=3, spectra=19 162 vs IgA: n=3, spectra=10 588). AI, arbitrary intensity.

Based on this premise, a fold change (FC) analysis was performed to quantify the increase of fingerprint proteins in amyloidosis with respect to the negative controls and evaluate which *fingerprint* proteins may play a predominant role in distinguishing amyloidosis from controls, highlighting ApoE, SAP, and ApoA1 as those with a higher FC (**Table 3**). Subsequently, a ROC analysis was performed to compare the presence of each *fingerprint* protein in ROIs annotated by the pathologist compared to the remaining bioptic tissue, representing areas without amyloidosis, to assess the contribution of each amyloid associated protein in the distinction of amyloid deposits versus the non-amyloidotic regions. **Table 4** reports the mean

intensities of *fingerprint* proteins and the AUC value obtained by confronting the intensities inside and outside putative amyloid deposits, further demonstrating the ability of ApoE, SAP, and ApoA1 to differentiate amyloid plaques from the background with an AUC > 0.70 (in green). Whilst showing less robust results, ApoA4 and VTNC could still produce an AUC > 0.70 for ALκ and AA amyloidosis cases, respectively.

Precursor protein	Mean intensity in amyloidosis cases (n=9)	Mean intensity in IgA cases (n=3)	Fold change
ApoE	125.40	27.01	4.6
SAP	63.36	21.68	2.9
ApoA1	51.32	27.64	1.9
ApoA4	42.60	26.82	1.6
VTNC	22.96	13.23	1.7

Table 3. Fold changes calculated by dividing the mean maximum intensity of the peaks of amyloid-associated proteins in all amyloidosis cases and the mean maximum intensity of these peaks in the controls.

	AA-amyloidosis (n=3)		ALκ amyloidosis (n=3)		ALλ amyloidosis (n=3)	
Protein	Amyloid/ Non-amyloid areas	AUC	Amyloid/ Non-amyloid areas	AUC	Amyloid/ Non-amyloid areas	AUC
ApoE	3.12/2.05	0.92	3.89/2.87	0.74	13.96/6.12	0.89
SAP	5.68/2.73	0.81	4.57/2.49	0.88	7.64/5.26	0.76
ApoA1	7.33/3.25	0.76	3.81/2.86	0.74	6.38/5.19	0.62
ApoA4	5.69/3.32	0.64	8.90/3.42	0.96	5.40/6.10	0.43
VTNC	1.34/0.96	0.76	1.66/1.66	0.51	2.34/2.17	0.55

Table 4. Average intensities of amyloid *fingerprint* proteins and AUC values obtained by comparing intensities inside and outside putative amyloid deposits. AUC values > 0.70 are shown in green.

Segmentation of amyloid deposits using amyloid fingerprint proteins

Based on the previous results, image segmentation was performed using the complete panel of *m*/*z* derived from *fingerprint* proteins reported in **Table 1** to obtain automatic annotations of putative amyloid deposition. Visually, the identified putative deposits displayed a good degree of colocalisation with the annotations highlighted by the nephropathologists on the Congo red stained section (**Figure 2, a–e**). When looking closely at manually annotated regions (pathologist) compared to the automatically annotated regions (MALDI-MSI), the latter could highlight larger areas of putative amyloid deposition, corresponding to glomerular, tubulointerstitial, and perivascular compartments (**Figure 2, f**). Representative MALDI-MS images of *fingerprint* proteins are displayed in **Figure 2, g**. All *fingerprint* proteins were shown to colocalise with automatic annotations and, as reported in the previous paragraph, ApoE, ApoA1, and SAP displayed a higher intensity in the automatically segmented areas compared to ApoA4 and VTNC.

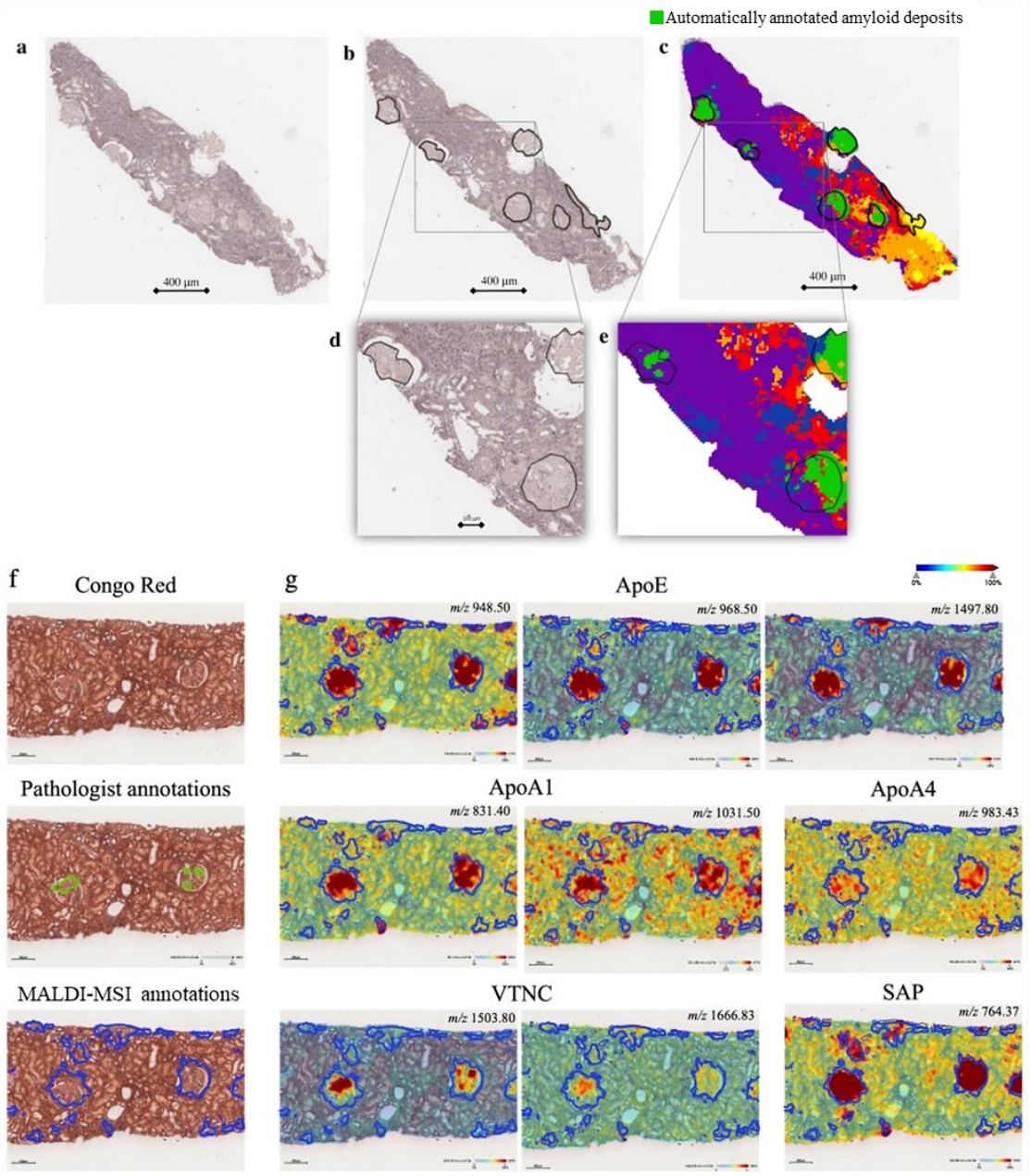

Figure 2 a) Kidney biopsy stained with Congo red. **b)** Pathologist's manual annotations on Congo red stained image (black). **c)** Results of spatial segmentation based on the distribution of amyloid *fingerprint* proteins. **d)** Detail of manual annotations. **e)** Detail of spatial segmentation. **f)** Congo red shows the difference between pathologist's manual annotations (green) and automatic annotations by spatial segmentation (blue). **g)** Distribution of amyloid *fingerprint* proteins; molecular images are overlaid with histological images to highlight colocalisation of signals and morphological structures. All signals from amyloid *fingerprint* proteins show strong colocalisation with automatically annotated regions (in blue). ApoE, apolipoprotein E; ApoA1, apolipoprotein A1; ApoA4, apolipoprotein A4; MSI, mass spectrometry imaging; SAP, serum amyloid P; VTNC, vitronectin.

Detection of amyloid precursor proteins for amyloid typing

The averaged maximum intensities of amyloid precursor proteins (SAA, immunoglobuling λ, and κ light chains) was assessed in automatically detected amyloid deposits highlighted by the spatial segmentation to perform amyloid typing (**Figure 3, a**). The abundance of each protein was in agreement with results of IF/IHC typing, with a specific enrichment of SAA in AA-amyloidosis, of IGKV in ALκ-amyloidosis, and of IGLV in ALλ-amyloidosis. The enrichment of each *m*/*z* signal included in the target panel is shown in **Figure 3, b**. Only the tryptic fragment *m*/*z* 1242.69 of IGLV displayed an aspecific enrichment in ALκ-amyloidosis but still demonstrated a higher abundance in ALλ-amyloidosis. Lastly, **Figure 3, c** displays representative MALDI-MSI images of cases of ALλ-amyloidosis, ALκ-amyloidosis, and AA-amyloidosis. When looking at the distribution of SAA, IGKV, and IGLV, a specific enrichment of each amyloid precursor protein in automatically annotated deposits (black line), according to IF/IHC typing, can be assessed.

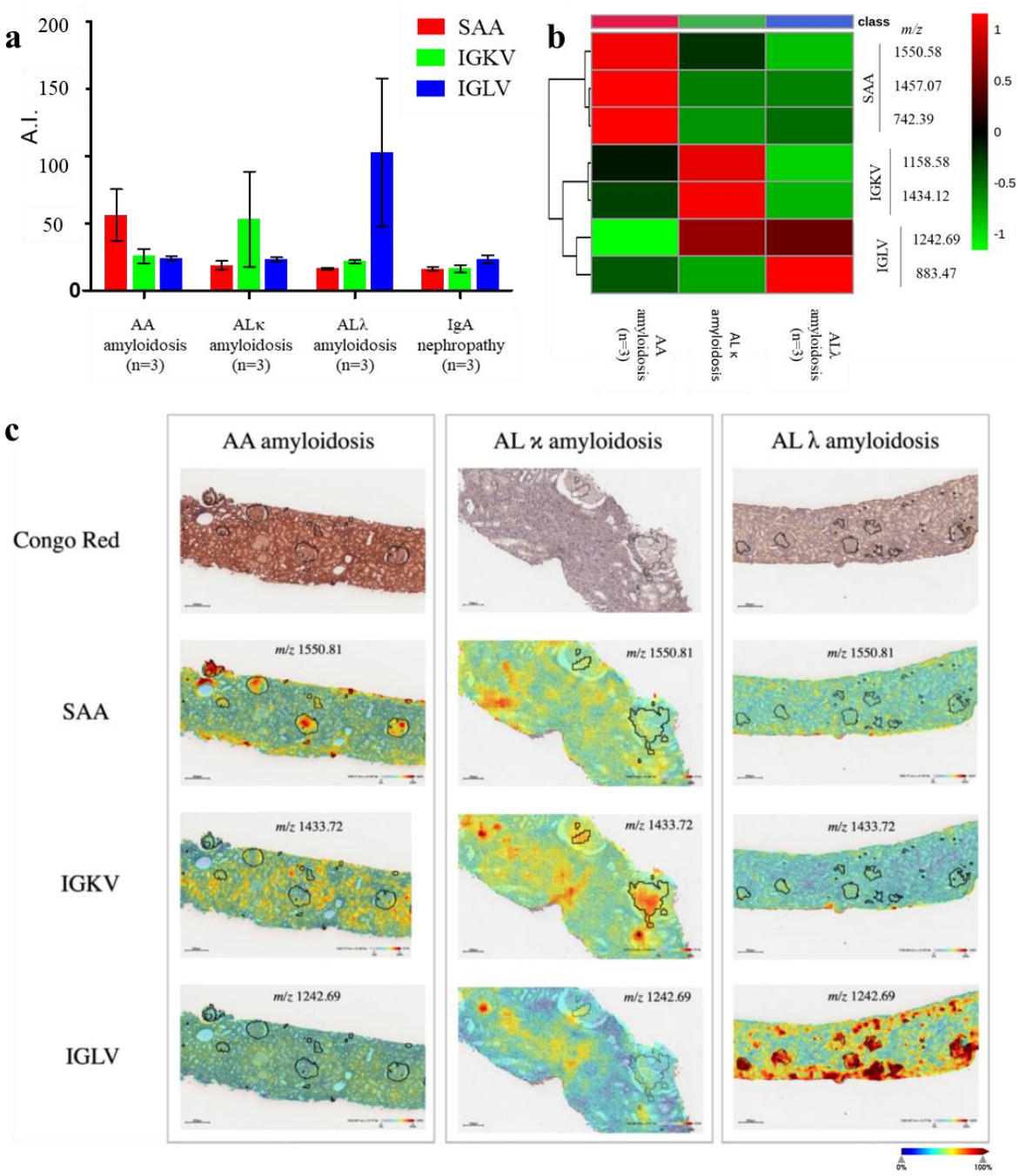

Figure 3 a) Averaged maximum intensities of amyloid precursor proteins in amyloidosis cases. SAA, IGKV, and IGLV show a specific enrichment in AA, ALκ, and ALλ-amyloidosis, respectively. **b)** Heatmap showing the correlation between amyloid precursor proteins (SAA, IGKV, IGLV) and amyloidosis classes (AA, ALκ, ALλ). **c)** Distribution of amyloid precursor proteins in renal amyloidosis cases; molecular images are overlaid with histological images to highlight colocalisation of signals and morphological structures. All precursor proteins show specificity for the respective amyloidosis type, with increased abundance in automatically annotated deposits (black line).

Proof of concept with challenging cases of minimal amyloidosis

Finally, more challenging cases were subjected to investigation with MALDI-MSI to assess the reliability of the proposed workflow for amyloid detection and typing. Specifically, two cases of LCDD (LCDD #10 and LCDD #11) and two cases of minimal amyloidosis (MA #12 and MA #13) were considered. As a first assessment, the intensity of amyloid *fingerprint* proteins was evaluated within automatically annotated deposits of MA and within the glomeruli of LCDD cases, considering that these structures represent the primary sites of amyloid deposition, and compared to the intensity of the same proteins against the rest of the tissue. Even in this instance, as previously reported in paragraph *Detection of fingerprint proteins in amyloid deposits with MALDI-MSI*, the *fingerprint* proteins SAP, ApoE, and ApoA1 demonstrated a higher AUC value compared to ApoA4 and VTNC in minimal amyloidosis cases, albeit below the threshold of 0.70 (**Table 5**). All *fingerprint* proteins demonstrated a complete lack of enrichment (AUC ~ 0.50) in the glomeruli of LCDD cases. Based on these promising findings, the distribution of the restricted *fingerprint* panel (*i.e.* SAP, ApoE, ApoA1) was evaluated in MA and LCDD (**Figure 5**), demonstrating a colocalisation of *fingerprint* proteins with putative deposits in MA, and a diffused distribution in LCDD cases.

	Minimal amyloidosis (MA)		Light Chain Deposition Disease (LCDD)	
Protein	Amyloid/ Non-amyloid areas	AUC	Amyloid/ Non-amyloid areas	AUC
ApoE	1.43/1.41	0.57	1.44/1.49	0.51
SAP	1.74/1.65	0.61	1.50/1.62	0.49
ApoA1	1.51/1.46	0.67	1.49/1.61	0.50
ApoA4	1.61/1.61	0.50	1.50/1.60	0.45
VTNC	0.86/0.89	0.44	0.84/0.85	0.50

Table 5. Average intensities of amyloid *fingerprint* proteins and AUC values obtained by comparing intensities inside and outside putative amyloid deposits (MA) or inside and outside glomeruli (LCDD).

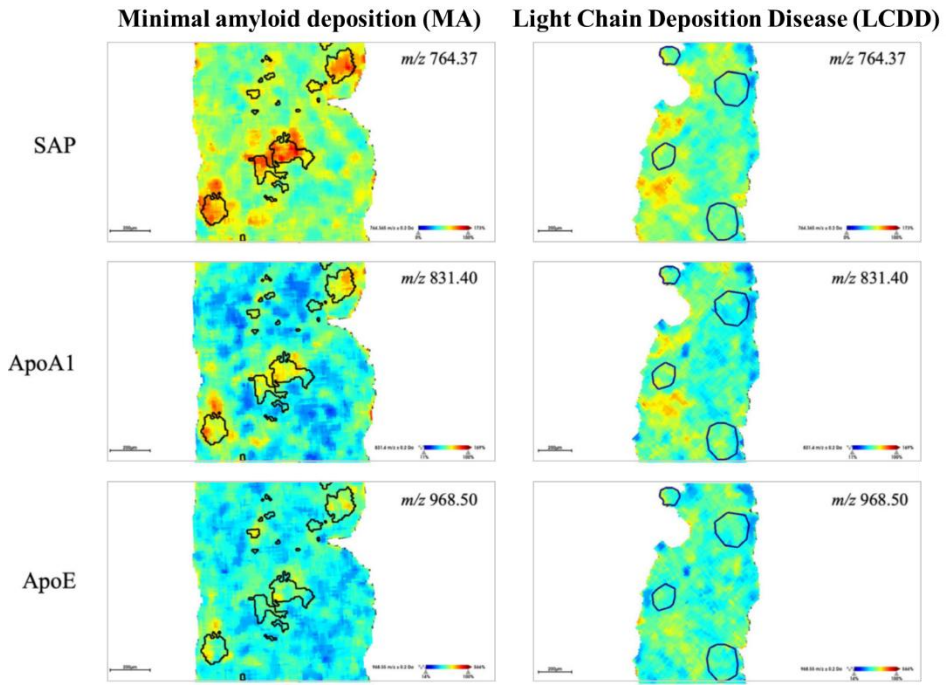

Figure 5. Distribution of SAP (*m/z* 764.37), ApoA1 (*m/z* 831.40) and ApoE (*m/z* 968.50) on tissue in one case of MA deposition and in one case of LCDD. The proteins show a light degree of colocalisation with automatically detected regions of interest in MA but have a diffuse distribution in LCDD.

In light of these indications in MA cases, the presence of the responsible precursor proteins was also investigated in the cohort of challenging cases. Interestingly, MALDI-MSI was able to indicate a higher abundance of λ light chain in both #12 and #13 MA cases (**Figure 6**). Whilst case #13 presented a FLC λ M-spike at the time of biopsy, case #12 did not demonstrate an M-spike at diagnosis and was negative for IF/IHC. Interestingly, MALDI-MSI showed a higher intensity of λ light chain protein within putatively annotated amyloid deposits, indicating AL λ amyloidosis as a possible classification, and this was later confirmed by the discovery of a λ M-spike during patient follow-up.

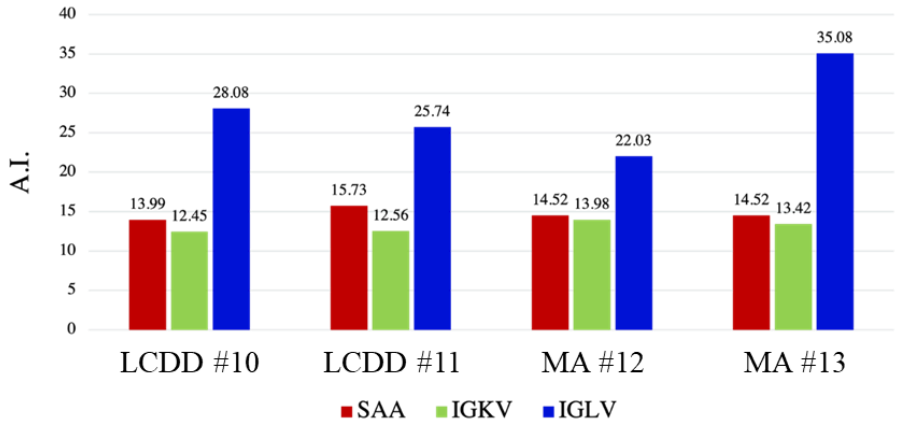

Figure 6. Averaged maximum intensities of amyloid precursor proteins in Light Chain Deposition Disease (LCDD #10, LCDD #11) and Minimal Amyloidosis (MA #12, MA #13) cases. For all considered cases there seems to be an enrichment of λ light chain signals compared to other precursor proteins, concordantly with the M-spike detected at the time of diagnosis or after patient follow up.

Discussion

MGRS comprises a complex group of renal diseases caused by direct or indirect damage due to a circulating monoclonal protein[17]. Considering their poor outcome[18,19], a rapid and accurate recognition of the disease is of paramount importance to initiate the most appropriate treatment, generally based on aggressive clone-directed therapeutic approaches, even in the absence of detectable hematological neoplasm[29]. One of the most common forms of MGRS is amyloidosis, a disease characterised by the progressive accumulation of fibrillar misfolded proteins that can be detected by Congo red staining and typed using IF/IHC[3]. Although these approaches have proven useful for the immediate detection of AL amyloidosis, recent advances in analytical technologies have shown that IF/IHC is still insufficient to type the full spectrum of MGRS cases, with rarer forms of amyloidosis still being misdiagnosis due to this lack of sensitivity[4]. With this in mind, the recent introduction of MS techniques has already proven to be a promising approach for amyloid typing. In particular, MS enabled the enrichment of the list of known amyloid precursor proteins[6] and the identification of a panel of recurrent proteins that may represent the sentinel of amyloid deposition, named *fingerprint* proteins. Recently, the introduction of *in situ* proteomics (MALDI-MSI) has given further impetus to this field and prompted the exploration of a fully automated proteomics-based tool that can aid the nephropathologist in the single-slide detection and typing of amyloidosis. One of the perks of these innovative *in situ* techniques is the possibility to perform the analysis on the same FFPE section used for the diagnosis, without tissue destruction through manual or laser microdissection, performing the analysis on a tissue section which still remains available for the pathologist's evaluation, as in this study. Moreover, laser microdissection relies on Congo Red staining,

which can be compromised by heterogeneities in staining, section thickness, low abundance of deposits, and tissue autofluorescence[21,22]. MSI-based approaches do not suffer from these variables and still provide great specificity, as evidenced in this work by the detection of tiny interstitial deposits, potentially overlooked on the original biopsy.

In the present study, the initial aim consisted in defining an automated segmentation pipeline based on amyloid *fingerprint* proteins, which was successfully carried out enabling the computational-aided identification or areas of putative amyloid deposition. Moreover, this study led to further restriction to the three most commonly found proteins, namely ApoE (*m*/*z* 948.50, *m*/*z* 968.50, *m*/*z* 1497.80), ApoA1 (*m*/*z* 831.40, *m*/*z* 1031.50) and SAP (*m*/*z* 764.37), able to improve the potential for segmentation of amyloid deposits. Along these lines, previous studies already proved that some of the *fingerprint* proteins (*e.g.*, VTNC and ApoA4) are differentially represented in different types of amyloidosis, limiting their use as sentinels for amyloid deposition in all cases[23]. This is particularly relevant in cases characterised by minimal amyloid deposits that are barely visible through light microscopy, where tissue is insufficient to be typed with IF/HC, and where there is eventual need of TEM for fibril detection, which is laborious and requires dedicated tissue sections. This work also enabled the typing of 9 amyloidosis cases diagnosed with SAA, ALκ, and ALλ amyloidosis, which represent the most common forms of the disease, in agreement with IF/IHC, which represents the most commonly utilised diagnostic approach. In addition, the workflow was applied to more challenging cases, leading to the detection of concordant light chains in cases of LCDD, without concomitant deposition of *fingerprint* proteins, and the detection of λ light chains in cases of non-fully-typed minimal amyloidosis. Interestingly, in one case presenting minimal amyloid deposition, this approach enabled the detection of a higher abundance of λ light chains even

before an M-spike could be assessed after patient follow-up, further hinting at the specificity of the technique and the reliability of the approach in early amyloid detection and typing.

Notwithstanding the promising results of this pilot study, further confirmations of these initial findings are required, especially considering the relatively small sample cohort that was used. In addition, the potential application of machine learning algorithms to complement MALDI-MSI could be explored in order to further enhance the proposed approach and promote its integration it into the clinical setting in a streamlined manner.

Conclusions

In this pilot study, MALDI Mass Spectrometry Imaging was applied to a small cohort of renal amyloidosis biopsies to assess its feasibility for the automatic detection of putative amyloid plaques and for their subsequent typing. Moreover, the potential of MALDI-MSI to detect amyloid precursor proteins when their abundance is minimal was assessed by implementing the technique on cases whose diagnosis and classification was considered challenging. The results presented in this study hint at the possibility to implement MALDI-MSI for the computationally enabled diagnosis of amyloidosis in a Congo Red-independent way, proposing it as a sensitive, automatable tool for the detection and subtyping of renal amyloidosis in FFPE tissue.

References

1. Leung, N., Nasr, S. H. & Sethi, S. How I Treat amyloidosis: The importance of accurate diagnosis and amyloid typing. *Blood* **120**, 3206–3213 (2012).
2. L'Imperio, V. *et al.* Monoclonal Gammopathy of Renal Significance: A Molecular Middle Earth between Oncology, Nephrology, and Pathology. *Kidney Diseases* vol. 8 446–457 Preprint at https://doi.org/10.1159/000527056 (2022).
3. Fogo, A. B., Lusco, M. A., Najafian, B. & Alpers, C. E. AJKD atlas of renal pathology: AL amyloidosis. *American Journal of Kidney Diseases* **66**, e43–e45 (2015).
4. Gonzalez Suarez, M. L. *et al.* The sensitivity and specificity of the routine kidney biopsy immunofluorescence panel are inferior to diagnosing renal immunoglobulin-derived amyloidosis by mass spectrometry. *Kidney Int* **96**, 1005–1009 (2019).
5. Dasari, S. *et al.* Amyloid Typing by Mass Spectrometry in Clinical Practice: a Comprehensive Review of 16,175 Samples. *Mayo Clin Proc* **95**, 1852–1864 (2020).
6. Benson, M. D. *et al.* Amyloid nomenclature 2020: update and recommendations by the International Society of Amyloidosis (ISA) nomenclature committee. *Amyloid* **27**, 217–222 (2020).
7. Vrana, J. A. *et al.* Clinical diagnosis and typing of systemic amyloidosis in subcutaneous fat aspirates by mass spectrometry-based proteomics. *Haematologica* **99**, 1239–1247 (2014).
8. L'Imperio, V. *et al.* Spatial transcriptome of a germinal center plasmablastic burst hints at MYD88/CD79B mutants-enriched diffuse large B-cell lymphomas. *Eur J Immunol* **52**, 1350–1361 (2022).
9. Smith, A. *et al.* High Spatial Resolution MALDI-MS Imaging in the Study of Membranous Nephropathy. *Proteomics Clin Appl* **13**, (2019).
10. Winter, M., Tholey, A., Kristen, A. & Röcken, C. MALDI Mass Spectrometry Imaging: A Novel Tool for the Identification and Classification of Amyloidosis. *Proteomics* **17**, (2017).
11. L'Imperio, V. *et al.* Histoproteomic characterization of localized cutaneous amyloidosis in X-linked reticulate pigmentary disorder. *Skin Pharmacology and Physiology* vol. 30 90–93 Preprint at https://doi.org/10.1159/000464336 (2017).
12. Casadonte, R. *et al.* Imaging mass spectrometry analysis of renal amyloidosis biopsies reveals protein co-localization with amyloid deposits. *Anal Bioanal Chem* **407**, 5323–5331 (2015).
13. L'Imperio, V. *et al.* Digital pathology for the routine diagnosis of renal diseases: a standard model. *J Nephrol* **34**, 681–688 (2021).
14. Hoelbeek, J. J., Kers, J., Steenbergen, E. J., Roelofs, J. J. T. H. & Florquin, S. Renal amyloidosis: Validation of a proposed histological scoring system in an independent cohort. *Clin Kidney J* **14**, 855–862 (2021).
15. Rubinstein, S. *et al.* Novel pathologic scoring tools predict end-stage kidney disease in light chain (AL) amyloidosis. *Amyloid* **24**, 205–211 (2017).
16. De Sio, G. *et al.* A MALDI-Mass Spectrometry Imaging method applicable to different formalin-fixed paraffin-embedded human tissues. *Mol Biosyst* **11**, 1507–1514 (2015).
17. Leung, N., Bridoux, F. & Nasr, S. H. Monoclonal Gammopathy of Renal Significance. *New England Journal of Medicine* **384**, 1931–1941 (2021).
18. Kyle, R. A. *et al.* Monoclonal gammopathy of undetermined significance (MGUS) and smoldering (asymptomatic) multiple myeloma: IMWG consensus perspectives risk factors for progression and guidelines for monitoring and management. *Leukemia* vol. 24 1121–1127 Preprint at https://doi.org/10.1038/leu.2010.60 (2010).
19. Steiner, N. *et al. Monoclonal Gammopathy of Renal Significance (MGRS) Increases the Risk for Progression to Multiple Myeloma: An Observational Study of 2935 MGUS Patients*. www.impactjournals.com/oncotarget (2017).

20. Fermand, J.-P. *et al.* How I Treat How I treat monoclonal gammopathy of renal significance (MGRS). (2013) doi:10.1182/blood-2013-05.\
21. Gupta, N., Kaur, H. & Wajid, S. Renal amyloidosis: an update on diagnosis and pathogenesis. doi:10.1007/s00709-020-01513-0/Published.
22. Wisniowski, B. & Wechalekar, A. Confirming the diagnosis of amyloidosis. *Acta Haematologica* vol. 143 312–321 Preprint at https://doi.org/10.1159/000508022 (2020).
23. Mollee, P. *et al.* Implementation and evaluation of amyloidosis subtyping by laser-capture microdissection and tandem mass spectrometry. *Clin Proteomics* **13**, 1–6 (2016).

2.3 The feasibility of MALDI-MSI based proteomics using bouin-fixed pathology samples: expanding access to nephropathology archives

Adapted from:

Bindi, G.[1], Pagani, L.[1], Ceku, J.[2], de Oliveira, G. S.[1], Porto, N. S.[1], Monza, N.[1], Denti, V.[1], Mescia, F.[3,4], Chinello, C.[1], Fraggetta, F.[5], Magni, F.[1], Pagni, F.[2], Alberici, F.[3,4], L'Imperio, V.[2], & Smith, A[1]. (**2024**).

Feasibility of MALDI-MSI-Based Proteomics Using Bouin-Fixed Pathology Samples: Untapping the Goldmine of Nephropathology Archives.

Journal of proteome research, 23(7), 2542–2551.

https://doi.org/10.1021/acs.jproteome.4c00198

[1] Department of Medicine and Surgery, Proteomics and Metabolomics Unit, University of Milano-Bicocca, Vedano al Lambro, 20854, MB, Italy

[2] Department of Medicine and Surgery, Pathology, IRCCS Fondazione San Gerardo dei Tintori, University of Milano-Bicocca, Monza, 20900, MB, Italy

[3] Nephrology Unit, Spedali Civili Hospital, ASST Spedali Civili di Brescia, Brescia, 25123, BS, Italy

[4] Department of Medical and Surgical Specialties, Radiological Sciences and Public Health, University of Brescia, Brescia, 25123, BS, Italy

[5] Pathology Unit, Gravina Hospital Caltagirone, ASP Catania, Caltagirone, 95041, CT, Italy.

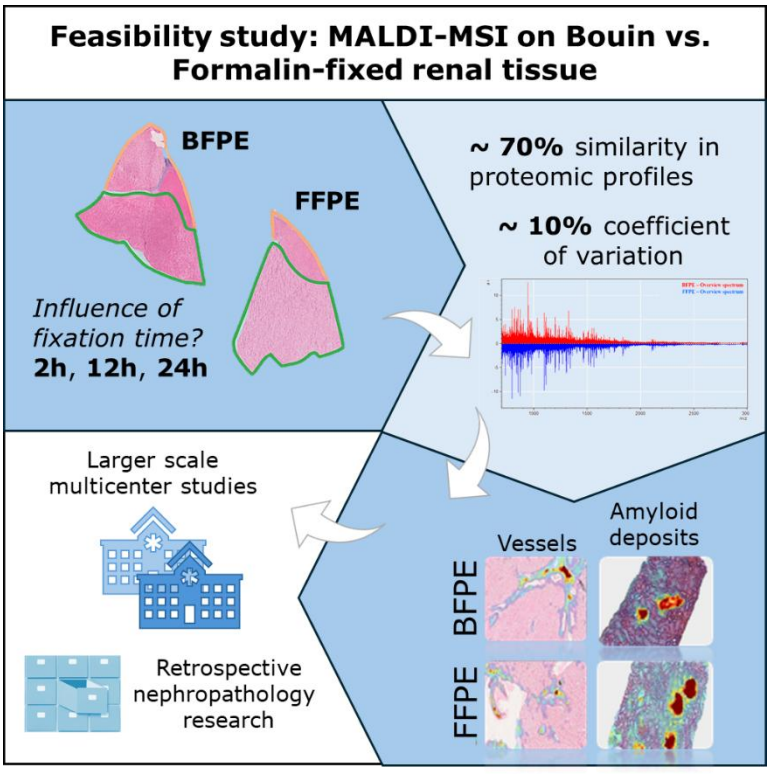

Abstract

The application of innovative spatial proteomics techniques, such as those based upon Matrix-Assisted Laser Desorption/Ionisation Mass Spectrometry Imaging (MALDI-MSI), has the potential to impact research in the field of nephropathology. Notwithstanding, the possibility to apply this technology in more routine diagnostic contexts remains limited by the alternative fixatives employed by this specific diagnostic field, where numerous nephropathology laboratories worldwide utilise Bouin-Fixed Paraffin-Embedded (BFPE) samples. Here, the feasibility of performing MALDI-MSI on BFPE renal tissue is explored, evaluating variability within the trypsin-digested proteome as a result of different preanalytical conditions and comparing them with the more standardised Formalin-Fixed Paraffin-Embedded (FFPE) counterparts. Upon data analysis, a vast majority of molecular features (n = 270, 68.9%) could be concurrently detected in BFPE and FFPE renal samples, and both fixatives demonstrated a limited variability in signal intensity (coefficient of variation of 10.22–10.06%, respectively) among technical replicates. Samples processed with either fixative were able to discriminate the principal parenchyma regions along with diverse renal substructures, such as glomeruli, tubules, and vessels. Additionally, a proof-of-concept study was performed to assess the possibility to detect amyloid deposits on tissue with BFPE samples, showing comparable results with FFPE samples in terms of the distribution of several amyloid *fingerprint* proteins. These results suggest the utility of BFPE tissue specimens in MSI-based nephropathology research, further widening their application in the field.

Introduction

The introduction of mass spectrometry-based proteomics is gradually impacting various fields of medicine[1], particularly molecular pathology. Of note, the advent of spatial proteomics techniques, such as Matrix-Assisted Laser Desorption/Ionisation Mass Spectrometry Imaging (MALDI-MSI), has also permitted *in situ* molecular mapping of pathological tissue to be integrated with routine histomorphological evaluation, further broadening its application in this field[2]. Whilst the most ideal samples for this application are represented by fresh or snap-frozen tissues, which maintain a more native molecular representation of the cells present within the tissue along with improved antigenicity, it can be challenging to achieve a widespread application of this technique without using fixed samples derived from pathology archives. For this reason, standardised protocols which enable MALDI-MSI proteomics analysis of archived formalin-fixed paraffin-embedded (FFPE) tissues have been developed, presenting comparable results with respect to their fresh or snap-frozen counterparts[3], and have since been applied to a variety of disease contexts, including renal diseases[4–6]. These approaches have also been facilitated by the introduction of instruments which permit imaging at higher lateral resolutions, down to the level of a single-cell[7].

Notwithstanding this progress, the possibility to apply MALDI-MSI technology in routine diagnostic is still limited by the alternative fixatives employed by highly specialised diagnostic fields, including nephropathology, where several laboratories worldwide utilise bouin-fixed paraffin embedded (BFPE) samples[8]. Frequently, BFPE is preferred due to its ability to preserve the morphological details of the renal structures, albeit at the expense of antigenicity preservation[9]. However, this fixative may also have an impact on the proteomic yield following the *in situ* enzymatic digestion required for the

MALDI-MSI proteomic analysis of tissue. For this reason, dedicated efforts are required to assess the possibility to perform MALDI-MSI analysis on BFPE tissue samples, whilst evaluating the differences in respect to FFPE samples, to expand access to nephropathology archives.

In the presented work, the feasibility of performing proteomics MALDI-MSI on BFPE renal tissue is investigated, both on wedge (WB) and core-needle biopsy (CNB)-like samples, evaluating the similarity of the obtained proteomic profiles and tissue distributions with respect to those derived from equivalent FFPE specimens. Moreover, as a proof-of-concept, the feasibility of using BFPE samples is validated through the detection of amyloid *fingerprint* proteins as a use case.

Materials and Methods

Cases

Normal renal tissue was obtained from two different nephrectomy surgical samples (left-over material, cortex away from tumor). Ex-vivo specimens were cut in the form of wedge (WB) or core needle biopsies (CNB) from the two renal samples (first and second replicates) and were alternatively FFPE or BFPE at different fixation times, with a minimum fixation time of 2h for CNBs and 12-24h for both WB and CNBs. WB could not be obtained for FFPE and BFPE samples fixed for 2h, since either fixatives would take more than 2h to fully penetrate tissue; thus, only CNBs are available for 2h fixation time. Blocks were then cut at a thickness of 4 micrometers and sections mounted onto a conductive indium tin oxide (ITO) glass slide and then dried at 60°C for 1 hour to promote tissue adhesion. Additionally, two fully anonymised samples from renal biopsies diagnosed as amyloidosis, either

FFPE and BFPE, were selected to test the comparability in terms of the detection of amyloid *fingerprint* proteins among different pre-analytical/fixative conditions. Approval was obtained from the local ethics committee (GR-2021-12374235, 09/03/23).

Chemicals and reagents

HPLC-grade toluene, HPLC-grade ethanol, HPLC-grade water, LC-MS grade water and HPLC-grade acetonitrile were obtained from Honeywell SC, Seelze, Germany. LC-MS grade acetonitrile was obtained from LiChrosolv®. Trifluoroacetic acid (TFA), citric acid monohydrate, eosin Y solution and ammonium bicarbonate (NH_4HCO_3) were obtained from Sigma-Aldrich, Buchs, Switzerland. Mayer's hematoxylin was purchased from Bio Optica Milano Spa, Milan, Italy. DL-Dithiothreitol (DTT), trypsin from the porcine pancreas and iodoacetamide (IAA) were obtained from Sigma-Aldrich, St. Louis, MO, USA. α-cyano-4-hydroxycinnamic acid matrix and PepMix I were purchased from Bruker Daltonics, Bremen, Germany. RapiGest™ SF was obtained from Waters,Milford (MA), USA. Formic acid (FA) was purchased from LiChropur®, Merck KGaA, Darmstadt, Germany. MMI-L Low Concentration Tuning Mixwas purchased from Agilent Technologies, Santa Clara, CA, USA.

Sample preparation for MALDI-MSI

FFPE and BFPE samples were subjected to deparaffinisation, rehydration, antigen retrieval, and tryptic digestion, according to our previously published method[10]. α-cyano-4-hydroxycinnamic acid matrix (10 mg/μL in 70% acetonitrile and 1% TFA) was sprayed onto the slides using an

HTX TM-Sprayer (HTX Technologies, Chapel Hill, North Carolina, USA) with the following parameters: temperature 75°C; number of passes 4; flow rate 0.12 mL/min; speed 1200 mm/min; pressure 10 psi. A mixture of known masses (PepMix I) was applied directly onto the ITO slide to be used as an external calibrant within the *m*/*z* range 750-3150.

MALDI-MSI analysis

A rapifleX MALDI Tissuetyper (Bruker Daltonics, Bremen, Germany) mass spectrometer was used to acquire mass spectra in reflectron positive ion mode within the *m*/*z* range 700-3000 with a beam scan setting of 46 μm and a raster width of 50 μm in the *x* and *y*-dimensions. The software FlexControl 4.0 (Bruker Daltonics, Bremen, Germany) was used to set instrument parameters, whilst FlexImaging 5.0 (Bruker Daltonics, Bremen, Germany) was used to visualise MALDI-MSI results. After the analysis, slides were washed with increasing concentrations of ethanol (70%, 90% and 100%) and subsequently stained with hematoxylin and eosin (H&E). Then, slides were mounted with a permanent mounting medium and scanned using a digital scanner (NanoZoomer S60, Hamamatsu Photonics).

Sample preparation for nLC-ESI-MS/MS

For protein identification and quantification, a pool of 6 slices of BFPE and FFPE renal samples at different fixation time points (2, 12, 24h), along with a pool of 5 slices of BFPE and FFPE renal amyloidosis, were collected and prepared for nLC-ESI MS/MS analysis. Samples were deparaffinised and digested as already described[11]. After the paraffin removal, antigen retrieval, and trypsinisation, the enzymatic reaction was stopped by adding TFA to a

final concentration of 0.5% to reach an acidic pH (<2). RapiGest™ SF Surfactant was removed by centrifuging samples (10 min, 13000 rpm). The supernatant was evaporated (Hetovac, Savant); dried peptides were resuspended in 50 µL of 0.1 % FA. Peptide content was quantified with NanoDrop (Thermo Scientific, Sunnyvale, CA, USA).

nLC-ESI-MS/MS analysis

nLC-ESI MS/MS analyses were performed coupling the nLC system online with timsTOF fleX™ (Bruker Daltonics, Bremen, Germany) mass spectrometer using a CaptiveSpray™ source, as already described, with slight modifications of the published method[12,13]. BFPE and FFPE renal samples at different fixation time points were analysed with Evosep One LC system (Evosep Biosystems, Odense, Denmark): 400 ng of peptides for each sample were loaded into a disposable trap column, Evotip Pure™ (Evosep Biosystems, Odense, Denmark) following the manufacturer protocol. Desalted and concentrated peptides were separated into an analytical 8 cm column (PepSep C18, 8cm Performance column, particle size of 1.5µm and internal diameter of 150µm) at a temperature of 40°C. For the separation, solvent A (0.1 % FA) and solvent B (ACN + 0.1 % FA) were used with a 21-minute gradient (60 SPD). BFPE and FFPE renal amyloidosis samples were analysed Dionex UltiMate 3000 rapid separation (RS) LC nanosystem (Thermo Scientific, Sunnyvale, CA, USA): 500 ng of tryptic peptides were separated in an analytical 50 cm nanocolumn (Thermo Scientific, Acclaim PepMap RSLC, 75 µm, 50 cm, nanoViper, C18, 2 µm) with a multistep 90 min gradient ranging from 4% to 98% of nanopump phase B (H_2O:ACN:FA 20:80:0.08).

The mass spectrometer was operated in DIA (Data Independent Acquisition)-PASEF (Parallel Accumulation-SErial Fragmentation) mode. Ions

were scanned in positive mode, over a *m*/*z* 100-1700 and mobility range of 0.85-1.30 V·s/cm². Dry gas flow was 3.0 L/min at 180°C. For tandem mass PASEF analysis, the cluster of mono-charged ions was excluded to reduce the complexity of MS2 spectra–using DIA windows of 25-26 Da. The mass spectrometer was calibrated for mass and ion mobility accuracy, using a mix of ten standards with a known mass (MMI-L Low Concentration Tuning Mix). For the ion calibration on nano-source, three specific lock masses (*m*/*z* 622.0290, *m*/*z* 922.0098 and *m*/*z* 1221.9906) have been added on the filter.

MALDI-MSI data and statistical analysis

The data derived from MALDI-MSI analysis was imported into a single SCiLS Lab 2023a Pro software (http://scils.de/; Bremen, Germany) file to perform baseline subtraction (Convolution algorithm), data normalisation (Total Ion Count algorithm), and to visualise the MS images and mean spectra of all regions. An *m*/*z* feature list of the whole dataset was generated using the "Feature finding" tool of SCiLS Lab, which utilises the Orthogonal Matching Pursuit (OMP) algorithm to account for the signal-to-noise ratio, peak shape, and frequency in the acquired spectra, thus reducing chemical noise and eliminating non-monoisotopic peaks. Subsequently, the Feature finding tool was used to generate two separate feature lists for BFPE and FFPE samples, including feature lists for samples fixed at different time points, to evaluate the effect of the type of fixative and fixation time on spectral quality; from the resulting data, Venn diagrams were generated with the aid of an open source platform to highlight common features among samples. The average intensity of peaks from samples fixed with different fixatives and for different intervals of time were exported from SCiLS Lab (interval processing mode: peak maximum), and, subsequently, Microsoft Excel 2016 (Microsoft, Redmond,

USA) was used to confront the intensity of peaks by calculating the overall percent coefficient of variation (CV%) of spectra. Average spectra of BFPE and FFPE samples, as well as average spectra at different time points, were imported in mMass for improved data visualisation.

Corresponding H&E digital slides (.ndpi format) were co-registered with the MALDI-MSI dataset in order to overlay molecular patterns and features with morphological structures. To achieve this, the MALDI-MSI dataset was also subjected to spatial segmentation with the bisecting k-means algorithms, employing weak spatial denoising, to cluster pixels based on their spectral similarity. Lastly, proteins of interest (podocin, nephrin, uromodulin (Tamm-Horsfall protein), low-density lipoprotein receptor-related protein 2 (LRP2), cytoplasmic actin (ACTB), elastin, apolipoprotein E (APOE), apolipoprotein A1 (APOA1), apolipoprotein A4 (APOA4), serum amyloid P component (SAP), and vitronectin (VTNC)) identified with nLC were also matched with features from the MALDI-MSI datased (mass error < 150 ppm) to verify signal distribution within principal renal sub-structures (glomeruli, tubules, and vessels, respectively) and within amyloid deposits.

nLC-ESI-MS/MS data and statistical analysis

Raw data derived from nLC-ESI-MS/MS were elaborated by using Spectronaut™ (v.18, https://biognosys.com) with human database (Swissprot, downloaded on 9 June 2022). The parameters were set as follows: trypsin as the enzyme, carbamidomethyl (C) as the fixed modifications, acetylation (protein N-term) and oxidation (M) as the variable modifications, 0.01 as a cutoff for precursor Q-value, and 1% FDR at both precursor and protein levels. Abundance values were automatically normalised across runs. Proteins were

considered identified and eligible for quantitation only if they had at least one and two significant peptides, respectively.

The statistical analysis was performed considering only quantified proteins with MetaboAnalyst 6.0, an open-source platform for statistical analysis of omics datasets, normalising data with log transformation (base 10). Student's T-test was carried out (*p value* < 0.001 with Benjamini–Hochberg adjustment for multiple comparisons) to pinpoint the most significantly varied proteins, and these were used to generate a heatmap (distance measure: Euclidean; clustering method: Ward); subsequently, a Volcano plot (fold change threshold: 1.5; *p value* threshold: 0.05 with Benjamini–Hochberg adjustment for multiple comparisons) was generated and Principal Component Analysis was performed.

Results

The influence of different fixative conditions on the proteomic profile of renal tissue

The influence of different fixative conditions on the proteomic profile of tissue was evaluated considering the following aspects: (1) number of common molecular features detected in the MALDI-MSI dataset; (2) variability in the intensity of the detected molecular features using the Coefficient of Variation (CV%); (3) delineation of the principal morphological structures with spatial segmentation; (4) comparative protein quantitation based on nLC-ESI-MS/MS.

Number of common features among different fixative conditions

As a first comparison, peaklists from BFPE and FFPE samples were analysed to assess whether different fixatives could influence the protein profiles generated by MALDI-MSI. In total, 340 and 322 features were detected in BFPE and FFPE renal tissue, respectively, and, among them, a total of 270 features (68.9%) were found to be present in tissue processed with either fixative, highlighting a substantial degree of common features (**Figure 1.a**). Furthermore, the same comparison was repeated for cases fixed for various lengths of time, revealing that for both BFPE and FFPE datasets, samples fixed for 12h and 24h shared a higher number of common features that were not presents in samples fixed for 2h (12.2% and 13.2%, respectively); moreover, samples fixed for 2h from both datasets showed a higher number of unique features (8.2% and 16.0%, respectively (**Figure 1.b-c**). **Figure 1.d** displays the average proteomics profiles, or overview spectra, obtained from the BFPE and FFPE renal tissue, with the average protein profiles obtained using different fixation times (2h, 12h, and 24h) being reported in **Supporting Information, S1**.

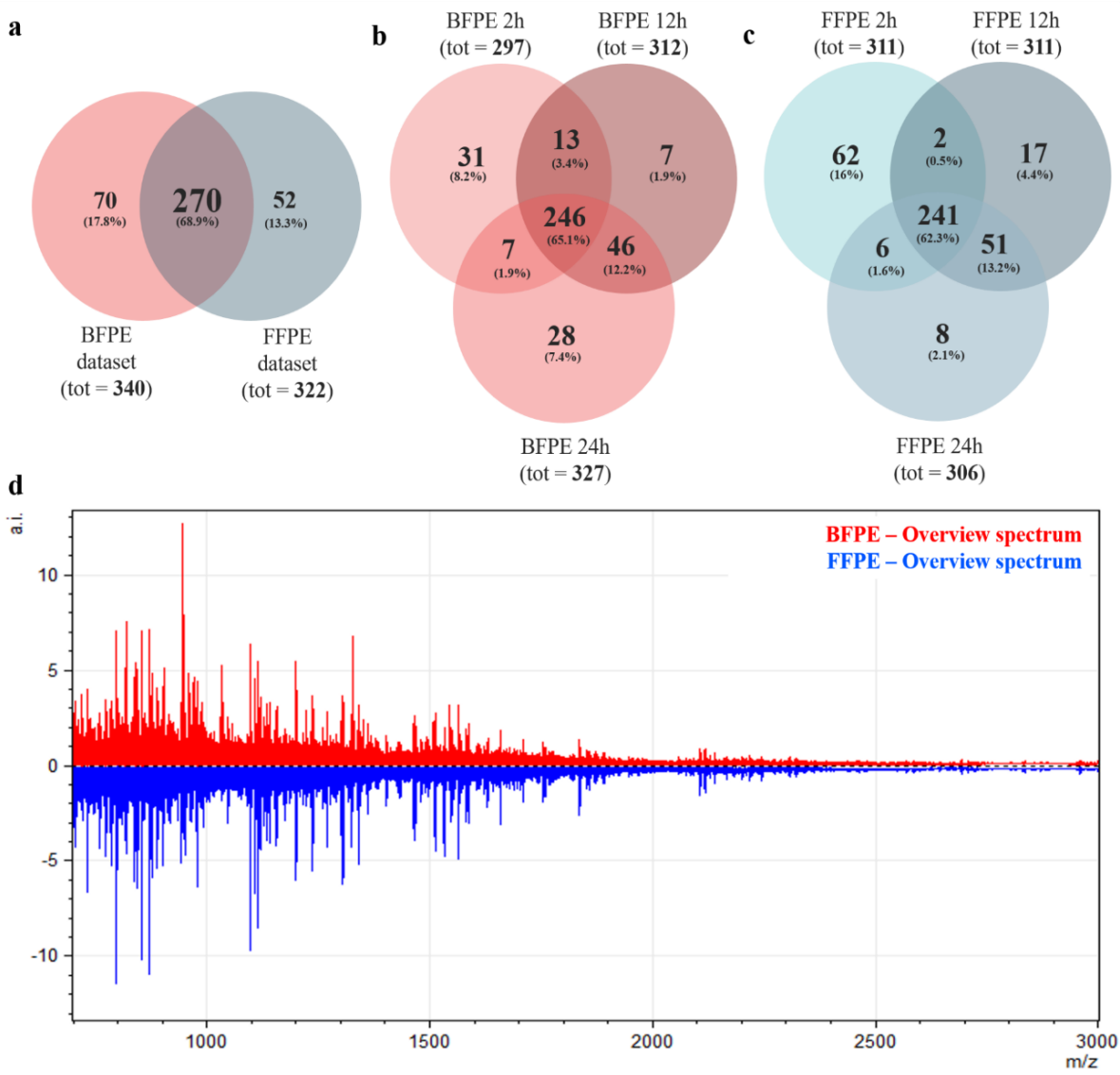

Figure 1: **a)** Venn diagram of features detected in the average protein profile of BFPE (tot = 340 features) and of FFPE renal tissue (tot = 322 features), highlighting a prevalence of common features (tot = 270 features, 68.9%) amongst datasets; **b)** Venn diagram of features found in the average protein profile of BFPE cases fixed for 2h (tot = 297 features), 12h (tot = 312 features), and 24h (tot = 327 features); **c)** Venn diagram of features found in the average protein profiles of FFPE specimens fixed for 2h (tot = 311 features), 12h (tot = 311 features), and 24h (tot = 306 features); **d)** Average protein profiles obtained from BFPE (red) and FFPE (blue) renal tissue.

Variation in intensity of the detected molecular features

Subsequently, the percent Coefficient of Variation (CV%), both deriving from analytical variability or different fixatives and fixation times, was measured. The CV% representative of the analytical variability was evaluated between replicates treated under the same conditions (fixative/times), showing substantial comparability for BFPE and FFPE samples (10.22% and 10.06%, respectively, **Table 1.a**). Analysing the additional contribution of fixative/time highlighted an increased CV% for samples fixed for 2h, especially in the instance of BFPE tissue (**Table 1.b**). Finally, independently from the analytical variability, the molecular features detected in the BFPE and FFPE renal tissue still showed an acceptable degree of variability when alternative fixatives (19.45%, **Table 1.c**) or fixation durations (2h: 22.42%; 12h: 18.92%; 24h: 22.73%; **Table 1.d**) were considered.

1.a	Second replicates	
First replicates	BFPE	FFPE
BFPE	10.22%	
FFPE		10.06%

1.c	FFPE
BFPE	19.45 %

1.b	Second replicates					
First replicates	BFPE 2h (n=1)	BFPE 12h (n=2)	BFPE 24h (n=2)	FFPE 2h (n=1)	FFPE 12h (n=2)	FFPE 24h (n=2)
BFPE 2h (n=1)	27.01 %					
BFPE 12h (n=2)		10.71 %				
BFPE 24h (n=2)			9.91 %			
FFPE 2h (n=1)				15.27 %		
FFPE 12h (n=2)					12.50 %	
FFPE 24h (n=2)						9.97 %

1.d	FFPE 2h (n=4)	FFPE 12h (n=2)	FFPE 24h (n=4)
BFPE 2h (n=2)	22.42 %		
BFPE 12h (n=4)		18.92 %	
BFPE 24h (n=4)			22.73 %

Table 1. Coefficient of Variation (CV%) calculated by comparing **a)** The intensity of the molecular features detected in analytical replicates of samples fixed with the same fixative; **b)** The intensity of the molecular features detected in samples fixed with the same fixative for different periods of time; **c)** The intensity of the molecular features detected in all of the BFPE and FFPE renal tissue samples; **d)** The intensity of the molecular features detected in both BFPE and FFPE renal tissue samples fixed for different periods of time. Please mind that for FFPE and BBFE samples fixed for 2h only WB were available, as reported in the Matherials and Methods section "Cases".

Spatial segmentation of BFPE and FFPE renal tissue

Subsequently, MALDI-MSI data obtained from the BFPE and FFPE renal tissue underwent spatial segmentation, which clusters pixels based on their spectral similarity in an unsupervised manner, in order to determine whether the principal renal parenchyma regions (cortical and medullary) could be delineated independently from the type of fixation and the fixation time. Spatial segmentation highlighted renal regions with spectral similarities between BFPE and FFPE samples (red, **Figure 2.a**), mainly corresponding to the annotation of renal medulla by pathologists (**Figure 2.b**), and areas with different spectral patterns (blue and yellow) which correspond to the cortical regions in the BFPE and FFPE tissue, respectively. Moreover, a higher degree of spectral variability was observed for CNB samples which had been fixed for 2h

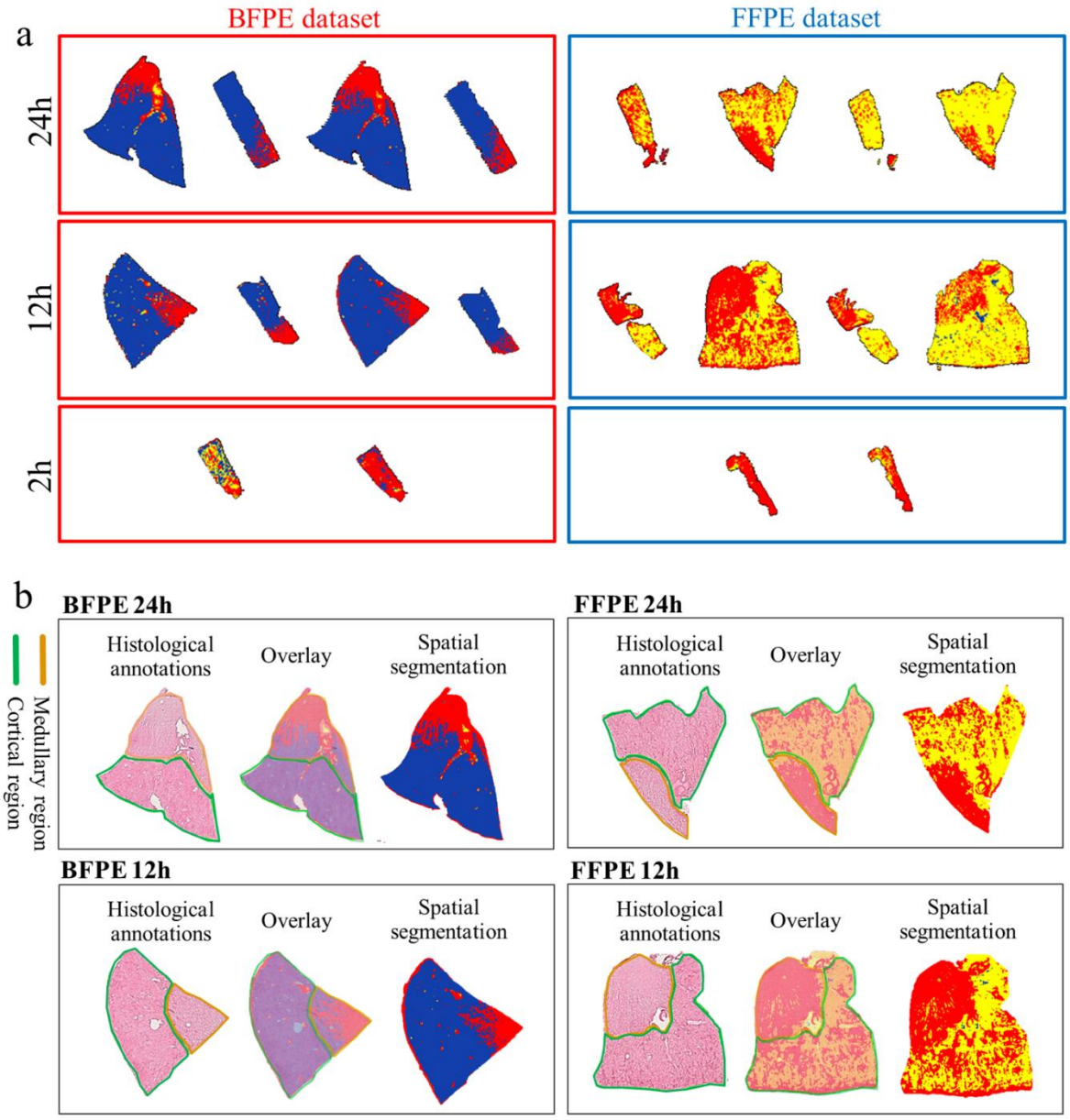

Figure 2. a) Spatial segmentation displaying the first three branches of the cluster tree, where pixels are colour-coded based on spectral similarity in blue, yellow, or red; **b)** Overlay of the segmentation maps with histological images of the renal tissue annotated by the pathologist (orange line, medullary region; green line, cortical region). For all examples considered, the pixels highlighted in blue correlate with the cortical region of BFPE tissues, whilst the yellow pixels represent the cortical region of FFPE specimens. The red region does not discriminate among fixatives or fixation time, and for all cases corresponds to the medullary region of the kidney.

Comparative protein quantitation by nLC-ESI-MS/MS

Finally, label-free quantitative proteomics analysis among BFPE and FFPE samples was performed using nLC-ESI-MS/MS. A total of 4333 proteins were quantified and, among these, a total of 154 features varied significantly between the BFPE and FFPE tissue samples (*p value* < 0.001), with the highest variability noted for those samples fixed for 2h, as already noted in the MALDI-MSI dataset (**Supporting Information, S2**). This selected subgroup of significantly varied proteins was used to generate a heatmap (**Figure 3.a**), showing a cluster of proteins whose abundance was impacted by the type of fixative. However, the influence of fixative was estimated to account for only 6% (*p value* < 0.05) of the total number of proteins quantified in the BFPE and FFPE samples, as displayed in the Volcano plot (**Figure 3.b**). The complete list of genes coding for proteins which were significantly enriched or depleted within the dataset is available in **Supporting Information, TS1**.

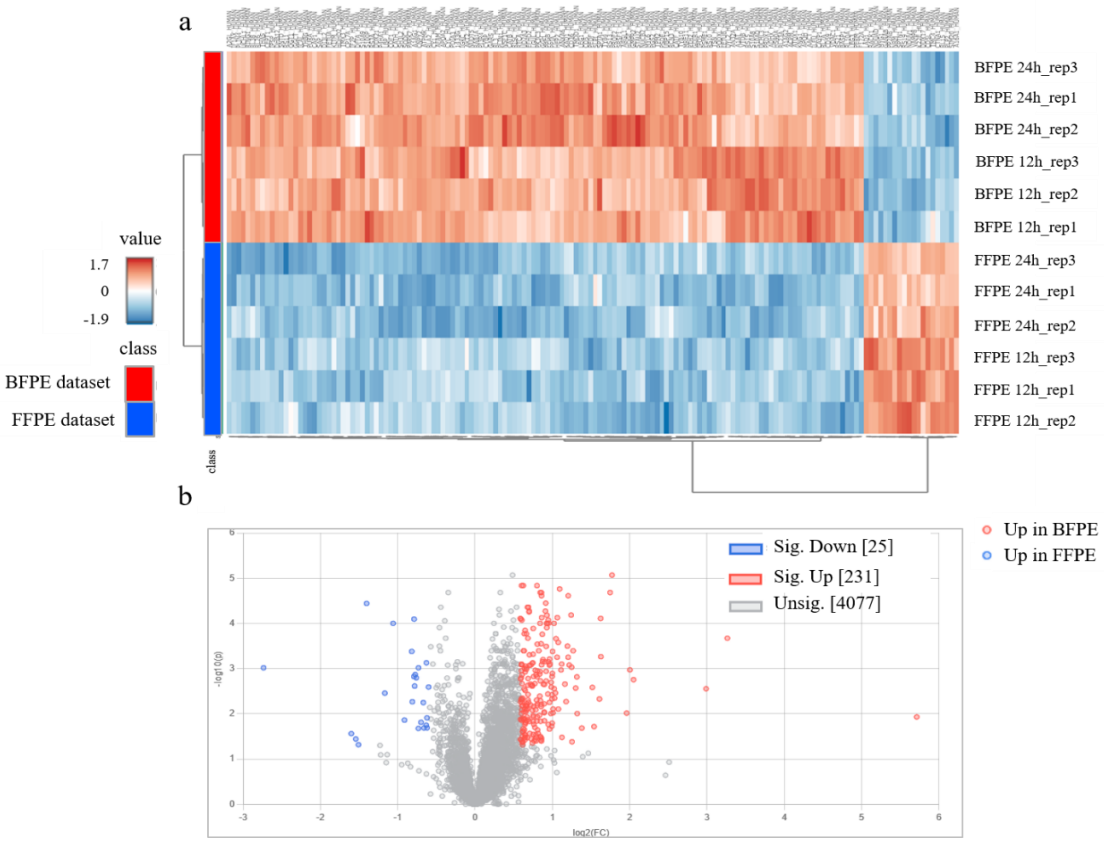

Figure 3. **a)** Heatmap displaying the abundance of the most significantly varied proteins (n = 154, $p < 0.001$) within BFPE and FFPE samples fixed for 12h and 24h; BFPE samples (red) and FFPE samples (blue) are separated in two different branches of the dendrogram **b)** The volcano plot highlights 231 proteins which are increased in BFPE and 25 proteins which are increased in FFPE samples, out of a total of the 4333 quantified.

The detection of renal sub-structures in BFPE and FFPE tissue

After assessing the comparability of the protein profiles generated from BFPE and FFPE renal tissue with MALDI-MSI, the tissue distribution of the detected proteins was also evaluated to determine any impact of the fixative, especially in extreme conditions (*e.g.* low fixation time, 2h) which may often be encountered in a routine nephropathology setting. To achieve this, six proteins of interest, which were identified with nLC-ESI-MS/MS in both BFPE and FFPE samples and are known to present specificity for the principal renal substructures, were mapped. For all proteins, a coherent tissue distribution amongst 12h and 24h-fixed tissue was observed in the expected renal sub-structures, as shown in **Figure 4**. Interestingly, although they showed greater variability in terms of protein content, both BFPE and FFPE samples fixed for 2h still presented a coherent distribution for the substructure-specific proteins mapped (**Supporting Information, TS2**)

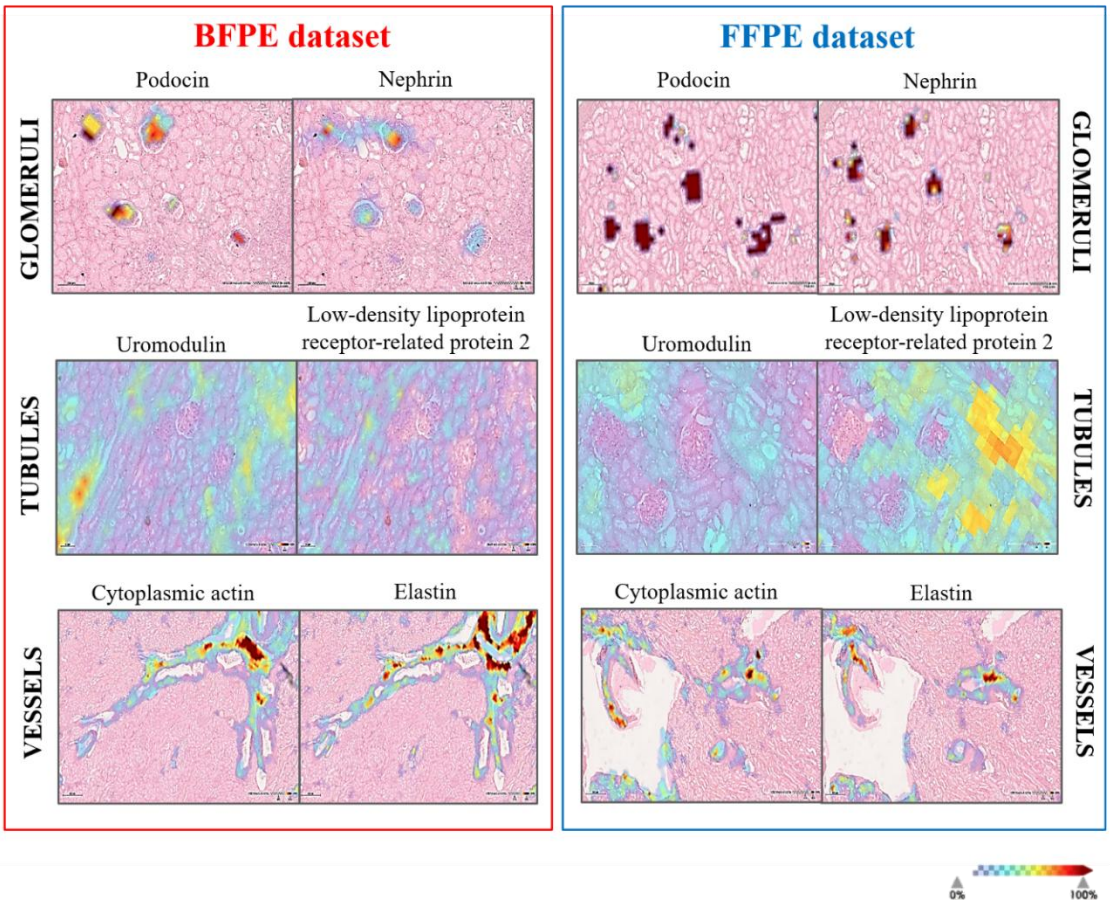

Figure 4. Representative MALDI-MSI images displaying the tissue distribution of proteins which are specifically expressed in glomeruli (podocin, *m/z* 1073.55; nephrin, *m/z* 1473.69), tubules (uromodulin, *m/z* 1117.52; LRP2, *m/z* 786.46), and vessels (ACTB, *m/z* 1722. 78; elastin, *m/z* 1729.79) within BFPE and FFPE renal tissue.

Amyloid detection in BF and FF renal biopsies: a proof-of-concept assessment

The ability of MALDI-MSI to detect and localise amyloid *fingerprint* proteins, which has been previously confirmed in FFPE tissues[10], was also assessed with BFPE samples as a use case. Using a recently described protocol for amyloid *fingerprint* protein detection on FFPE CNBs[10], the pipeline was adopted on a BFPE renal biopsy. This comparison demonstrated the feasibility to detect the presence of the principal amyloid *fingerprint* proteins and underline their colocalisation within amyloid deposits in BFPE tissue,

corresponding to the annotations of the renal pathologist on the Congo Red stained tissue and presented the same reliability as the FFPE counterpart. (**Figure 5**). The identified tryptic peptides of these proteins and their comparability among the two fixatives was also confirmed by the label-free quantitative analysis performed with nLC-ESI-MS/MS (**Supporting Information, S3)**.

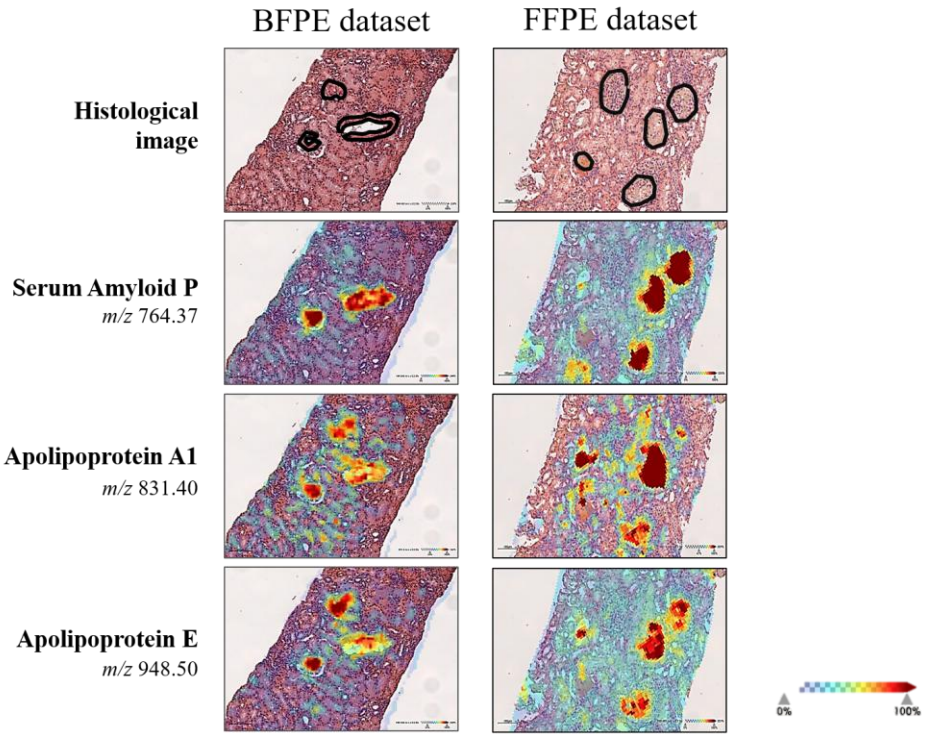

Figure 5. MALSI-MSI images of the principal amyloid *fingerprint* proteins (Apolipoprotein E, *m*/*z* 948.50; Apolipoprotein A1, *m*/*z* 831.40; Serum Amyloid P component, *m*/*z* 764.37) in BFPE and FFPE renal amyloidosis samples.

Discussion

A valuable yet untapped resource for molecular and diagnostic research techniques lies in pathology archives enriched with Bouin-fixed paraffin-embedded renal tissue, routinely stored for years using Bouin's fixative in renal pathology. Previous studies have attempted to investigate whether Bouin-fixed specimens are suitable for proteomic analysis using traditional MS-based techniques (*e.g.* LC-MS/MS) and have suggested that BFPE tissue archives can be fruitfully exploited for gathering data from particularly precious cases, although molecular biases and technical constraints exist[14]. Whilst studies have presented the application of MALDI-MSI on BFPE tissues (*e.g.* human testis) with promising results, none have preceded to assess the technical reliability of this method through the direct parallel analysis of coupled FFPE cases[15]. Thus, starting from our previous results on FFPE renal biopsies in the context of different kidney diseases[7,10,16–18], here we sought to investigate whether BFPE samples are equally suitable for spatial proteomics analysis with MALDI-MSI in order to further enrich the capabilities of this tool and, subsequently, unlock a wide retrospective series of rare renal diseases that can be exploited to increase our knowledge in this field.

Here, the technical comparison among differently fixed samples documented a large degree of overlap in terms of the number of detected protein features (68.9%), with a relatively overall low Coefficient of Variation when comparing the intensity of the features detected in BFPE and FFPE renal tissue (10.22 and 10.06%, respectively), demonstrating the reliability of Bouin-fixation for the detection of tryptic peptides on renal tissue. Moreover, the application of MALDI-MSI facilitated the separation of different renal parenchyma regions (cortical and medullary) with both fixatives, with only slight differences observed within the cortical regions. Label-free protein

quantification through nLC-ESI-MS/MS further unveiled the similarity of the renal tissue treated with either fixative, confirming the presence of only minor differences, limited to 6% of the quantified features.

Notwithstanding the slight differences noted in the proteomic profiles of BFPE and FFPE renal tissue, the capacity to reliably map proteins within specific renal structures (e.g. podocin in glomeruli, uromodulin in tubules, and actin in vessels), demonstrated the suitability of BFPE specimens for the spatial proteomics assessment of renal parenchyma, generating largely comparable results to their FFPE counterparts. Whilst these results suggest that the application of MALDI-MSI in BFPE is feasible, a higher degree of proteomic variability was, however, noted in samples with a reduced fixation time (2h) independently from the fixative used, both from a semi-quantitative and a spatial point of view. Whilst this scenario is most relevant to renal pathology, where core needle biopsies are typically fixed for a few hours with little standardisation (ranging from 2 to 12 hours), we used this threshold here as an additional proof-of-concept to further demonstrate the reliability of these samples. This is testified by the overall Coefficient of Variation, which, although determined to be 19.45% and higher than observed in tissue fixed for 12h and 24h, is still below the CV threshold of 20% stated by The European Medicine Agency (EMA) for analytical techniques used to determine the concentration of a given analyte in a biological matrix[19]. Based on these promising results which point to the possibility of analysing BFPE samples with MALDI-MSI, future studies could be directed towards the assessment of the coefficient of variation of samples over time, specifically focusing on the influence of environmental factors such as humidity and storage time, of BFPE samples.

Finally, once the feasibility of performing MALDI-MSI spatial proteomics analysis in BFPE tissue was demonstrated, cases of renal amyloidosis were selected to document the real-world feasibility of performing MALDI-MSI on a BFPE kidney bioptic sample obtained from routine clinical archives. Here, the comparable detection of amyloid *fingerprint* proteins in both BFPE and FFPE cases of renal amyloidosis confirmed the applicability of this approach in BFPE renal samples. As a consequence, these findings suggest that renal pathology archives containing vast numbers of BFPE biopsies from cases with renal amyloidosis can also be used to further optimise this MALDI-MSI-based approach for detecting and subtyping this disease. Additionally, they can amplify the statistical significance of the case series, particularly for cases that arise from rarer subsets of precursors among the over 30 proteins known to have amyloidogenic potential[20–22].

Conclusion

This feasibility study demonstrates the possibility to perform MALDI-MSI on BFPE pathology samples, showing only minor proteomic variations with respect to the standard FFPE tissue specimens. Collectively, these results suggest the utility of BFPE tissue specimens in MSI-based research in molecular pathology, allowing its wider application in the retrospective archives of nephropathology centres. Further studies using other renal-world dedicated fixatives, such as Serra's solution, may further enrich our technical knowledge in this area and increase the number of precious renal tissue samples available for larger-scale MSI-based research in molecular pathology.

Supporting Information

Supporting Information is available at https://drive.google.com/drive/folders/14ph4fe_yw-6V7AUfRP_knpftR3kLd4iX

References

1. He, B., Huang, Z., Huang, C. & Nice, E. C. Clinical applications of plasma proteomics and peptidomics: Towards precision medicine. *Proteomics Clin. Appl.* **16**, e2100097 (2022).
2. Piga, I., Magni, F. & Smith, A. The journey towards clinical adoption of MALDI-MS-based imaging proteomics: from current challenges to future expectations. *FEBS Lett.* (2023) doi:10.1002/1873-3468.14795.
3. De Sio, G. *et al.* A MALDI-Mass Spectrometry Imaging method applicable to different formalin-fixed paraffin-embedded human tissues. *Mol. Biosyst.* **11**, 1507–1514 (2015).
4. Winter, M., Tholey, A., Kristen, A. & Röcken, C. MALDI Mass Spectrometry Imaging: A Novel Tool for the Identification and Classification of Amyloidosis. *Proteomics* **17**, (2017).
5. L'Imperio, V., Smith, A., Chinello, C., Pagni, F. & Magni, F. Proteomics and glomerulonephritis: A complementary approach in renal pathology for the identification of chronic kidney disease related markers. *Proteomics Clin. Appl.* **10**, 371–383 (2016).
6. Angelotti, M. L., Antonelli, G., Conte, C. & Romagnani, P. Imaging the kidney: from light to super-resolution microscopy. *Nephrol. Dial. Transplant* **36**, (2021).
7. Smith, A. *et al.* High Spatial Resolution MALDI-MS Imaging in the Study of Membranous Nephropathy. *Proteomics Clin. Appl.* **13**, e1800016 (2019).
8. Walker, P. D., Cavallo, T., Bonsib, S. M. & Ad Hoc Committee on Renal Biopsy Guidelines of the Renal Pathology Society. Practice guidelines for the renal biopsy. *Mod. Pathol.* **17**, 1555–1563 (2004).
9. Najafian, B., Lusco, M. A., Alpers, C. E. & Fogo, A. B. Approach to Kidney Biopsy: Core Curriculum 2022. *Am. J. Kidney Dis.* **80**, 119–131 (2022).
10. Bindi, G. *et al.* Spatial resolution of renal amyloid deposits through MALDI-MSI: a combined digital and molecular approach to monoclonal gammopathies. *J. Clin. Pathol.* (2023) doi:10.1136/jcp-2023-208790.
11. Principi, L. *et al.* Proteomic Fingerprint of Lung Fibrosis Progression and Response to Therapy in Bleomycin-Induced Mouse Model. *Int. J. Mol. Sci.* **24**, (2023).
12. Previtali, P. *et al.* Towards the Definition of the Molecular Hallmarks of Idiopathic Membranous Nephropathy in Serum Proteome: A DIA-PASEF Approach. *Int. J. Mol. Sci.* **24**, (2023).
13. Pagani, L. *et al.* Plasma Proteomic Variables Related to COVID-19 Severity: An Untargeted nLC-MS/MS Investigation. *Int. J. Mol. Sci.* **24**, (2023).
14. Tanca, A. *et al.* Evaluation of the suitability of archival Bouin-fixed paraffin-embedded tissue specimens to proteomic investigation. *Electrophoresis* **33**, 1375–1384 (2012).
15. Lahiri, S. *et al.* MALDI-IMS combined with shotgun proteomics identify and localize new factors in male infertility. *Life Sci Alliance* **4**, (2021).
16. Smith, A. *et al.* The putative role of MALDI-MSI in the study of Membranous Nephropathy. *Biochim. Biophys. Acta: Proteins Proteomics* **1865**, 865–874 (2017).

17. L'Imperio, V. *et al.* MALDI imaging in Fabry nephropathy: a multicenter study. *J. Nephrol.* **33**, 299–306 (2020).
18. L'Imperio, V. *et al.* MALDI-MSI Pilot Study Highlights Glomerular Deposits of Macrophage Migration Inhibitory Factor as a Possible Indicator of Response to Therapy in Membranous Nephropathy. *Proteomics Clin. Appl.* **13**, e1800019 (2019).
19. Guideline on bioanalytical method validation. https://www.ema.europa.eu/en/documents/scientific-guideline/guideline-bioanalytical-method-validation_en.pdf. (accessed on 6 June 2021).
20. Ihne, S. *et al.* Amyloidosis—the Diagnosis and Treatment of an Underdiagnosed Disease. *Deutsches Ärzteblatt International* **117**, 159 (2020).
21. Wechalekar, A. D., Gillmore, J. D. & Hawkins, P. N. Systemic amyloidosis. *Lancet* **387**, 2641–2654 (2016).
22. Wisniowski, B. & Wechalekar, A. Confirming the Diagnosis of Amyloidosis. *Acta Haematol.* **143**, 312–321 (2020).

2.4 Single-slide detection and typing of AL renal amyloidosis: combining mass spectrometry imaging and digital pathology

Adapted from:

Bindi, G.[1], Cazzaniga, G.[2], Alberici, F.[3], Mescia, F.[3], Mannino, M.[2], Maggioni, A.[2], Galimberti, S.[4], Capitoli, G.[4], & Fisogni, S.[5], Magni, F.[1], Pagni, F.[2], Smith, A.[1], L'Imperio, V.[2]. (**2025**).
Single-slide detection and typing of AL renal amyloidosis: combining mass spectrometry imaging and digital pathology.
Amyloid. pp. 1-9.
doi: 10.1080/13506129.2025.2530532.

[1] Department of Medicine and Surgery, Proteomics and Metabolomics Unit, University of Milano - Bicocca, Monza, Italy
[2] Department of Medicine and Surgery, Pathology, University of Milan-Bicocca, IRCCS Fondazione San Gerardo dei Tintori, Monza, Italy
[3] Nephrology Unit, Spedali Civili Hospital, ASST Spedali Civili di Brescia, Brescia, Italy
[4] Bicocca Bioinformatics Biostatistics and Bioimaging B4 Centre, School of Medicine and Surgery, University of Milan - Bicocca (UNIMIB), Monza, Italy
[5] Section of Pathology, Department of Molecular and Translational Medicine, Spedali Civili, University of Brescia, Brescia, Italy.

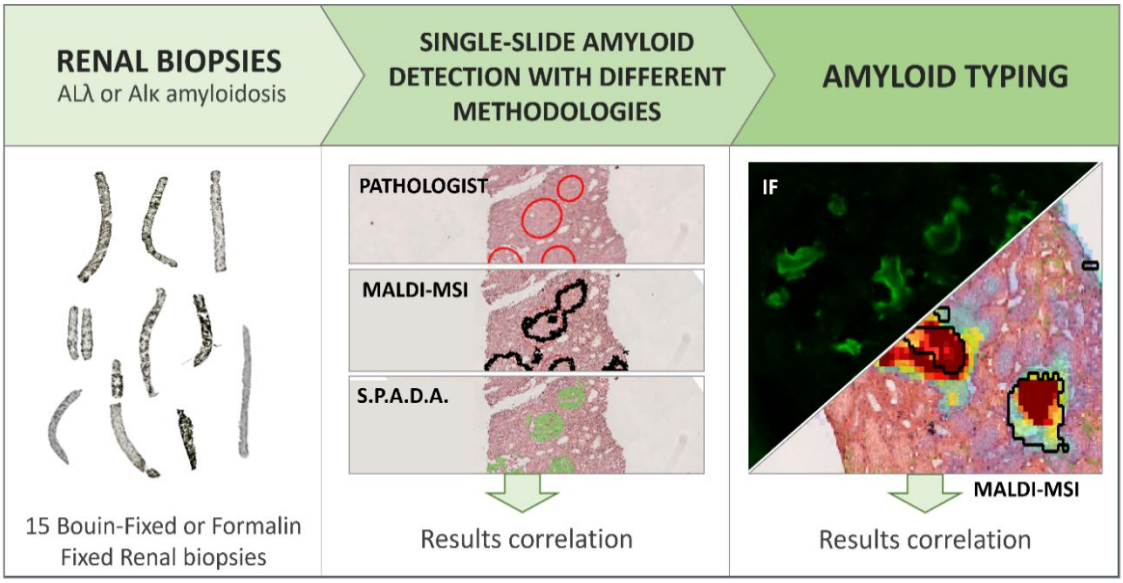

Abstract

Amyloid typing, particularly in Monoclonal Gammopathies of Renal Significance, can be technically challenging. Matrix-Assisted Laser Desorption/Ionisation-Mass Spectrometry Imaging (MALDI-MSI) has been proposed as a non-destructive method to detect and type amyloid deposits on a single tissue slide. This study aims to confirm this capability of MALDI-MSI in renal light chain amyloidosis (AL amyloidosis), irrespective of the fixative utilised, confronting results with other traditional and upcoming methods for amyloid detection. MALDI-MSI was applied to 15 renal biopsies diagnosed with AL amyloidosis. Results were compared with the routinely utilised methods of amyloid detection and typing, respectively the pathologist's evaluation and immunofluorescence (IF), and additionally with a computational technique for amyloid detection, SPADA (Streamlined Pipeline for Amyloid Detection Through Congo Red Fluorescence Digital Analysis). MALDI-MSI demonstrated an agreement of 85.0% and 86.4% with SPADA and the pathologist in detecting glomerular deposits. It also showed complementary potential with SPADA, suggesting the possibility of combining all methodologies on a single tissue slide. Furthermore, MALDI-MSI showed a complete agreement with IF in amyloid typing. This study confirmed the capability of MALDI-MSI to detect and type AL amyloidosis, assessing the possibility to integrate an additional, computational method for amyloid detection on a single tissue slide.

Introduction

Characterisation of the responsible precursor protein in renal amyloidosis is of paramount importance to define the therapeutic strategy, given that cases related to monoclonal components (light chain amyloidosis, AL; heavy chain amyloidosis, AH) should be treated with aggressive chemotherapy[1,2]. In the majority of cases, the employment of light microscopy (LM), immunofluorescence/immunohistochemistry (IF/IHC), and transmission electron microscopy (TEM) on renal biopsies can be sufficient to ascribe amyloid deposits to the group of so-called Monoclonal Gammopathies of Renal Significance (MGRS)[3,4,5]. However, the subsequent application of these techniques can deplete the sample and reduce material available for further analyses, leading to a paradigm shift toward more sensitive and specific techniques such as Mass Spectrometry (MS)[6], which can concurrently provide information regarding precursor proteins (e.g., monoclonal light chains) as well as the so-called *fingerprint* proteins (*e.g.*, Serum Amyloid P-component)[7]. Notwithstanding the high potential, the most widely reported MS-based technique for this purpose requires dedicated tissue sections for laser microdissection (LMD), which results in consequent tissue destruction and a lack of morpho-molecular correlation[8]. Moreover, this approach still relies upon the morphological identification of fibrillar deposits with Congo red by pathologists, which can be troublesome, especially in the case of subtle or minimal disease[6,9]. Along these lines, *in situ* proteomics techniques, in particular Matrix-Assisted Laser Desorption/Ionisation Mass Spectrometry Imaging (MALDI-MSI)[10], constitute a valid alternative given that they provide highly specific and sensitive proteomic information, all whilst maintaining the spatial and morphological integrity of the biopsy. In fact, MALDI-MSI has been previously utilised to detect and type amyloid deposits within the renal

parenchyma[11,13] and our group implemented a workflow which enabled the automatic segmentation and typing of amyloid plaques in routine Formalin-Fixed Renal Biopsies (FFRBs)[14].

Building upon these initial findings, this work seeks to confirm the applicability of MALDI-MSI for the detection and typing of renal amyloidosis, even in the instance of Bouin-Fixed Renal Biopsies (BFRBs), which represent a significant proportion of specimens present in nephropathology archives worldwide and have been recently shown to be a useful specimen type for MALDI-MSI proteomics studies[15]. In this setting, this spatial proteomics approach is integrated and confronted with another recently described computational approach, the Streamlined Pipeline for Amyloid Detection Through Congo Red Fluorescence Digital Analysis (SPADA) pipeline[16], on the same tissue slide. Moreover, the capability of MALDI-MSI to perform typing of AL amyloidosis in BFRBs is presented, with respect to traditional IF, further underscoring the capability of this technique to detect and type amyloidosis on a single tissue slide irrespective of the fixative utilised.

Materials and Methods

Cases

A retrospective cohort of 10 BFRBs with a diagnosis of AL amyloidosis were retrieved from the archives of the Pathology Departments of Spedali Civili di Brescia; 5 Formalin FRBs (FFRBs) with a diagnosis of AL amyloidosis were obtained from Fondazione IRCCS San Gerardo di Monza, Italy. IF was performed for κ (FITC anti-κ Polyclonal Primary Antibody, Ventana®, Roche. Concentration: 0.3 μg/mL) and λ (FITC anti- λ Polyclonal Primary Antibody, Ventana®, Roche. Concentration: 20 μg/mL) immunoglobulin light chains on

fresh/frozen tissue at the diagnosis (Ultra Benchmark, Ventana, Roche). In addition to AL amyloidosis cases, 3 retrospective membranous nephropathy cases obtained within a "Ricerca Finalizzata" trial (GR-2021-12374235 - PROFOUND) were used as negative controls, together with 3 normal Formalin-fixed renal tissues retrieved from nephrectomy surgical samples (leftover material, cortex away from tumour). For AL amyloidosis renal biopsies, clinical data (age, serum creatinine at diagnosis, proteinuria, and serum/urine monoclonal component-M spike) was also collected. Approval was obtained from the local ethics committee.

Sample preparation for MALDI-MSI

The complete list of chemicals and reagents utilised is available at **Supplementary Information, S1**. For each sample type, six-micrometre-thick sections were cut and mounted on conductive Indium Tin Oxide (ITO) glass slides. Sample preparation was carried out according to our previously published method, which includes deparaffinisation, tissue rehydration, antigen retrieval, tryptic digestion, and MALDI matrix application[14].

MALDI-MSI analysis

All tissues were analysed with a rapifleX MALDI TyssueTyper™ (Bruker Daltonics, Bremen, Germany) equipped with a Smartbeam™ 3D laser operating at a 10kHz laser repetition rate, in positive reflectron mode within the *m*/*z* 700-3000 range. A raster setting of 10 μm and a beam scan of 6 μm in the *x* and *y* dimensions were utilised. Instrument calibration was carried out with PepMixI. FlexControl 4.2 and FlexImaging 6.0 (Bruker Daltonics, Bremen, Germany) were used to set the image acquisition parameters. After MALDI-MSI analysis, the matrix was removed from each sample with increasing concentrations of ethanol (70%, 90%, and 100%), and the slides were stained

with Congo Red to be subjected to the pathologist's evaluation and the SPADA pipeline.

Computational SPADA pipeline

After MALDI-MSI and Congo Red staining, slides were digitally scanned using a NanoZoomer S60 (Hamamatsu, Shizuoka, Japan) at 20× magnification in brightfield and darkfield mode using two fluorescence filter combinations, as previously described[16]:

- Texas red filter—TRITC—(556/20 excitation—617/73 emission).
- A scramble filter combination to detect autofluorescence in tissue (480/17 excitation—617/73 emission).

Obtained whole slide images (WSIs) were submitted to an expert nephropathologist (VL) for the delineation of regions of interest containing amyloid deposits and obtained annotations were exported for the colocalisation with the deposits found with MALDI-MSI. Then, the SPADA pipeline was applied on obtained Congo Red Fluorescence virtual slides (CRFvs) to automatically segment amyloid deposits and consequently obtained regions of interest (ROIs) which were exported to create masks for the overlay with MALDI-MSI ROIs.

MALDI-MSI data analysis

Raw data obtained for each measurement region was imported into a single SCiLS Lab 2024b Pro file (Bruker Daltonics, Bremen, Germany). Data was normalised (Total Ion Count algorithm), and baseline subtraction was performed (Convolution algorithm). Subsequently, the *m*/*z* value of tryptic fragments derived from amyloid *fingerprint* proteins (Apolipoprotein E, APOE_HUMAN; Apolipoprotein A1, APOA1_HUMAN; Apolipoprotein A4,

APOA4_HUMAN; Vitronectin, VTNC_HUMAN; Serum amyloid P-component, SAMP_HUMAN), which were present either in the previously described panel[14] or in an *in house* kidney protein library generated by tryptic digestion and nLC-ESI-MS/MS analysis of the renal amyloid samples included in the study, were correlated with *m*/*z* features present in the MALDI-MSI dataset (mass error ≤ 150 ppm, monoisotopic) to generate a novel, more comprehensive target list of 31 amyloid *fingerprint* peptides (**Supplementary Information, T1**). The same process was also performed in order to generate a novel, more comprehensive target list for the amyloid precursor proteins of ALκ and ALλ amyloidosis, namely various fragments of immunoglobulin κ variable (KV), immunoglobulin κ constant (IGK), and immunoglobulin λ variable (LV) (**Supplementary Information, T2**), for a total of 20 target tryptic fragments.

To putatively annotate areas of amyloid deposition, spatial segmentation (Bisecting k-means algorithm, very strong spatial denoising), using the feature list reported in **Supplementary Table 1**, was performed on each individual biopsy, according to our previously published workflow[14]. Areas identified as putative amyloid deposits were saved as regions of interest (ROIs) and the mean spectrum of these ROIs was obtained for each case. Subsequently, the intensity of features (Maximum Intensity; Interval processing mode: Peak Maximum) reported in **Supplementary Table 2** was assessed in the annotated ROIs to assign a subtype (either ALκ or ALλ) to each amyloidosis case, according to the workflow previously described[14]. Subsequently, the maximum intensities of κ and λ tryptic fragments in deposits of AL amyloidosis cases and in the glomeruli of Membranous Nephropathy (MN) and healthy controls (CTRL)[14] were obtained and summed for each sample to estimate the increase of immunoglobulin κ or λ light change tryptic fragments in amyloidosis and control cases. Subsequently, these values were

imported in GraphPad Prism 5 (GraphPad Software Inc., California, USA) to generate a bar chart of the intensities of κ and λ fragments in different sample types.

Statistical analysis

For continuous variables, mean and standard deviation (SD) were calculated, whilst qualitative variables were reported as count and frequency. For the comparison of means and qualitative variables, Student's T-test, Fisher's exact test and X^2 test were used, considering *p values* < 0.05 as statistically significant. Statistics were extracted using Excel 2016 (Microsoft) and Python 3.10 libraries pandas and scikit-learn.

Results

Cases

The clinical, laboratory, and histologic characteristics of the patients included in the study are shown in **Table 1**. Patients' mean age was 62.0 (± 14.7) years, serum creatinine 2.1 (± 1.4 mg/dl), and proteinuria 4.7 (± 2.9 g/24h) at the time of diagnosis. All cases were diagnosed with AL amyloidosis, of which 10 were typed as AL λ amyloidosis and 5 were typed as AL κ amyloidosis based on IF. The IF study (data not shown) demonstrated exclusive positivity for lambda or κ in almost all cases, except for case BFRB#10 in which only a slight prevalence of λ on κ was recorded (4+ vs. 2+). No statistically significant differences were noted in terms of age (62.2 ± 11.5 vs. 61.6 ± 21.3, p=0.9), serum creatinine (1.9 ± 1.5 vs. 2.5 ± 1.4, p=0.4), and proteinuria (4.8 ± 2.5 vs. 4.5 ± 3.8, p=0.8) between the AL λ and AL κ amyloidosis cases. On histopathological examination, the mean number of globally sclerosed glomeruli was 3.5 (± 4.6).

No statistically significant differences were noted in terms of total number of sclerosed glomeruli (2.9 ± 3.5 vs 5.3 ± 7.6, p=0.5) between the λ and κ AL amyloidosis cases.

ID	Age (y)	Serum Creatinine (mg/dl)	Proteinuria (g/die)	M-spike	Type of sample	GS (%)	Amyloidosis type
BFRB#1	63	0.77	6.60	λ	BFRB	2	AL λ
BFRB#2	43	0.60	3.57	λ	BFRB	0	AL λ
BFRB#3	63	2.20	4.00	IgG κ	BFRB	0	AL κ
BFRB#4	80	4.50	1.50	IgG κ on serum urine λ free light chains	BFRB	10	AL λ
BFRB#5	72	3.16	0.93	λ	BFRB	0	AL λ
BFRB#6	51	1.40	5.00	λ	BFRB	6	AL λ
BFRB#7	67	1.50	2.80	IgG κ	BFRB	2	AL κ
BFRB#8	64	0.90	5.00	IgG λ	BFRB	3	AL λ
BFRB#9	62	1.62	9.10	IgA λ	BFRB	0	AL λ
BFRB#10	63	0.77	6.60	λ	BFRB	2	AL λ
FFRB#1	69	1.80	3.40	κ	FFRB	14	AL κ
FFRB#2	74	0.64	3.5	IgG λ	FFRB	15	AL λ
FFRB#3	50	3.6	5.8	FLC λ	FFRB	0	AL λ
FFRB#4	26	2.0	11.0	IgG κ	FFRB	0	AL κ
FFRB#5	83	5.0	1.0	IgM κ	FFRB	38	AL κ

Table 1. Clinical, laboratory, and histologic features of AL renal amyloidosis cases. GS, global glomerulosclerosis; IF, immunofluorescence; AL, light chain amyloidosis; BFRB, bouin-fixed renal biopsy; FFRB, formalin-fixed renal biopsy.

MALDI-MSI and SPADA: confronting molecular and histology-guided computational approaches

To evaluate the performance of MALDI-MSI with respect to an already established computational approach for the automatic detection of amyloid plaques on tissue, each renal sample was subsequently subjected to MALDI-MSI and the SPADA pipeline. For MALDI-MSI, deposits were automatically detected according to the workflow already published[14], which relies on the distribution and colocalisation of amyloid *fingerprint* proteins (**Supplementary Information, S2**). Then, to assess the performance of MALDI-MSI and SPADA in comparison to the annotations of the pathologist based on Congo Red staining, which still represent the gold standard for amyloid detection, glomeruli were taken into consideration as the primary site of amyloid deposition[17]. The areas highlighted by MALDI-MSI and SPADA were then compared to the ROIs defined by the pathologist on Congo Red stained WSI (Whole Slide Images) to assess the correspondence of glomerular annotations in the three techniques. This analysis demonstrated a good agreement between MALDI-MSI and the pathologist's evaluation, accounting for an average of 86.4% of glomeruli in which amyloid deposits were detected by both MALDI and the pathologist (**Table 2**). When compared to MALDI-MSI, the application of the SPADA computational pipeline demonstrated higher agreement with the pathologist's evaluation in terms of positive glomeruli (average 87.8%), but still demonstrated a satisfactory agreement with the predictions of MALDI-MSI, with a percentage of agreement calculated as comparisons reflect variability on different cases, with some showing higher concordance between SPADA and the pathologist as compared to MALDI-MSI (e.g. FFRB#1, FFRB#2), and others slight superiority of MALDI-MSI in detecting more glomeruli involved by amyloidosis (e.g. BFRB#2, BFRB#5). This resulted in an overall higher percentage of glomeruli detected by the combination of MALDI-

MSI and SPADA; in fact, the combination of these two computational approaches led to the annotation of a further 6 glomeruli compared to the pathologist alone, accounting for +4.1% of annotated glomeruli.

ID	N. glomeruli	Glomeruli with amyloid (Pathologist)	Glomeruli with amyloid (MALDI-MSI)	Glomeruli with amyloid (SPADA)	Common glomeruli Path. and MALDI-MSI	Common glomeruli Path. and SPADA	Common glomeruli MALDI and SPADA
BFRB#1	3	3/3	3/3	3/3	3	3	3
BFRB#2	7	6/7	7/7	3/7	6	3	3
BFRB#3	26	26/26	26/26	26/26	26	26	26
BFRB#4	6	6/6	6/6	6/6	6	6	6
BFRB#5	9	4/9	9/9	4/9	4	4	4
BFRB#6	25	25/25	25/25	25/25	25	25	25
BFRB#7	4	4/4	4/4	4/4	4	4	4
BFRB#8	4	4/4	4/4	4/4	4	4	4
BFRB#9	4	4/4	4/4	4/4	4	4	4
BFRB#10	3	3/3	3/3	3/3	3	3	3
FFRB#1	17	17/17	15/17	17/17	15	17	15
FFRB#2	10	5/10	4/10	5/10	1	3	1
FFRB#3	11	11/11	11/11	11/11	11	11	11
FFRB#4	14	14/14	13/14	14/14	13	14	13
FFRB#5	4	2/4	3/4	3/4	2	2	3
	Tot = 147	Tot = 134	Tot = 137	Tot = 132	Tot = 127 Mean = 86.4 %	Tot = 129 Mean = 87.8 %	Tot = 125 Mean = 85.0%

Table 2. Number of glomeruli involved by amyloid deposits based on the pathologist evaluation, MALDI-MSI automatic annotations and SPADA computational pipeline detections. The number of common glomeruli is displayed for all three annotation techniques.

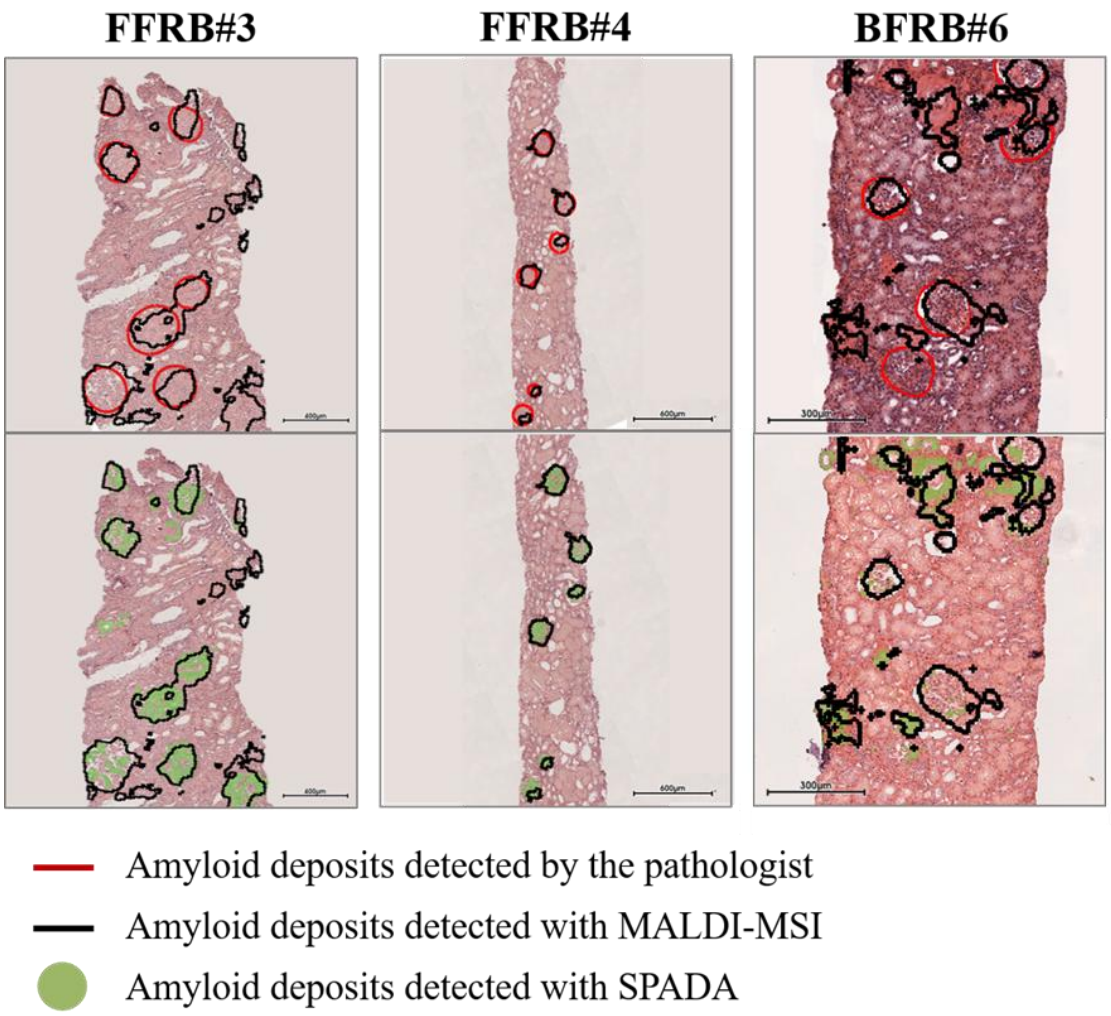

Figure 1. Amyloid deposits detected within three renal biopsies through CongoRed staining and manual annotation by the pathologist (red line), MALDI-MSI automatic segmentation (black line) and the SPADA computational pipeline (green areas). For each biopsy, the first panel displays the colocalisation of deposits annotated by the pathologist and MALDI-MSI, whilst the second panel displays the colocalisation of deposits annotated with SPADA and MALDI-MSI.

MALDI-MSI and IF: confronting spatial proteomics with a routinely used approach for amyloid typing

According to the pipeline previously described[14], ROIs which could be pinpointed as amyloid plaques highlighted by the spatial segmentation following MALDI-MSI were taken into consideration to perform amyloid subtyping. To do so, the maximum intensity of peptides belonging to the

amyloid precursor proteins of ALκ and ALλ amyloidosis (**Supplementary Information, T2**) were assessed and the most intense peak was considered for amyloid typing (**Figure 2**). Subsequently, results were compared with those of IF, which represents the most widely employed methodology for amyloid typing in the clinical practice[18]. A complete agreement was noted between IF and MALDI-MSI, with concordance in all cases for the two techniques (**Table 3**). **Figure 3** displays the sum of the maximum intensities of κ and λ fragments in automatically annotated deposits of AL amyloidosis cases; the intensities of κ and λ fragments in glomeruli of Membranous Nephropathy (MN) and normal kidney (CTRL) are also shown to display the abundance of immunoglobulin light chains in diseased and healthy negative controls. Interestingly, even in cases where glomeruli were highlighted as being amyloid-positive only by MALDI-MSI (see BFRB#2 and #BFRB#5, **Table 3**) the presence of the concordant light chain confirmed the possible genuinity of these deposits highlighted by the automatic annotation process **(Supplementary Information, S3)**. Finally, MALDI-MSI's capabilities were tested on a challenging case with equivocal positivity for λ (4+) and κ (2+) light chains on IF, namely BFRB#10, as reported in the paragraph *Cases* of the Results section. MALDI-MSI confirmed a slight prevalence of λ light chains, with fragment *m*/*z* 883.44 (LV211) being the most intense in deposits (**Figure 4a-b**, **Table 3**) and fragment *m*/*z* 998.43 (LV208) showing the highest Pearson Correlation Coefficient with deposits (PCC = 0.37) .

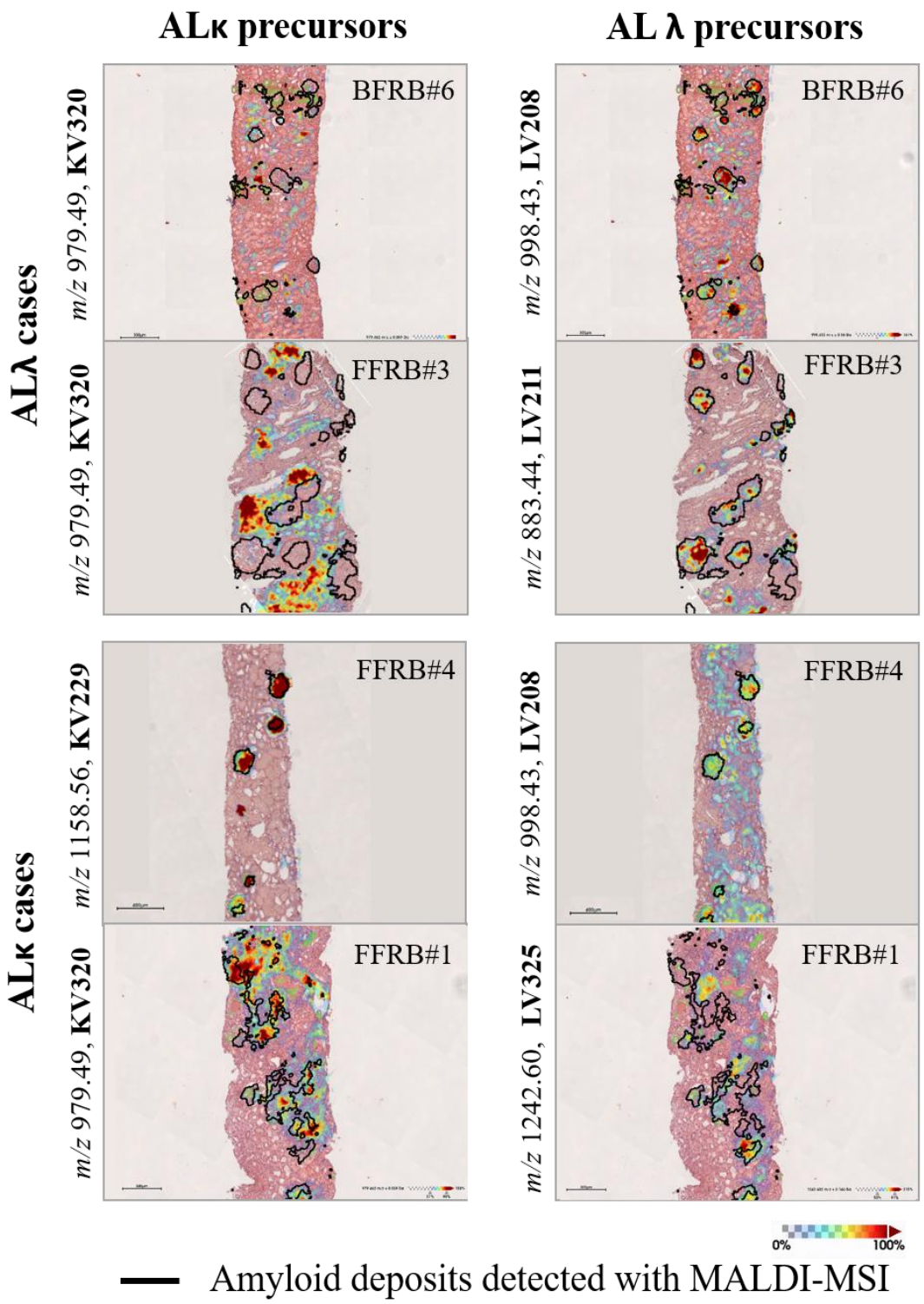

Figure 2. Distribution of the precursor proteins of immunoglobulin λ and κ light chains in cases of AL λ and κ amyloidosis. Images are visualised with Weak spatial denoising; contrast and intensity were set to maximise image quality.

ID	Histology-based AL type	Most intense peak (maximum intensity in deposits)	MALDI-based AL type
BFRB#1	ALλ	*m/z* 998.43, LV208	ALλ
BFRB#2	ALλ	*m/z* 998.43, LV208	ALλ
BFRB#3	ALκ	*m/z* 979.46, KV320	ALκ
BFRB#4	ALλ	*m/z* 883.44, LV211	ALλ
BFRB#5	ALλ	*m/z* 998.43, LV208	ALλ
BFRB#6	ALλ	*m/z* 998.43, LV208	ALλ
BFRB#7	ALκ	*m/z* 1122.52, KV401	ALκ
BFRB#8	ALλ	*m/z* 883.44, LV211	ALλ
BFRB#9	ALλ	*m/z* 883.44, LV211	ALλ
BFRB#10	ALλ	*m/z* 883.44, LV211	ALλ
FFRB#1	ALκ	*m/z* 979.46, KV320	ALκ
FFRB#2	ALλ	*m/z* 883.44, LV211	ALλ
FFRB#3	ALλ	*m/z* 883.44, LV211	ALλ
FFRB#4	ALκ	*m/z* 1158.78, KV229	ALκ
FFRB#5	ALκ	*m/z* 979.46, KV320	ALκ

Table 3. Comparison of the amyloid AL subtype based on the histological assessment and on the most intense peak (maximum intensity in automatically annotated deposits) after MALDI-MSI analysis.

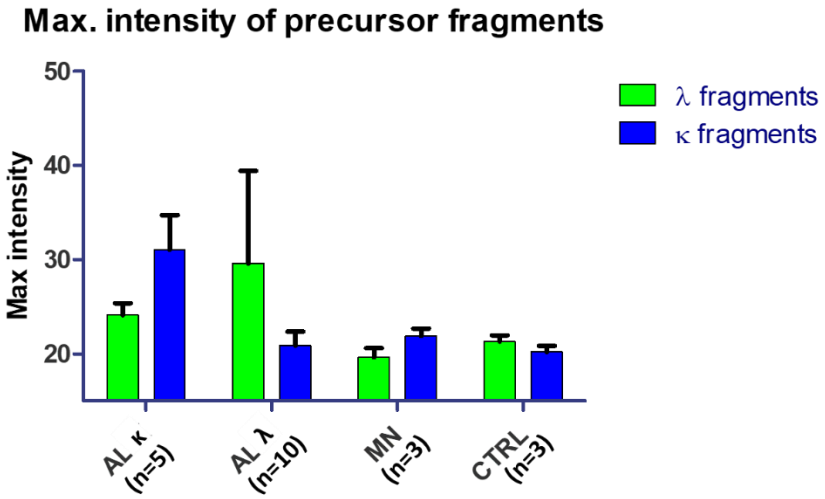

Figure 3. Sum of the maximum intensities of all target λ and κ fragments in amyloid deposits annotated with MALDI-MSI in AL amyloidosis renal biopsies (ALκ, AL λ) or in glomeruli of Membranous nephropathy (MN) biopsies and normal kidney (CTRL) cases.

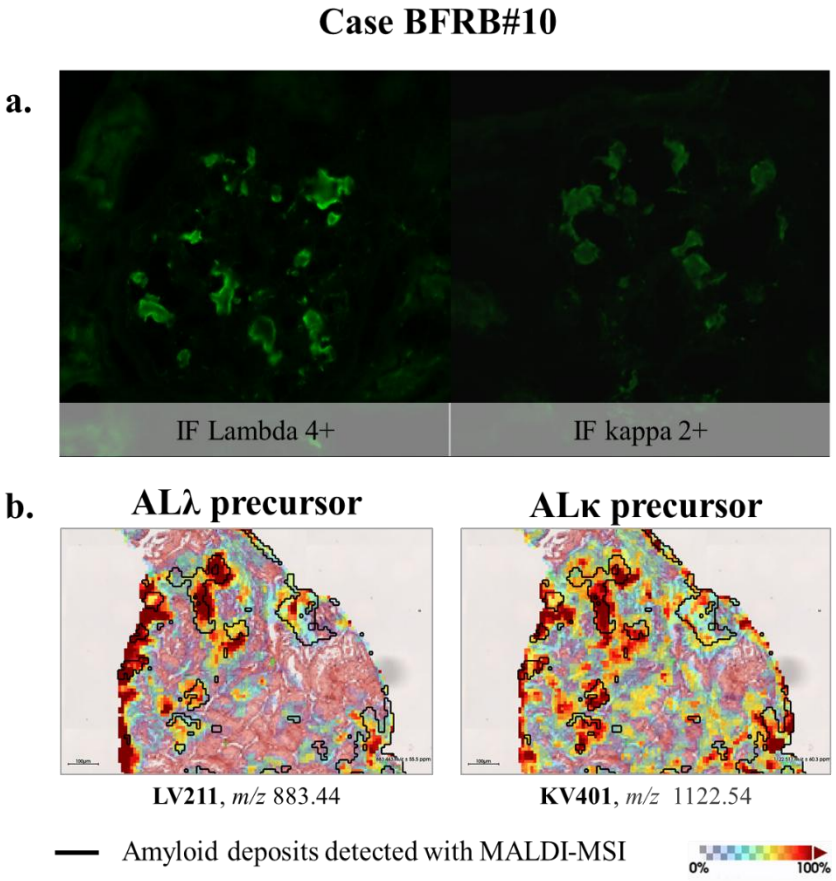

Figure 4 a) Ambiguous results of the IF for immunoglobulin light chains (4+ for λ and 2+ for κ) in case BFRB#10 **b)** Distribution of the most intense λ (LV211) and κ (KV401) peptides in case BFRB#10. Whilst LV211 emerges as the most intense peptide, a co-deposition of both chains is displayed. Images are visualised with Weak spatial denoising; contrast and intensity were set to maximise image quality.

Discussion

The direct involvement of kidney parenchyma by misfolded proteins produced by neoplastic plasma cell clones (MGRS) is gaining progressively more importance in the onco-nephrology setting[19]. However, the routinely used armamentarium of pathology departments can be insufficient for the correct characterisation of these diseases, especially in the context of amyloidosis, whose precursor protein list is progressively extending[20] and where the differentiation of MGRS-related forms (such as ALκ or ALλ amyloidosis) from other rarer entities is paramount for therapeutic strategy[4]. In this direction, MS is the natural solution for the comprehensive and one-shot analysis of these precious biopsies, especially when considering MALDI-MSI, where the spatial coordinates of detected proteins signals are conserved, sparing tissue from destruction all whilst coupling morphological and molecular information[10,14,21-23].

This work explores the application of MALDI-MSI on ALκ or ALλ renal amyloidosis biopsies. Firstly, the possibility to perform MALDI-MSI-based automatic segmentation using amyloid *fingerprint* proteins[14,24] was confirmed and results were correlated to another automatic computational tool, the SPADA pipeline, which already proved its efficiency to aid in the screening of renal biopsies for amyloid deposits[16]. MALDI-MSI results indicated, on the whole, a slightly lower percentage of agreement with the pathologist and SPADA (86.4% and 85.0%, respectively) compared to the agreement of annotation performed with the histology-based approaches (87.8%). However, this is to be expected, considering that the histology-based approaches both assess amyloid deposition based on the birefringence of misfolded proteins in Congo Red stained slides, whereas MALDI-MSI detects the contemporary presence of tryptically digested amyloid *fingerprint* proteins, whilst accounting

for their tissue distribution and intensity. Therefore, considering that these techniques are based on different premises, the resulting average agreement is still satisfying, and within MALDI-MSI detected deposits it was still possible to denote a good colocalisation of amyloid precursor proteins (**Figure 2, Supplementary Information S3**). It is interesting to point out that in those instances in which MALDI-MSI annotated a greater number of glomeruli with respect to the histology-based approaches (e.g. case BFRB#2 and BFRB#5, **Table 2**) the deposition of expected immunoglobulin light chains within the indicated regions could still be confirmed (**Supplementary Information, S3**), increasing the confidence of these annotations and hinting at the possible capability of MALDI-MSI to annotate amyloidosis at an earlier stage of protein deposition, probably due to its lack of reliance on amyloid birefringence. Moreover, in some instances MALDI-MSI and/or SPADA could detect more deposits than the pathologist, accounting for around 4% of all annotated glomeruli. Considering that all three annotation techniques can be successfully performed on a single tissue slide, the integration of these complementary approaches could potentially lead to a more comprehensive and unbiased detection of all amyloid deposits, further refining computational-aided amyloid annotation whilst still relying on the expert eye of a trained pathologist.

MALDI-MSI's ability to correctly type amyloidosis was also assessed, indicating a complete agreement with immunofluorescence. Interestingly, the case that displayed an ambiguous diagnosis with immunofluorescence (**Figure 4.a**) could still be typed with MALDI-MSI, whilst also assessing the co-deposition of both κ and λ immunoglobulin light chains (**Figure 4.b**); these findings further stress the strategic role of this technique in the characterisation of challenging-to-diagnose onco-nephrology cases. On the whole, this study confirms the strategic role of MALDI-MSI to perform both automatic detection and typing of amyloidosis on a single tissue section, even in the instance of

challenging cases and irrespective of the type of fixative, whilst still preserving tissue for further staining with Congo Red and application of the SPADA pipeline.

Conclusions

This study confirmed the capability of MALDI-MSI to detect and type AL amyloidosis irrespectively of the type of fixative, assessing the possibility to integrate an additional, computational method for amyloid detection on a single tissue slide.

Supporting Information

Supporting Information is available at https://drive.google.com/drive/folders/14ph4fe_yw-6V7AUfRP_knpftR3kLd4iX

References

1 Leung N, Nasr SH, Sethi S. How I treat amyloidosis: the importance of accurate diagnosis and amyloid typing. Blood. 2012 Oct;120(16):3206–13.

2 Kidd J, Carl DE. Renal amyloidosis. Curr Probl Cancer. 2016 Aug;40(5-6):209–19.

3 Fogo AB, Lusco MA, Najafian B, Alpers CE. AJKD Atlas of Renal Pathology: AL Amyloidosis. Am J Kidney Dis. 2015 Dec;66(6):e43–5.

4 L'Imperio V, Cazzaniga G, Vergani B, Smith AJ, Alberici F, Pagni F. Monoclonal Gammopathy of Renal Significance: A Molecular Middle Earth between Oncology, Nephrology, and Pathology. Kidney Diseases. 2022;1–12.

5 Gonzalez Suarez ML, Zhang P, Nasr SH, Sathick IJ, Kittanamongkolchai W, Kurtin PJ, et al. The sensitivity and specificity of the routine kidney biopsy immunofluorescence panel are inferior to diagnosing renal immunoglobulin-derived amyloidosis by mass spectrometry. Kidney Int. 2019 Oct;96(4):1005–9.

6 Dasari S, Theis JD, Vrana JA, Rech KL, Dao LN, Howard MT, et al. Amyloid Typing by Mass Spectrometry in Clinical Practice: a Comprehensive Review of 16,175 Samples. Mayo Clin Proc. 2020 Sep;95(9):1852–64.

7 Benson MD, Buxbaum JN, Eisenberg DS, Merlini G, Saraiva MJM, Sekijima Y, et al. Amyloid nomenclature 2020: update and recommendations by the International Society of Amyloidosis (ISA) nomenclature committee. Amyloid. 2020 Dec;27(4):217–22.

8 L'Imperio V, Morello G, Vegliante MC, Cancila V, Bertolazzi G, Mazzara S, et al. Spatial transcriptome of a germinal center plasmablastic burst hints at MYD88/CD79B mutants-enriched diffuse large B-cell lymphomas. Eur J Immunol. 2022 Aug;52(8):1350–61.

9 Vrana JA, Theis JD, Dasari S, Mereuta OM, Dispenzieri A, Zeldenrust SR, et al. Clinical diagnosis and typing of systemic amyloidosis in subcutaneous fat aspirates by mass spectrometry-based proteomics. Haematologica. 2014 Jul;99(7):1239–47.

10 Smith A, L'Imperio V, Denti V, Mazza M, Ivanova M, Stella M, et al. High Spatial Resolution MALDI-MS Imaging in the Study of Membranous Nephropathy. Proteomics Clin Appl. 2019 Jan;13(1):e1800016.

11 Lavatelli F, Merlini G. Proteomics with Mass Spectrometry Imaging: Beyond Amyloid Typing. Proteomics. 2018 Apr;18(7):e1700353.

12 L'Imperio V, Bruno I, Rabach I, Smith A, Chinello C, Stella M, et al. Histoproteomic Characterization of Localized Cutaneous Amyloidosis in X-Linked Reticulate Pigmentary Disorder. Skin Pharmacol Physiol. 2017 Apr;30(2):90–3.

13 Winter M, Tholey A, Kristen A, Röcken C. MALDI Mass Spectrometry Imaging: A Novel Tool for the Identification and Classification of Amyloidosis. Proteomics. 2017 Nov;17(22). DOI: 10.1002/pmic.201700236

14 Bindi G, Smith A, Oliveira G, Eccher A, Vatrano S, Alberici F, et al. Spatial resolution of renal amyloid deposits through MALDI-MSI: a combined digital and molecular approach to monoclonal gammopathies. J Clin Pathol. 2024 May;77(6):402–10.

15 Bindi G, Pagani L, Ceku J, de Oliveira GS, Porto NS, Monza N, et al. Feasibility of MALDI-MSI-Based Proteomics Using Bouin-Fixed Pathology Samples: Untapping the Goldmine of Nephropathology Archives. J Proteome Res. 2024 Jul;23(7):2542–51.

16 Cazzaniga G, Bolognesi MM, Stefania MD, Mascadri F, Eccher A, Alberici F, et al. Congo Red Staining in Digital Pathology: The Streamlined Pipeline for Amyloid Detection Through Congo Red Fluorescence Digital Analysis. Lab Invest. 2023 Nov;103(11):100243.

17 Rubinstein S, Cornell RF, Du L, Concepcion B, Goodman S, Harrell S, et al. Novel pathologic scoring tools predict end-stage kidney disease in light chain (AL) amyloidosis. Amyloid. 2017 Sep;24(3):205–11.

18 Gibier J-B, Perbet R, Lopez B, Colombat M, Dubois R, Humez S, et al. Paraffin Immunofluorescence Increases Light-Chain Detection in Extra-Renal Light Chain Amyloidosis

and Other Light-Chain-Associated Diseases. Arch Pathol Lab Med. 2021 Mar;145(3):352–8.
19 Rosner MH, Jhaveri KD, McMahon BA, Perazella MA. Onconephrology: The intersections between the kidney and cancer. CA Cancer J Clin. 2021 Jan;71(1):47–77.
20 Leung N, Nasr SH. 2024 Update on Classification, Etiology, and Typing of Renal Amyloidosis: A Review. Am J Kidney Dis. 2024 Sep;84(3):361–73.
21 Smith A, L'Imperio V, Ajello E, Ferrario F, Mosele N, Stella M, et al. The putative role of MALDI-MSI in the study of Membranous Nephropathy. Biochim Biophys Acta: Proteins Proteomics. 2017 Jul;1865(7):865–74.
22 L'Imperio V, Smith A, Pisani A, D'Armiento M, Scollo V, Casano S, et al. MALDI imaging in Fabry nephropathy: a multicenter study. J Nephrol. 2020 Apr;33(2):299–306.
23 L'Imperio V, Smith A, Ajello E, Piga I, Stella M, Denti V, et al. MALDI-MSI Pilot Study HighlightsGlomerular Deposits of Macrophage Migration Inhibitory Factor as a Possible Indicator of Response to Therapy in Membranous Nephropathy. Proteomics Clin Appl. 2019 May;13(3):e1800019.
24 Winter M, Tholey A, Krüger S, Schmidt H, Röcken C. MALDI-mass spectrometry imaging identifies vitronectin as a common constituent of amyloid deposits. J Histochem Cytochem. 2015 Oct;63(10):772–9.

2.5 Conclusions to Chapter 2

The detection and typing of renal amyloidosis can be particularly challenging, both because of the pitfalls associated with routinely employed approaches and due to the limited amount of biopsy material available for investigation. In this Chapter, we described a novel workflow based on MALDI-MSI that supports the detection of amyloid deposits directly on tissue. This approach also enables the spatial distribution of amyloid precursor proteins to be visualised with respect to the deposits, permitting amyloid typing on the same tissue slide. This workflow tackles the specific challenges associated with renal amyloid detection and typing given that it overcomes some of the limitations linked to routinely employed techniques, and, critically, it only requires a single tissue section. Whilst the identification of a streamlined workflow for the one-slide diagnosis of this disease already represents an important step towards the application of MALDI-MSI within the clinical setting, different pathology centres often adopt distinct sample preparation protocols. This can introduce variability when applying the same analytical approach to specimens sourced from multiple centres. Therefore, in this Chapter we also evaluated the robustness of the proposed approach in samples processed with different common fixatives and fixation times, thereby broadening its potential use and enabling larger-scale multicentre studies. Lastly, a further effort was directed toward integrating an additional imaging modality, specifically, a computationally aided approach for amyloid detection, on the same tissue slide. Given the growing role of computational methods in disease classification, the integration of this additional imaging modality bridges the gap between digital and molecular pathology, with an eye toward the future clinical utility of the latter.

Altogether, this promising line of research represents an important step toward the clinical application of MALDI-MSI, demonstrating how this high-throughput spatial technique can contribute to the elucidation of challenging-to-diagnose diseases such as renal amyloidosis, while bridging the gap between bench and bedside.

Concluding remarks

In conclusion, this thesis has demonstrated the application of spatially resolved mass spectrometry across several facets of renal pathology, including molecularly driven disease investigation as well as the path to clinical translation.

Mass spectrometry-based *omic* approaches are becoming increasingly important in clinical research; however, considerable work remains in order to fully tailor their use to the field of renal pathology and to promote their adoption for the analysis of clinical specimens. Specifically, in the context of rare renal diseases, the ability to investigate retrospective cases, spanning multiple centres, is critical to obtain sufficiently sized patient cohorts. In this work, this need was addressed by employing and refining analytical workflows compatible with fixed and embedded specimens. These samples remain more challenging than fresh material due to the formation of stable methylene bridges between amino acid residues, which prevent tissue degradation but simultaneously pose challenges for protein analysis and require specific decrosslinking steps. However, their use enables access to extensive nephropathology archives, facilitating larger retrospective cohorts and supporting multicentric studies. This thesis further addressed this aspect by taking into account the methodological variability across clinical facilities, which constitutes a challenge when attempting to implement standardised protocols for clinical sample preparation. Importantly, whilst the analytical robustness across differently processed samples could be confirmed, this work also highlighted proteomic differences associated with the use of different fixatives. This underscores the need to further investigate the impact of sample processing on the resulting molecular profiles and highlights the importance of providing sample preparation guidelines to enable studies in which samples

are collected across multiple facilities, particularly in the context of large retrospective studies and rare diseases.

Another obstacle related to the more widespread adoption of molecular approaches within the nephropathology setting lies in the limited amount of available tissue, and specifically, the conflicting demand between routine diagnostic assessments and clinical research purposes. Given the human origin and diagnostic relevance of patient-derived material from pathology units, sample preservation is crucial, both for tumour resections and renal biopsies. Accordingly, this thesis proposes the use of mass spectrometry as a highly sensitive analytical approach that requires only minimal amounts of tissue, rendering it well suited for implementation in renal pathology. Most importantly, the development of workflows requiring only a single tissue section, for instance through the integration of two sequential spatial *omic* approaches described in Chapter 1, or through the streamlined workflow for amyloid detection and typing presented in Chapter 2, was prioritised. The implementation of high-throughput, non-destructive, approaches capable of maximising the extraction of extensive molecular information from residual diagnostic material aligns naturally with the necessity of sample preservation.

Importantly, beyond limiting sample usage, the application of multiple approaches on a single tissue slide also facilitates the integration of several layers of spatially resolved data. This permits the correlation of complementary molecular levels within regions of interest, supporting a more comprehensive characterisation of local tissue biology; this aspect is already critical in the complex and heterogeneous environment of a diseased kidney, but becomes essential for the thorough molecular characterisation of the multicellular context of the tumour microenvironment. In Chapter 1, this spatial integration enabled the characterisation of the immune landscape of the TME of ccRCC, while also investigating proteomic alterations induced by distinct immune

phenotypes on surrounding cells. This represents an important step forward in the exploration of the tumour-immune microenvironment, as it permits, through the MALDI-HiPLEX-IHC-MSI workflow, the unprecedented multiplexed targeting of antigens of interest without limiting the untargeted exploration of other molecular layers. In the thriving field of tumour immunology, this enables the spatial mapping of previously characterised markers of immunomodulation, as for instance the presence of T regulatory cells, whilst also aiding the discovery of unknown immune-related markers at a multimolecular level. In Chapter 2, the proteomic profiling of renal biopsies followed by the joint application of a computational approach powered by digital pathology on the same tissue section allowed the mapping of amyloid deposits, permitting disease detection, while simultaneously profiling resulting annotations for disease typing. This integration further enhanced the multimodality of the workflow, deriving complementary molecular and histological information from a single slide. When trying to push the implementation of mass spectrometry in the field of nephropathology, the possibility to directly correlate molecular distributions with tissue morphology facilitates cross-disciplinary collaboration between researchers and clinicians, bridging the gap between bench and bedside.

Overall, this work provides methodological solutions to some of the limitations which have previously hindered the molecular analysis of renal tissue, specifically in rare diseases and limited clinical material. Altogether, this thesis represents a step forward in the application of mass spectrometry-based methodologies, particularly spatially resolved approaches, within renal pathology, supporting studies investigating the molecular basis of disease as well as those which could be translated to provide support in the pathological workup of clinical cases.